Monte Carlo simulation applied to uncertainties in iodine-123 assay and thyroid uptake measurement

By

Matthew Talboys

Cardiff University, School of Engineering

PhD Thesis

2016

DECLARATION

This work has not been submitted in substance for any other degree or award at this or any other university or place of learning, nor is being submitted concurrently in candidature for any degree or other award.

Signed …… (candidate) Date ……

STATEMENT 1

This thesis is being submitted in partial fulfilment of the requirements for the degree of PhD

Signed …… (candidate) Date ……

STATEMENT 2

This thesis is the result of my own independent work/investigation, except where otherwise stated. Other sources are acknowledged by explicit references. The views expressed are my own.

Signed …… (candidate) Date ……

STATEMENT 3

I hereby give consent for my thesis, if accepted, to be available online in the University's Open Access repository and for inter-library loan, and for the title and summary to be made available to outside organisations.

Signed …… (candidate) Date ……

SUMMARY

The Monte Carlo method can be used to simulate deterministic processes such as the interaction of nuclear particles with matter, using a probabilistic approach. For radiation transport, the method is realised using Monte Carlo radiation transport codes. Performing simulations often has a distinct advantage over experimental studies, especially when physical measurements would be impracticable or even impossible to undertake. The application of Monte Carlo methods to nuclear medicine problems can therefore be seen as advantageous.

^{123}I is a commonly utilised radionuclide for nuclear medicine diagnostic imaging and non-imaging investigations. The radioactive decay scheme of ^{123}I presents particular challenges in terms of accurately determining the activity of an ^{123}I based radiopharmaceutical prior to administration.

The aims of this project were to use Monte Carlo modelling techniques to investigate the uncertainties associated with ^{123}I assay and thyroid uptake assessment using this radionuclide. A model of the UK secondary standard calibrator was created using MCNP5 code and validated against the physical calibrator. A sensitivity curve for the instrument was created through simulation and the effect of measuring ^{123}I using a vial and a syringe investigated. Up to 21% variation was seen between the vial and the syringe geometries studied.

A thyroid uptake counter model was produced to determine uncertainties in thyroid uptake assessment for a number of different parameters. Variations in collimator to

neck distance, horizontal displacement of the detector and increasing depth of the thyroid gland in tissue were shown to affect the accuracy of uptake measurement. A depth-based correction for the thyroid gland was derived from the differential counts in the x-ray and gamma peaks of ^{123}I. Such an approach could be utilised in clinical practice to correct for the depth of the thyroid gland in the neck.

ACKNOWLEDGEMENTS

I am extremely grateful to Professor Wil Evans and Professor Peter Wells for firstly affording me the opportunity to undertake these studies and for their invaluable guidance and support throughout. I would like to thank other colleagues in the Medical Physics Department of the University Hospital of Wales for their assistance at numerous instances during my studies.

I would also like to acknowledge the emotional and practical support afforded me by my family members and friends.

CONTENTS

LIST OF ABBREVIATIONS

ALARP	As Low as Reasonably Practicable
ARSAC	Administration of Radioactive Substances Advisory Committee
BNMS	British Nuclear Medicine Society
Bq	Becquerel
BS	British Standard
CT	Computed Tomography
EC	European Commission
EDTA	Ethylenediamine Tetraacetic Acid
ENDF	Evaluated Nuclear Data File
EGS	Electron Gamma Shower
FWHM	Full Width at Half Maximum
Geant4	Geometry and Tracking version 4
GBq	Giga Becquerel
GFR	Glomerular Filtration Rate
HDP	Hydroxymethane Diphosphonate
HMPAO	Hexamethylpropyleneamine Oxime
HPGe	High Purity Germanium
I^-	Iodine ions
IAEA	International Atomic Energy Authority
IRMER	Ionising Radiation (Medical Exposure) Regulations
MBq	Mega Becquerel
MCA	Multichannel Analyser
MCNP5	Monte Carlo N-Particles version 5

MIBG	Metaiodobenzylguanidine
MRI	Magnetic Resonance Imaging
NaI(Tl)	Thallium Doped Sodium Iodide
NPL	National Physical Laboratory
PET	Positron Emission Tomography
PMMA	Polymethyl Methacrylate
PMT	Photomultiplier Tube
ROI(s)	Region(s) of Interest
SeHCAT	Selenium Tauroselcholic Acid
SNM	Society of Nuclear Medicine
SPECT	single Photon Emission Computed Tomography
T_3	Triiodothyronine
T_4	Thyroxine
TSH	Thyroid Stimulating Hormone
UK	United Kingdom
USA	United States of America

CHAPTER 1: INTRODUCTION

1.1 Nuclear medicine

Nuclear medicine is a term that encompasses the use of radiopharmaceuticals for both diagnostic and therapeutic applications. The basic premise of a nuclear medicine procedure includes the administration of a radiopharmaceutical to either induce a therapeutic effect or undertake measurements to glean a diagnostic result. Diagnostic applications of nuclear medicine can be further subdivided into those concerning imaging, generally using a gamma camera and non-imaging, where in-vitro or in-vivo assays are conducted on samples or within the body.

The radiopharmaceutical administered principally consists of two chemically attached components, the radionuclide and the pharmaceutical. The purpose of the radionuclide is, via the process of radioactive decay, to emit ionising radiations to administer a therapeutic effect or be detected as part of a diagnostic test. The type of ionising radiations emitted from the radionuclide is one aspect of the design of a radiopharmaceutical that determines its suitability as either diagnostic or therapeutic. Highly ionising particulate emissions, namely α and β particles are principally used for therapeutic purposes. Gamma emitting radionuclides are generally reserved for diagnostic applications. They are not completely incompatible with the alternative use however. For example, ^{14}C is often administered orally for the detection of the stomach ulcer causing bacteria, Helicobacter Pylori, and ^{131}I may also be administered, although very rarely, for diagnostic thyroid uptake procedures. As well as the emissions, the half-life of the radionuclide will also determine its suitability to

be used in a medical context. For diagnostic purposes, the half-life needs to be consistent with the length of the investigation but not too long leading to a high effective dose or too short to prohibit non-diagnostic data acquisition.

The pharmaceutical element of the radiopharmaceutical determines its fate within the body by acting as a tracer for a particular physiologic or biochemical process. Some radionuclides may be administered without significant chemical interference. For example, ^{99m}Tc sodium pertechnetate may be used in its eluted form for diagnostic thyroid and Meckel's diverticulum imaging. However, most radionuclides will be bound to a pharmaceutical tracer, predominately through the addition of the radionuclide to a chemical complex or through incorporation into autologous blood cells. Typically, administration of the radiopharmaceutical is via an intravenous injection in the antecubital fossa region, however, other modes of administration including inhalation and ingestion may be employed depending on the particular clinical indication.

Diagnostic imaging using a gamma camera was the predominant nuclear medicine procedure undertaken in 2003-2004 (Hart and Wall, 2005). A wide range of diagnostic imaging radiopharmaceuticals have been developed to image physiological processes of the body. The instrumentation used for nuclear medicine imaging was first developed in the 1950s by Hal Anger, an American biophysicist (Anger, 1957). The basic components of a gamma camera have not drastically changed in the six decades that have proceeded, with the major development being the move from analogue to digital image acquisition and processing. A gamma camera can provide static, dynamic and three-dimensional reconstructed images of

the distribution of a radiopharmaceutical within the body. By virtue of being a physiological imaging technique, the acquired images in some instances may not closely resemble the anatomical structure of the tissues or organs under investigation (Figure 1.1). Hence image fusion with an anatomical imaging modality, for example CT or MRI, can be advantageous in some applications.

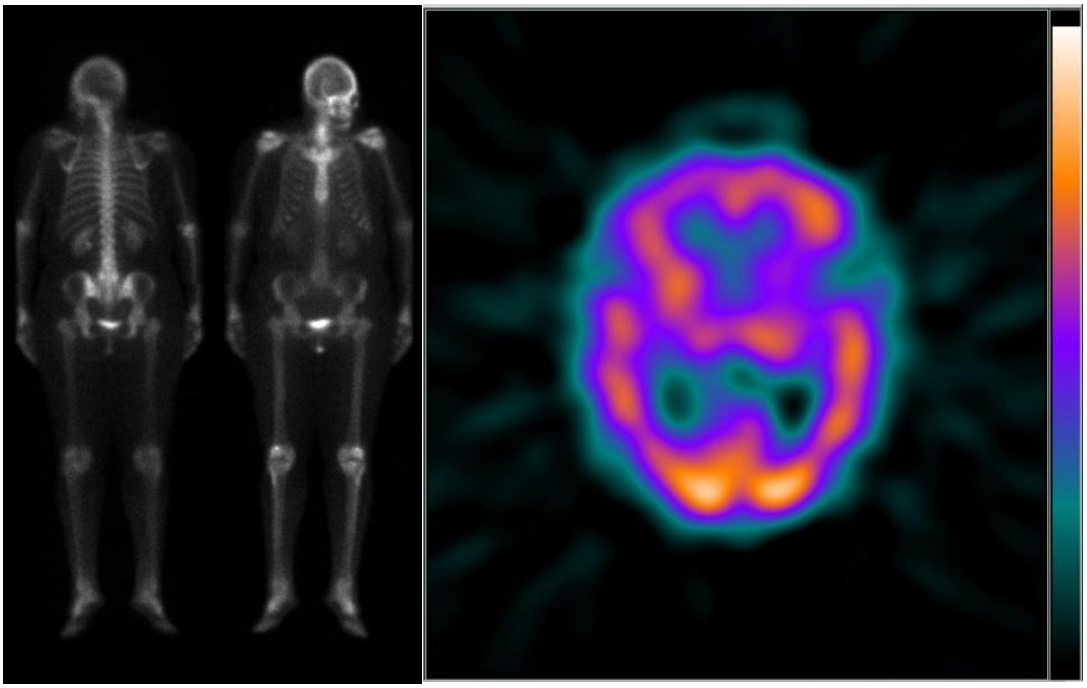

Figure 1.1: Left – ^{99m}Tc HDP scan showing accumulation of the radiopharmaceutical in the skeletal system. This shows good resemblance with the anatomical structures. Right – ^{99m}Tc HMPAO scan showing blood perfusion of the brain. Anatomical resemblance is more abstract in this instance

Non-imaging diagnostic nuclear medicine investigations are either undertaken in-vivo (e.g. thyroid uptake assessment) or in vitro (e.g. GFR measurement). There are some notable advantages for undertaking non-imaging nuclear medicine investigation as compared to imaging using a gamma camera. Firstly, gamma camera imaging is inherently an inefficient technique and requires administered activities usually in the region of 10s – 100s of MBq of the radionuclide. Non-imaging nuclear medicine investigations can employ more sensitive detection equipment and therefore the total activity administered to the patient, and hence the radiation detriment they receive, can be reduced. The other notable advantage of non-imaging techniques is that it is possible to use other radionuclides such as ^{14}C and ^{125}I, where their emissions deem them unsuitable for gamma camera imaging. This allows for different tracer pathways to be assessed in the body. Some examples of non-imaging nuclear medicine applications include ^{75}SeHCAT studies to investigate the re-absorption of bile acids in the intestines and ^{51}Cr EDTA investigations to calculate the GFR of the kidneys as a parameter of kidney function.

1.2 Applications of radioiodine in nuclear medicine

Iodine is an essential trace element for human life. One of the primary functions of iodine in the body is via the incorporation into thyroid hormones, which allow for the regulation of various body processes. The synthesis of thyroid hormones occurs in the thyroid gland and therefore dietary iodine is predominately taken up by, and stored in, the thyroid.

Radioiodine has been employed in nuclear medicine for both diagnostic and therapeutic applications for a number of decades. Only one isotope of iodine is stable, namely ^{127}I. The three main medical isotopes of iodine are ^{123}I, ^{125}I and ^{131}I. ^{124}I, a positron emitter, is also finding some diagnostic clinical application using PET. Biologically, radioisotopes of iodine are indistinguishable from ^{127}I when administered in unaltered pharmaceutical form. Therefore, administered radioiodine can usually be found in high concentrations in the thyroid gland.

The potential detrimental effects of radioiodine accumulation in the thyroid gland were evident following the Chernobyl accident. Huge quantities of ^{131}I were released into the atmosphere and entered into the human food chain mainly through the cow-milk pathway. In the subsequent years following the accident, the incidence of childhood thyroid cancers, particularity papillary cancer, rose dramatically, in some regions to over 100 fold (Stsjazhko et al., 1995). The increase was proportional to the radiation dose received (Bennett et al., 2006).

In terms of nuclear medicine imaging, ^{123}I is widely used as an imaging radionuclide. For diagnostic purposes, the aim is to keep the radiation burden ALARP to prevent any stochastic radiation detriment that may occur over time. Although it was once commonplace for ^{131}I to be administered for diagnostic purposes, it has generally been superseded by ^{123}I. This is due to its convenient gamma emissions for imaging and detection using conventional imaging equipment (scintillation or semi-conductor detectors) and lower radiation dose to the patient due to the lack of β^- emissions. Two examples of ^{123}I based investigations not used for thyroid imaging include ^{123}I MIBG for neuroendocrine tumour imaging and ^{123}I Ioflupane (DaTscan™) for imaging the dopaminergic cells in the brain. Where there is a possibility of free radioiodine, it is prudent to administer thyroid blocking medication to reduce the detriment to the thyroid for non-thyroid investigations.

Radioiodine treatment is also undertaken for both benign and malignant thyroid conditions. ^{131}I is usually employed for both procedures as one of its particulate emissions are β^- particles. β^- particles have a mid level linear energy transfer and can therefore cause ionisation over a small distance within tissues (e.g. 1 MeV β^- particles have a range of less than 1 cm in water (Cherry et al., 2003)). The difference between treating a benign and malignant condition usually lies in the fact that the patient may have had a thyroidectomy for malignant cancers and the administered activities may be in the region of several GBq for malignant therapy as opposed to typically 100s of MBq for benign conditions.

1.3 Introduction to Monte Carlo simulation

Stochastic simulation techniques have found a wide area of application in a number of different fields including the physical sciences, finance, business and telecommunications. One of the earliest examples of a stochastic simulation was proposed by Comte de Buffon in the 18th Century and is known as the 'Buffon needle experiment'. Buffon's experiment involved randomly dropping needles on a panelled floor to determine the probability that the needle intersects the panels. Monte Carlo techniques can also be applied to this experiment to determine an estimate of π. In the 1930's, Fermi used stochastic methods to study the moderation of neutrons (Metropolis, 1987). While working on the Manhattan Project, John Von Neumann and Stanislaw Ulam further developed the use of random sampling to solve deterministic mathematical equations (Price, 2008). Due to the probabilistic nature of the method, the term Monte Carlo was coined as a reference to the famous casino in the administrative area and the first paper using this phrase (to describe stochastic methods) in the title was published in 1949 (Metropolis and Ulam, 1949).

Monte Carlo simulations allow the collection of a vast amount of information about the system that would that in many circumstances not be possible or practical with real time experimentation. One particular application of the Monte Carlo method is to simulate radiation transport in a given system. The principles of a Monte Carlo simulation for radiation transport are outlined by Price (2008) and are summarised as follows:

- A nuclear particle is generated originating from the desired source distribution
- Sampling routines and cross sectional data is used to determine its fate within the specified geometry.

- The statistical sampling process relies on the selection of pseudo-random numbers and using probabilistic data transport libraries to determine the outcome at each step of the particle's life.
- The particle history describes the progression of a particle from the start of its simulation to termination.
- By simulating a sufficiently large number of histories, reliable statistical averages of the tallies which are preselected can be returned.

1.4 Current Monte Carlo research in medical physics

The Monte Carlo method has the potential for a wide variety of applications within the field of medical physics. The use of Monte Carlo techniques has found particular application in radiotherapy treatment planning. A recent review article highlights the use of Monte Carlo in radiotherapy treatment planning for both photon and electron beams and details some of the commercially available Monte Carlo treatment planning systems (Reynaert et al., 2007). It is also envisaged that Monte Carlo simulations will be instrumental in the treatment planning for proton beam therapy in the near future (Paganetti, 2014).

Its use within nuclear medicine has also been demonstrated for both diagnostic and therapeutic applications. An invited perspective article highlights the current uses and the future potential of the Monte Carlo method in nuclear medicine (Bolch, 2010). Some of the current applications highlighted include generating radionuclide absorbed dose S values, modelling of therapeutic radiopharmaceutical administrations in patients and also the modelling of nuclear medicine diagnostic imaging equipment. The design of SPECT and PET systems has received

considerable attention with one Monte Carlo code, GATE, written and validated specifically, for such applications (Staelens et al., 2003) (Lamare et al., 2006). Also, the usefulness of the Monte Carlo method has been demonstrated for radiation protection purposes for predicting the dose to nuclear medicine staff members wearing different protective garments (Fog and Collins, 2008).

1.5 Outline of research objectives

As previously stated, ^{123}I is a commonly utilised radionuclide for nuclear medicine diagnostic imaging and non-imaging investigations. The decay scheme of ^{123}I as described in chapter 3 presents particular challenges in terms of accurately determining the radioactivity of a ^{123}I based radiopharmaceutical prior to administration. In medical institutions, access to sophisticated assay equipment is generally not available and therefore for convenience ionisation chambers are utilised to undertake the assay. Inaccuracies in determining the radioactivity of a ^{123}I based radiopharmaceutical may have two consequences. Firstly, UK legislation requires the accurate administration of known amount of activity within particular tolerances and therefore compliance with the legislation may be compromised. Secondly, inaccuracies in the assay procedures will inevitably propagate into uncertainty in quantitative nuclear medicine studies where accurate initial assay is a proviso and also semi-quantitative studies, for example thyroid uptake assessment.

The following hypothesis is proposed:

"Monte Carlo techniques can be used to accurately simulate a radionuclide calibrator and thyroid uptake counter and quantify uncertainties with respect to ^{123}I measurement"

The first element of this work therefore investigates the uncertainties associated with ^{123}I assay using commonly available assay equipment with suggestions of suitable correction strategies. The second theme of the thesis is the investigation of the uncertainties associated with thyroid uptake assessments with the application of a thyroid depth correction.

CHAPTER 2: SIMULATION OF RADIATION TRANSPORT USING MONTE CARLO TECHNIQUES

2.1 Introduction

The Monte Carlo method can be used to simulate deterministic processes such as the interaction of nuclear particles with matter, using a probabilistic approach. For radiation transport, the method is realised by using Monte Carlo radiation transport codes. A number of such codes are available, including Monte Carlo N-Particles, Electron Gamma Shower and Geant4.

As described in section 1.3, undertaking a simulation does have some distinct advantages over experimental studies. For example, Monte Carlo simulations are used to assess absorbed doses to tissues that would not be possible to measure non-invasively. Also, as shown in later chapters, it is possible to change the material compositions of equipment, for example the chamber gas of a radionuclide calibrator, which may pose significant cost and practical difficulties if undertaken physically.

In this chapter the salient features of Monte Carlo transport codes are presented along with an overview of the radiation Monte Carlo code used for the subsequent investigations.

2.2 Salient features of Monte Carlo radiation transport codes

At the heart of all Monte Carlo radiation transport codes are a number of core components to allow for the interactions of ionising radiation with matter to be simulated. The simulations outlined in the following chapters of this thesis concern photon transport. The following sections are therefore primarily concerned with the description of Monte Carlo codes in relation to photon transport. The core components as outlined by Price (2008) include:

- Models for the physical processes
- Sampling routines
- Tallies
- Variance reduction techniques

A brief description of each component is provided.

2.2.1 Models for the physical processes

High energy photons (x and gamma rays) may interact with atoms of the materials through which they transverse. When a photon interacts with an atom it may undergo absorption or scattering events in which it loses a proportion or all of its energy. Any energy lost by the incident photon is transferred to the atom.

There are four main processes with which photons interact with matter.

- Coherent (Rayleigh) scattering

Coherent scattering is an interaction that occurs when a photon impinges on an atom and is scattered without losing any energy. This type of interaction leads to a photon being scattered mostly in the forward direction (Ljungberg, 1998). The probability of this process increases with decreasing energy (E^{-1}), and increasing atomic number of the scattering atom (Z^2). Coherent scattering is important at relatively low energies, generally less than 50 keV (Cherry et al., 2003).

- Photoelectric effect

In the photoelectric effect an incident photon interacts with an atom, imparting all of its energy. A tightly bound inner orbital electron (known as a photoelectron) is ejected in the process. An electron from an outer orbit fills the vacancy by falling into the inner orbital 'hole'. This results in the emission of a characteristic x-rays equivalent to the difference in energy of the two orbital shells. The x-ray is known as characteristic because its energy is characteristic of the absorbing material (Brown et al., 2001).

The probability of the photoelectric effect is proportional to the cube of the atomic number (Z^3) and is inversely proportional to cube of the incident photon energy (E^{-3}). The photoelectric effect is the predominant interaction in NaI(TI) scintillation crystals

(Z=32) used in nuclear medicine and lead (Z=82), a commonly utilised attenuating material (Powser and Powser, 2006).

- Compton effect

The Compton effect describes the interaction between a photon and a loosely bound orbital electron. A proportion of the photon's energy is used to liberate the orbital electron from the atom. This results in a decrease of the incident photon energy. The energy lost by the incident photon via Compton scattering depends upon the angle through which it is scattered and may calculated using Equation 2.1:

$$\frac{1}{E} = \frac{1}{E_0} + \frac{1}{m_0 c^2}(1 - \cos\theta) \quad \text{...Equation 2.1}$$

where E is the Compton scattered photon energy, E_0 is the incident photon energy, θ is the scattering angle, m_0 is the rest mass of the electron and c is the speed of light (Brown et al., 2001).

The Compton effect is largely independent of the atomic number of the material and is inversely proportional to the energy of the photon (E^{-1}). It therefore predominates over the photoelectric effect for low atomic number materials such as soft tissues (Z=7.5) (Powser and Powser, 2006).

- Pair Production

Pair production is only possible when the energy of the incident photon exceeds the combined rest mass of an electron-positron pair (1.022 MeV). In the presence of the nucleus, an incident photon may create an electron-positron pair. Any excess photon energy is transferred as kinetic energy of the electron and positron and a portion may result in an excited nucleus state. High photon energies are required for this process to occur, well in excess of the maximum photon energies used for diagnostic nuclear medicine. The probability of pair production is proportional to the square of the atomic number (Z^2).

Figure 2.1 illustrates the predominant interactions based on the incident photon energy and atomic number of the material it traverses.

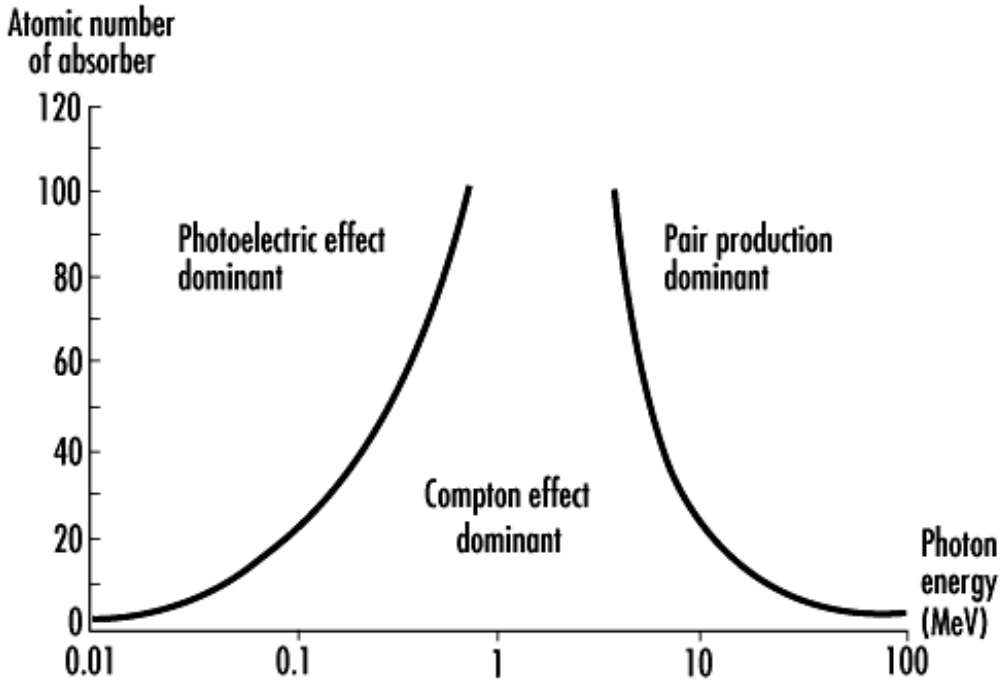

Figure 2.1: Predominant interactions based on the incident photon energy and atomic number of the material it traverses (Cherry, 2016)

The photon interactions with matter previously described result in a reduction in the flux of photons as they pass through the medium. The loss of photons is known as attenuation. The attenuation processes for narrow beam photon transport can be described by Equation 2.2.

$$I_x = I_0 e^{-\mu x} \quad \text{…Equation 2.2}$$

where I_0 is the incident intensity of the photons, I_x is the transmitted intensity, μ is the linear attenuation coefficient, and x is the thickness of the material.

An integral part of any Monte Carlo code is the ability to model physical interaction processes of photons within a material. As previously shown, the likelihood of a given interaction is dependent on the energy of the incident photon and the atomic number of the material through which it passes. In a Monte Carlo code, this information is provided by validated atomic interaction cross-section tables. Photon cross-sections for compounds can be provided by a weighted sum of cross-sections for the different atomic constituents (Ljungberg, 1998).

The cross-section data are used to create probability density functions which describe the likelihood of the physical processes.

2.2.2 Random number generator

The probability density functions must be sampled in some way to determine the photon's behaviour within a material. Sampling is undertaken based on the generation of random numbers. A truly random method for generating numbers (usually between 0 and 1) is impractical to realise and therefore a computational algorithm is adopted. The term *pseudo*- random number generator is therefore applied to computational algorithms for determining random numbers, the most common of which is the linear congruental algorithm. This provides a series of random numbers based on the initial value (known as the seed) as described by Ljungberg (1998):

$$I_{n+1} = (aI_n + b) mod (2^k) \text{...Equation 2.3}$$

where I_n is the initial seed value, I_{n+1} is the random number, k is the integer word size of the computer and a and b are constants. Normalisation of this integer series of random numbers can be undertaken to produce a set of random numbers in the range 0 to 1. To ensure a new sequence of numbers different to that produced previously requires a different seed value each time. There is also a potential risk that the initial seed may be generated in the number sequence; this will therefore result in a looping of the numbers generated (Ljungberg, 1998).

2.2.3 Sampling routines

Sampling routines are a key requirement for any Monte Carlo code; they are used to sample the various probability density functions that describe the photon transport and interactions. One such routine, based on the distribution function method, is the determination of the photon path length in a material before it undergoes an interaction. The probability function is exponential and dependant on both the material composition and photon energy (Ljungberg, 1998). For a photon travelling a distance of x or less, integrating the distribution yields the following equation:

$$x = -\frac{1}{\mu}\ln(R) \text{...Equation 2.4}$$

where *R* is a random number and μ is the macroscopic linear attenuation coefficient. A random number *R* can therefore be used to sample the path length of the photon before an interaction (Rogers and Bielajew, 1986). If the path length to an interaction is greater than the path length to a boundary, the photon will be moved to the boundary and the process repeated.

2.2.4 Tallies

The main aim of a Monte Carlo simulation is the production of a result, or tallies, once the program comes to completion. Tallies are the output a desired parameter under investigation in the Monte Carlo simulation. Tallies can be created for a wide range of different parameters. Tallies of particular interest to the work presented in this thesis include energy deposition in a region and pulse height distribution.

2.2.5 Variance reduction techniques

As with any computational simulation technique, the computing time taken to complete the simulations to an acceptable level of precision depends on the complexity of the modelled geometry and nature of the simulations. Most Monte Carlo codes provide some means of precision estimation. One such estimation of the precision is the relative error of the mean. The relative error is proportional to the inverse square of the number of histories simulated. Therefore a fourfold increase in histories will halve the relative error. If the tally in question has a low hit rate, then increasing the number of particles simulated is one method of achieving an acceptable precision. However, this may mean running the simulation for an unacceptably long time as the computing time is proportional to the number of particles simulated. Variance reduction techniques are therefore often employed to reach an acceptable precision for fewer histories, without distorting the physical processes. In the simplest form this may include a cut-off for photons, where photon energies lower than the cut-off values are no longer sampled if they will not contribute to the tallies. Other methods include geometry splitting, where particles entering geometries of importance in the simulation are split to create more particles, with the opposite being true for particles entering areas of low importance. Providing the tallies are modified by the splitting, this provides a method of increasing the histories in the region of interest and therefore reducing the time to reach an acceptable precision (X-5 Monte Carlo Team, 2003).

2.3 Monte Carlo codes

There are a number of different Monte Carlo codes available either commercially or freely distributed using a variety of different platforms. Three of the commonly utilised Monte Carlo codes for medical physics applications include MCNP5, EGS and Geant4. A brief précis of each code is presented here.

2.3.1 MCNP5

MCNP5 is a general-purpose Monte Carlo transport code that has been publically available for the longest period of time (Andreo and Ljungberg, 1998). The developers are based at the Los Alamos National Laboratory where some of the early work concerning Monte Carlo modelling was undertaken (while developing the atomic bomb during World War II). The transport modes that are available are photons, neutrons and electrons, which may be used independently or in some cases combined. Photon and electron energy ranges of 1 keV to 1000 MeV are used to simulate the transport of these particles (X-5 Monte Carlo Team, 2003). MCNP5 uses ENDF continuous-energy nuclear and atomic data libraries.

To run an MCNP5 program the user creates an input file which is read by the program. The user specifies variables such as;

- The geometry of the problem
- Descriptions of materials including density and atomic numbers
- Source specifications

- Tallies required
- Variance reduction techniques used to improve efficiency

MCNP5 has been utilised for a wide range of applications. Within medical physics, applications include absorbed dose assessments (Reed, 2007) and radiation detector design and analysis (Temple, 2007). The MCNP5 webpage hosts a range of validation documentation for the transport code (X-5 Monte Carlo Team, 2015). Currently, the distribution of MCNP5 is via application to the Radiation Safety Information Computational Centre, USA.

2.3.2 EGS

The EGS Monte Carlo code was first developed in the 1970's and originated from the Stanford Linear Accelerator Centre, USA (Andreo, 1991). Since then, the Monte Carlo code has gone through a number of iterations to its current forms. There are currently two main subsets of the EGS code that is maintained. EGS5 is maintained by the High Energy Accelerator Research Organization, Japan. It is a general purpose Monte Carlo simulation package which allows for the coupled transport of electrons and photons with energies ranging from a few keV to several hundred GeV (Hirayama et al., 2016). The EGS system is written in the MORTRAN computer language (Andreo and Ljungberg, 1998). EGSnrc is maintained by the National Research Council Canada and has been developed from the EGS4 code, the predecessor of both the EGS5 and EGSnrc codes. The stated coupled electron and photon energy ranges for EGSnrc is from 1 keV to 10 GeV (National Research

Council, 2015). Both EGS versions are freely available for download (KEK, 2016) (National Research Council, 2016).

The EGS Monte Carlo code has been employed for a wide range of medical physics problems. The EGSnrc code is distributed with BEAMnrc, which allows for the modelling of high energy photon and electron beams from radiotherapy linear accelerators and is one of the most popular codes for such applications (Verhaegen and Seuntjens, 2003). EGS5 has also been demonstrated to have particular applications for radiation protection. Kato et al. (2011) used EGS5 to calculate the personal dose equivalent for positron emitting radionuclides to estimate radiation dose.

2.3.3 Geant4

Geant4 is described as “a toolkit for simulating the passage of particles through matter” (Agostinelli et al., 2003). The Monte Carlo code has been produced collaboratively by a large number of multinational contributors and continues to be maintained and developed. In its current form, it is one of the more recently developed Monte Carlo codes (1990’s) compared to EGS and MCNP. It is object orientated and implemented in the C++ programming language (Agostinelli et al., 2003). This allows for additional features to be appended to the code by the user if desired. Low energy physics process models for photon transport down to 250 eV can be used (Chauvie et al., 2002). The source code is freely available for download from the Geant4 internet page along with user documentation (Geant4, 2016).

The Geant4 Monte Carlo code has been used for a range of applications including high energy physics simulations (e.g. simulating parts of the large hadron collider), space and radiation and medical physics (Geant4, 2013). A particular application using the underlying structures of Geant4 is GATE. GATE can be used to simulate diagnostic nuclear medicine equipment such as SPECT and PET imaging equipment (Jan et al., 2004). GATE also allows for the modelling of CT and external beam radiotherapy systems (Jan et al., 2011) as well as having potential applications for radiation therapy and dosimetry (Sarrut et al., 2014).

2.3.4 Monte Carlo code for subsequent investigations

The previous subsections give a brief introduction to three commonly utilised Monte Carlo transport codes for medical physics applications. Each of the Monte Carlo codes has stated photon energy ranges that cover the emissions of ^{123}I, which is subject to the simulations in this thesis. The purpose of the investigations, consistent with the proposed hypothesis, is to assess whether Monte Carlo techniques in general are suitable for simulating the uncertainties in ^{123}I assay and thyroid uptake measurement. MCNP5 is the code that has been available for the longest period of time and is extensively validated (X-5 Monte Carlo Team, 2015). Therefore, of the three codes, MCNP5 is used for the subsequent simulations.

Acquisition of the MCNP5 programme was via the Nuclear Energy Agency databank (applications to use MCNP5 must now be made to the Radiation Safety Information Computational Centre, USA). Simulations were undertaken on Windows™ (Versions XP and 10) based PC and laptop platforms.

CHAPTER 3: ASSAY OF RADIONUCLIDES

3.1 Introduction

Nuclear Medicine involves the administration of a radiopharmaceutical to a patient. The administration of any radioactive medicinal product is governed by the appropriate UK legislation. The legislations are designed to protect the patient from inappropriate procedures. Prior to any administration, the activity of the radiopharmaceutical must be assayed to ascertain the activity is as specified for the clinical procedure. The assay is undertaken on a radionuclide calibrator, an ionisation chamber designed to measure ionisation currents from radiation interactions.

This chapter introduces the legal requirements for the assay of radionuclides in the UK. The function of a radionuclide calibrator is then described followed by a description of the production and emissions of ^{123}I. Issues regarding the assay of ^{123}I are detailed along with currently adopted correction approaches. Finally, the aims of this portion of the thesis are outlined.

3.2 Legal requirements for accurate assay of radionuclides in the UK

There is a legal requirement in the UK to make an accurate assay of the total radioactivity administered to a patient for diagnostic or therapeutic purposes. The basis for the corresponding UK legislation stems from the European Union, namely the European Directive 97/43/Euratom (The Medical Exposures Directive) (EC, 1997). The Euratom Directive has been implemented in UK law via The Ionising Radiation (Medical Exposure) Regulations 2000 (UK Government, 2000) (as amended in 2006 (UK Government, 2006a) and 2011 (UK Government, 2011)). At the time of writing, a new Euratom Directive, Council Directive 2013/59/Euratom (EC, 2013), has been published. The new Euratom Directive must be implemented by member states (of which the UK is one) by the 6th February 2018.

The Ionising Radiation (Medical Exposure) Regulations 2000 (IRMER 2000) is concerned with medical exposures, occupational health surveillance, health screening programmes, medico-legal exposures and medical research. The regulations are enforced under the Health and Safety at Work Act 1974 with compliance delegated to the Care Quality Commission in England and the devolved administrations in Scotland, Wales and Northern Ireland.

IR(ME)R 2000 incorporates the concepts of optimisation and justification for medical exposures. An exposure may be justified if there is a net benefit to the patient from the exposure. The objective of the exposure, potential diagnostic or therapeutic benefits, detrimental effects and alternative techniques must be considered. In essence, justification is a cognitive process which is undertaken by the practitioner, an individual identified in IRMER 2000. In the particular case of nuclear medicine,

the ARSAC notes for guidance specify that the practitioner should be a doctor or dentist in possession of a certificate issued by the Secretary of State for Health in accordance with The Medicines (Administration of Radioactive Substances) Regulations 1978 (UK Government, 1978) (as amended 1995 (UK Government, 1995) and 2006 (UK Government, 2006b)).

The optimisation of exposures requires that the radiation detriment received by a patient is kept ALARP. For nuclear medicine procedures the detriment is typically quantified in terms of effective dose. Compliance with ALARP requires a multifactorial approach and depends on variables such as the radionuclide, the pharmaceutical, the age of the patient and the equipment used. One of the key factors in determining the radiation detriment to the patient and complying with the principles of ALARP is the activity of the radionuclide used for the investigation or therapy. The rate of radioactive decay, defined in terms of disintegrations per second (S.I. unit Bq), determines the rate of emission of ionising radiations. The higher the rate of emission, the more likely there will be an ionising interaction, which may result in a stochastic effect.

ARSAC through its notes for guidance recommends an appropriate activity to be administered for a given clinical investigation (ARSAC, 2016). The recommendations are based on scientific evidence relating the administered activity and image quality. The notes for guidance specify an upper recommendation of administered activity that is considered appropriate for a given diagnostic investigation. Under certain circumstances, exceeding this may be justified, for example, in patients with a high body mass index where the diagnostic quality of the image may be compromised

without a higher administered activity. The IRMER 2000 legalisation requires the documentation of local diagnostic reference levels. For nuclear medicine, this would be the activity administered to a patient for a given clinical investigation with reference to the ARSAC recommended activities. Once a diagnostic reference level has been specified, a tolerance of ±10% is acceptable for diagnostic procedures and ±5% for therapeutic procedures. The tolerances are applied to reflect uncertainties in the assay procedure and the inherent difficulties in providing radiopharmaceuticals to high precision (assuming an accurate calibration). Therefore, accurate assay of a radionuclide is critical in ensuring that the legislative requirements for ALARP can be realised.

3.3 Assay methodology

Primary techniques for the standardisation of radionuclide activity are held by the NPL in Teddington, UK. A number of instruments are employed to undertake the primary standardisation measurement. Typically, a radioactive sample is assayed using one of the primary techniques (e.g. coincidence counting) to determine the specific activity in the sample, expressed in terms of Bq g^{-1}, along with an associated measurement uncertainty. To ensure international standardisation of radionuclide sources, NPL works with other international metrological institutes to certify the primary standardisation techniques are comparable (NPL, 2015a). However, these primary techniques are complex, time consuming and expensive to administer. Therefore once a radionuclide has been assayed, it is used to calibrate secondary standard instruments or provide secondary standard sources for dissemination to end users. The secondary standard instruments are typically ionisation chambers suitable for the assay of radioactivity in vials or syringes. A typical calibration of a

secondary instrument would be as follows. Once the activity concentration of the sample is known, it is transferred to a secondary instrument in a standard container and volume. The ionisation current is measured and knowing the activity of the sample, a calibration factor can be derived to convert current to activity (Baker, 2005).

The basic components of an ionisation chamber consist of a sealed gas chamber, electrodes, electrometer, and display device (Figure 3.1). The gas is usually kept at a pressure several times that of the ambient atmospheric pressure (Gadd et al., 2006). The sealing of the chamber ensures that there are no variations in gas density that may have an adverse effect on the calibration. Furthermore, keeping the pressure of the gas somewhat higher than ambient pressure increases the linear attenuation coefficient for radiation interaction.

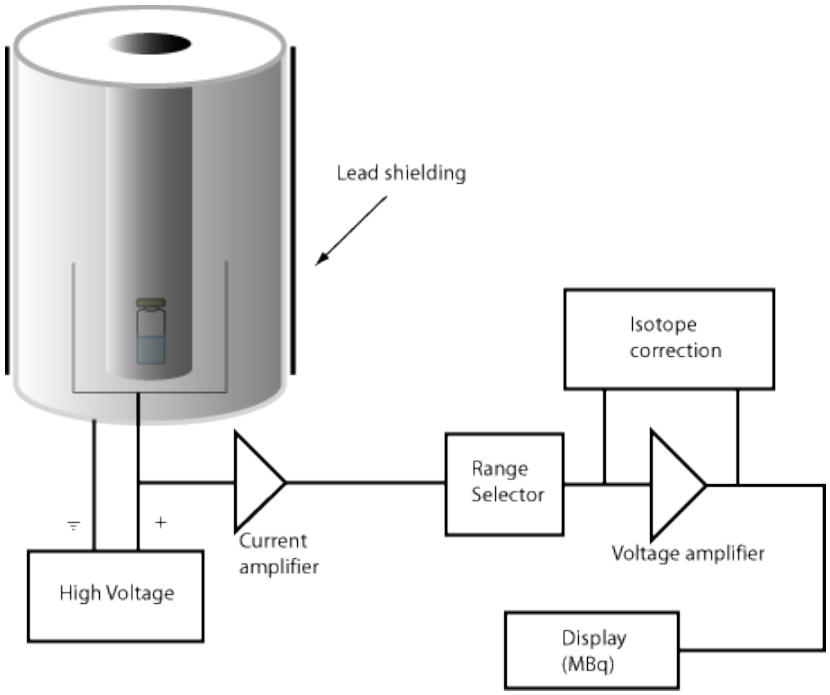

Figure 3.1: Schematic of a radionuclide calibrator (IAEA, 2015)

When a radioactive sample is placed within the chamber, some radioactive emissions may pass through the chamber wall and cause ionisation of the gas. Within the chamber there are also two electrodes kept at a potential difference of ~100 – 1000 V. The purpose of the electrodes is to collect the positive and negative ions created by the ionisation of the gas. The correct choice of potential difference between the electrodes is important to ensure that it is high enough to prevent recombination of the positive and negative ions, but insufficient to create further ionisation through acceleration of the arising ions. This ensures that there is a direct proportionality between the ionisation current induced and the energy deposited via ionisation in the chamber. The ionisation current generated is usually of the order of pA for medical radionuclide assay but a range of currents from pA to μA may be induced. A single electrometer may not be able to accommodate such a current range and so a number of electrometers may be employed for measurement, with electronics used to switch between them. Once the current is measured, a calibration factor must be selected to ensure that the measured current is properly converted to the activity for the particular radionuclide assayed. The calibration factor depends on several variables, with one of the primary variables being the energy of the radionuclide emissions. After the application of the calibration factor, the display unit is configured to display the activity in an appropriate unit.

A typical range of displayed activity units in nuclear medicine would be GBq to kBq. Measurement of activities lower than the order of kBq will suffer from high statistical variations due to the poor sensitivity of the electrometers to measure low ionisation currents. In such circumstances, a radionuclide calibrator would not be the ideal measurement device and an alternative detection system, such as a NaI(Tl) or HPGe detector would be more appropriate, provided that associated standard sources are available. Activities much greater than the order of GBq can be assayed on a radionuclide calibrator, but the lack of requirement for such activities in a medical context and the associated radiation protection issues makes this activity redundant.

The secondary standard instrument held by NPL is known as the Fidelis Secondary Standard Radionuclide Calibrator (Figure 3.2). The Fidelis comprises the NPL-designed nitrogen filled ionisation chamber and an electrometer and user interface unit from Southern Scientific Ltd. (NPL, 2015b). The Fidelis is provided with a database of traceable calibration factors to the NPL primary standardisations. Each calibration factor can be retrieved by the display software when a particular radionuclide, container and volume are selected. A number of Fidelis calibrators have been built to the same specification as the master Fidelis chamber held at NPL and are available for purchase by nuclear medicine or other departments.

Figure 3.2: Fidelis secondary standard radionuclide calibrator (NPL, 2015b)

Before installation at the department, the chamber is checked against the master chamber at NPL to ensure that the responses are equivalent. This ensures that for the factor database generated for the master chamber is applicable to other Fidelis chambers. The factor database is editable by the user, which allows the addition of new calibration factors when they are published by NPL (available from the NPL website (NPL, 2015c)). Caution must always be exercised when editing the database to ensure typographical errors are not introduced which may comprise the validity of the calibration factors. Periodically, a new database may be disseminated by NPL to Fidelis users. Once disseminated into nuclear medicine departments, the Fidelis chambers provide a means of assay traceability to the primary methods for standardisation.

The Fidelis is relatively expensive and is not an instrument of choice for the routine assay of radionuclides in a nuclear medicine department. For example, a regional medical physics department may have one Fidelis calibrator but may need 10 – 20 for routine radionuclide assay. In this case, field radionuclide calibrators are employed. Field instruments are produced by a number of manufacturers including Capintec, Biodex, Veenstra and PTW. Again, the basic design of the calibrators is consistent with that previously described. There may also be subtleties in the dimensions of and the materials used for each of the manufacturers calibrators.

One of the main differences between the Fidelis and a field instrument is the number of available calibration factors for the user to select. Generally, a field calibrator will have one factor for a given radionuclide.

Calibration factors will have been generated from measurements in a particular container and volume [consideration throughout is only given for radionuclide solutions]. However, calibration is dependant not only on the emissions, but also on the container material, the geometry of the container and also the volume of the solution. Such variables and their impact on the calibration of a radionuclide calibrator are discussed in detail in the NPL Measurement Good Practice Guide No. 93: Protocol for Establishing and Maintaining the Calibration of Medical Radionuclide Calibrators and their Quality Control (Gadd et al., 2006). The Fidelis has a number of container and volume combinations. To ensure that the field chamber is accurate for different containers and volumes, inter-comparison exercises must be undertaken to cross-calibrate the Fidelis against a field chamber. This would consist of taking a radioactive sample, measuring it in the Fidelis chamber and then measuring it in the

field chamber. A comparison of measurements, appropriately decay corrected, will yield a ratio of the Fidelis to field chamber measurement. This may then be the basis of implementing a new calibration factor or the introduction of a correction for an existing calibration factor.

3.4 ^{123}I production

The predominant mode of production of ^{123}I is using a cyclotron (Guhlke et al., 2007). There are two main cyclotron routes to producing ^{123}I following proton, deuteron or helium irradiation, either directly or via the intermediate production of ^{123}Xe. The first two production modes in Table 3.1 show the nuclear reactions involving ^{123}Xe (IAEA, 2009). Both of the xenon-123 routes can produce high purity ^{123}I as the ^{123}Xe can be chemically separated from the target material and allowed to decay to ^{123}I. However, as can be seen from Table 3.1, this route does require large irradiation energies, generally only achievable by cyclotrons located in large research facilities. The most commonly adopted route of ^{123}I production is via the ^{124}Te(p, 2n)^{123}I reaction by irradiating high purity ^{124}Te with protons (IAEA, 2009). Following irradiation, the ^{123}I is chemically extracted from the target material. Figure 3.3 shows the excitation function for the ^{124}Te(p, 2n)^{123}I reaction. The notable advantage of this production route is that much lower cyclotron energies may be employed for the reaction. This is more suitable for industrial level production cyclotrons found in commercial production facilities (Guhlke et al., 2007). However, ^{125}Te impurities in the target material will result in the production of ^{124}I via the ^{125}Te(p, 2n)^{124}I reaction. Their abundance at production is low compared to the total ^{123}I activity. However, because of the longer half-life of ^{124}I (4.2 days) compared to ^{123}I (13.2 hours), the proportion of the impurity increases over time.

Nuclear reaction	Useful energy range (MeV)	Natural abundance of target material (%)
$^{127}I(p, 5n)^{123}Xe:^{123}I$	55+	100
$^{127}I(d, 6n)^{123}Xe:^{123}I$	83	100
$^{122}Te(d, n)^{123}I$	14–8	2.4
$^{123}Te(p, n)^{123}I$	15–8	0.87
$^{124}Te(p, 2n)^{123}I$	26–20	4.6
$^{124}Xe(p, pn)^{123}Xe:^{123}I$	15–30	0.10
$^{121}Sb(^{4}He, 2n)^{123}I$	15–25	57.4
$^{123}Sb(^{3}He, 3n)^{123}I$	20–30	42.6

Table 3.1: Nuclear reactions to produce ^{123}I (IAEA, 2009)

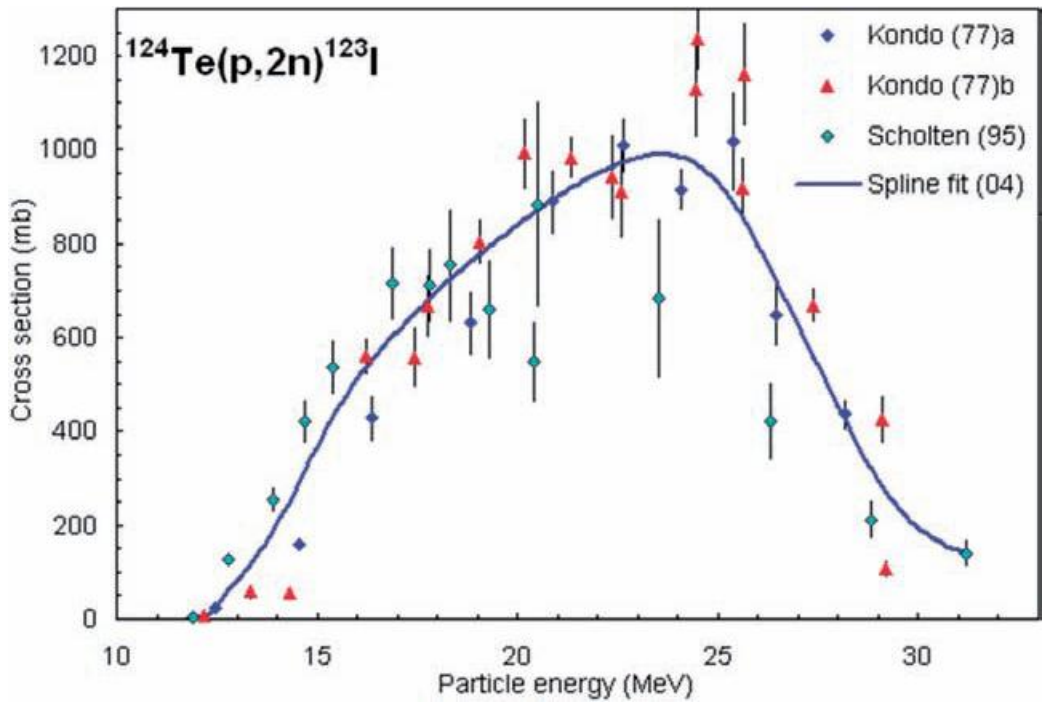

Figure 3.3: Excitation function for the $^{124}Te(p, 2n)^{123}I$ reaction (IAEA, 2009)

3.5 ^{123}I decay scheme

The routine assay of ^{123}I poses particular problems. Clarification of this statement requires a detailed analysis of the decay scheme and the principal energies and emission probabilities of ^{123}I as seen in Figure 3.4 and Table 3.2.

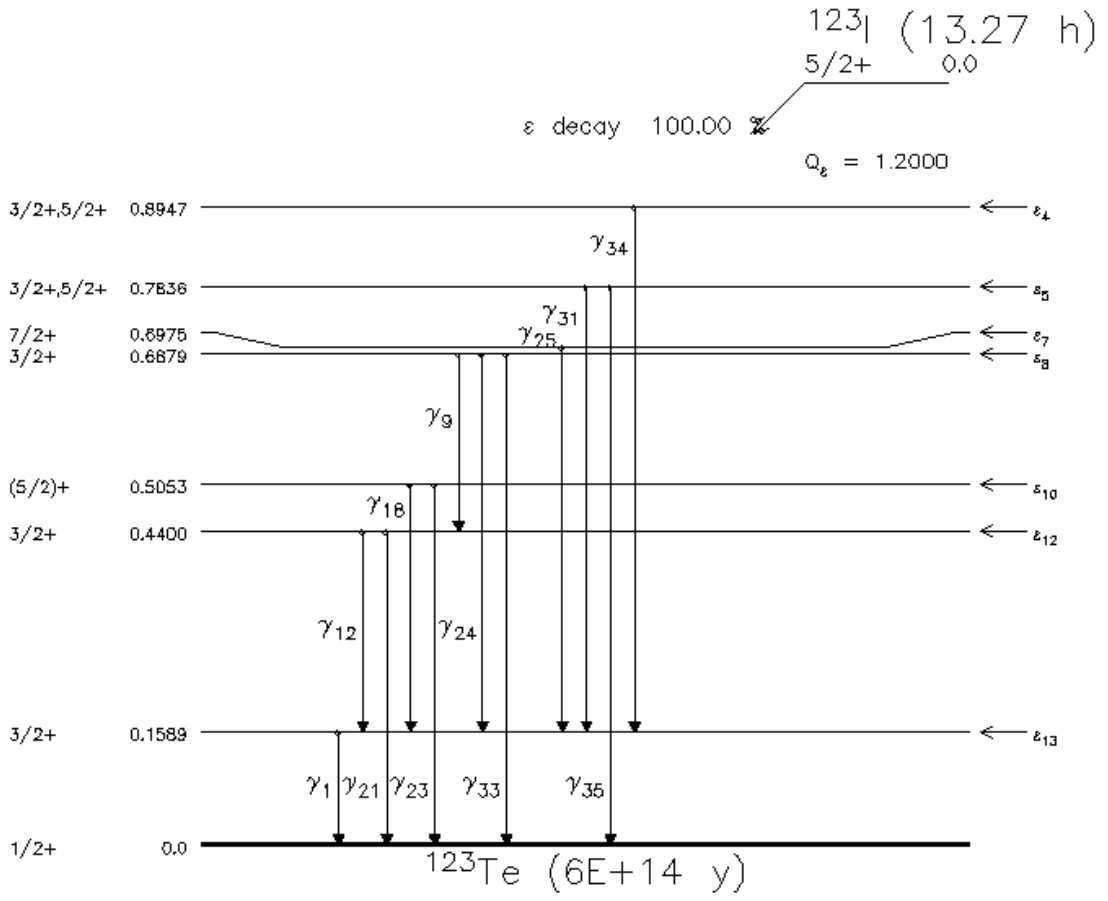

Figure 3.4: Decay scheme for ^{123}I (ORAU, 2015)

Radiations	y(i) $(Bq\text{-}s)^{-1}$	E(i) (MeV)	y(i)×E(i)
gamma 1	8.28×10^{-01}	1.590×10^{-01}	1.32×10^{-01}
ce-K, gamma 1	1.35×10^{-01}	1.272×10^{-01}	1.72×10^{-02}
ce-L, gamma 1	1.60×10^{-02}	1.540×10^{-01}	2.47×10^{-03}
ce-M, gamma 1	3.46×10^{-03}	1.582×10^{-01}	5.48×10^{-04}
ce-N+, gamma 1	8.27×10^{-04}	1.590×10^{-01}	1.32×10^{-04}
gamma 9	7.07×10^{-04}	2.480×10^{-01}	1.75×10^{-04}
gamma 12	7.86×10^{-04}	2.810×10^{-01}	2.21×10^{-04}
gamma 18	1.25×10^{-03}	3.463×10^{-01}	4.33×10^{-04}
gamma 21	4.25×10^{-03}	4.400×10^{-01}	1.87×10^{-03}
gamma 23	3.14×10^{-03}	5.053×10^{-01}	1.59×10^{-03}
gamma 24	1.38×10^{-02}	5.290×10^{-01}	7.31×10^{-03}
gamma 25	3.79×10^{-03}	5.385×10^{-01}	2.04×10^{-03}
gamma 31	8.28×10^{-04}	6.246×10^{-01}	5.17×10^{-04}
gamma 33	2.66×10^{-04}	6.879×10^{-01}	1.83×10^{-04}
gamma 34	6.12×10^{-04}	7.358×10^{-01}	4.50×10^{-04}
gamma 35	5.90×10^{-04}	7.836×10^{-01}	4.62×10^{-04}
Kalpha1 X-ray	4.58×10^{-01}	2.747×10^{-02}	1.26×10^{-02}
Kalpha2 X-ray	2.46×10^{-01}	2.720×10^{-02}	6.70×10^{-03}
Kbeta1 X-ray	8.66×10^{-01}	3.100×10^{-02}	2.69×10^{-03}
Kbeta2 X-ray	2.66×10^{-02}	3.171×10^{-02}	8.43×10^{-04}
Kbeta3 X-ray	4.46×10^{-02}	3.094×10^{-02}	1.38×10^{-04}
Auger-LMX	3.11×10^{-01}	3.849×10^{-03} *	1.20×10^{-03}
Listed X, gamma, and gamma$^{\pm}$ Radiations			1.71×10^{-01}
Omitted X, gamma, and gamma$^{\pm}$ Radiations**			6.76×10^{-04}
Listed beta, ce, and Auger Radiations			2.80×10^{-02}
Omitted beta, ce, and Auger Radiations**			1.21×10^{-04}
Listed Radiations			1.99×10^{-01}
Omitted Radiations**			7.97×10^{-04}

* Average Energy (MeV).

[a] Maximum Energy (MeV) for subshell.

** Each omitted transition contributes <0.100% to Sum of y(i)×E(i).

Table 3.2: Emissions of ^{123}I (ICRP, 1983). Y(i) is the yield per disintegration, E(i) is the energy of the emission, y(i)×E(i) is the sum of the yield and the energy of the disintegration and ce are conversion electrons

^{123}I decays 100% via electron capture to ^{123}Te which is a stable nuclide. The principal gamma energy (gamma 1) is 159 keV. For diagnostic nuclear medicine purposes, this is the gamma photon that is used for detection as it falls within the 80 – 400 keV range, which is ideal for detection using a NaI(Tl) scintillation crystal. There are a number of other gamma emissions in the decay scheme. They are generally at a higher energy than the principal gamma emission but notably at a much reduced yield, typically 100-1000 times less abundant as compared to gamma 1. The decay of ^{123}I is also characterised by the emissions of K-alpha and K-beta characteristic x-rays at energies ranging from 27 – 31 keV with a combined abundance of 86.2%.

3.6 Uncertainties associated with ^{123}I assay

Field radionuclide calibrators generally only provide one calibration factor, typically for a standard glass vial, for any given radionuclide. The decay scheme for ^{123}I has been shown to present particular problems for the accurate assay of a sample of this radionuclide. The difficulty in accurately assaying a sample of ^{123}I primarily stems from the emissions associated with the characteristic x-rays.

Wiarda (1984) identified that a large portion of characteristic photons are absorbed in a glass vial due to a increase in the mass attenuation of glass towards low energy photons at around 30 keV. Wiarda (1984) also showed that up to 80% of the total response from ^{123}I is due to the characteristic x-rays. However, the type of radionuclide calibrator and specifications of the vials were not disclosed. In a paper published the same year, Harris et al. (1984) reported similar findings, in that up to 70% of the chamber response was due to the characteristic x-rays. The authors

identified their radionuclide calibrator as a argon filled Capintec CRC-5. In a more recent paper, Tyler and Woods (2003) reported a difference in chamber response of up to 60% between a P6 vial and a 5ml syringe. This response was documented for an argon filled ARC 120 calibrator. Thompson et al. (1997) also described experiences at their centre where there was a large variation in readings compared to the expected values. Vials tended to read 25% below the expected value and syringes tended to read 27% higher than the expected value.

It is clear from previous publications that the assay of ^{123}I is problematic, particularly when moving from a glass vial to a syringe. The degree of variation in measurement may not only depend on the type of material used to house the radionuclide but also the particulars of the radionuclide calibrator design and material composition. Manufacturers predominately calibrate their radionuclide calibrators for a standard vial. However, once dispensed, the activity is usually measured in a syringe. The assay of ^{123}I in a syringe on a radionuclide calibrator with a factor specified for a vial could potentially result in an overestimation of the activity in the syringe in the region of 60% - 80%. Such an overestimation would mean that the patient would receive less than half of the prescribed activity. This may have a detrimental effect on the image quality or the ability to achieve a diagnostically reliable result. Repeated investigations may actually result in a higher radiation detriment than otherwise would have been received.

To ensure an accurate assay of ^{123}I, the options for a field radionuclide calibrator are to use an individually derived calibration factor for each container, a individually derived multiplicative correction factor for each container or a filtering system designed to negate the effects of the characteristic x-rays.

The first two options can be undertaken using the following process. Firstly, a homogenous stock solution of ^{123}I can be produced in a volume larger than all the samples required for measurement. A standard volume of the solution can be dispensed into a glass vial for which the calibrator has a traceable calibration factor. This sample is assayed in the calibrator using this factor to determine the activity concentration of the solution. Further samples can then be sub-dispensed from the stock solution into the various syringes and other containers that are used clinically. As the activity in each syringe can be calculated from the volume dispensed, individual calibration factors can be derived for each container, or a correction factor derived with respect to the reading made on the vial calibration setting. One of the main issues with such a process is that there are a large number of different syringe and volume combinations to consider when undertaking such an exercise. The result is there are also a large number of calibration factors or correction factors to consider. This may lead to the potential for the wrong calibration or correction factors being selected.

The third option, the use of a filtering system, is one that has been investigated in the literature. The principle of a filtering system is to use an absorbing material to selectively attenuate the low energy characteristic x-rays while permitting a measureable portion of the main gamma radiation to transmit to the radionuclide

calibrator. One of the first examples of use of such a material was documented by Wiarda (1984). Wiarda (1984) used a copper filter of thickness 1 mm and placed sources containing ^{123}I, ^{127}Xe or ^{133}Xe into the well of a radionuclide calibrator. Measurements demonstrated a significant reduction in the characteristic x-ray peak while allowing 93% of the 159 keV gammas to pass through. Since this time, the use of a copper filter has found widespread application for not only the assay of ^{123}I but also for ^{111}In. Kowalsky and Johnson (1998) undertook some practical work with ^{125}I as a mock radionuclide for ^{123}I to determine the optimal thickness of a copper filter. They found that the transmission of the x-rays fell below 1% when using a copper thickness of 0.6 mm. Harris et al. (1984) also showed that thicknesses of copper of the order of 0.5 mm was sufficient to reduce penetration of the x-rays to less than 1%. Kowalsky and Johnson (1998) also specifically looked at the activity variations with 1 ml, 3 ml and 10 ml syringes and a 10 ml vial for an argon filled Capintec calibrator. For the same volume, they found that the largest variation of 44% was seen when comparing a 1 ml syringe with the manufacturers recommended calibration factor. When using 0.64 mm of copper, the variation in activity measured in all containers decreased to below 3%.

From a practical perspective, the use of a filtering system such as copper has some distinct advantages over the use of individual calibration factors. A single factor can be determined that allows assay of all material types. From the current literature, those calibrators identified typically were argon filled field chambers.

Monte Carlo models for a radionuclide calibrator have been described in the literature previously. Laedermann et al. (2004) undertook a Monte Carlo simulation using GEANT 3 of an argon filled Veenstra VDC-405 radionuclide calibrator. The authors were able to reproduce the response of the detector and validate their results against practical measurements. Olsovcová (2010) undertook a Monte Carlo simulation of an argon filled radionuclide claibrator with vial and syringe geometries containing ^{111}In, ^{123}I and ^{153}Sm. The author was able to estimate uncertainties for this particular chamber when assaying with a vial and syringe and determined an appropriate copper filter thickness for correction.

3.7 Aims of Monte Carlo radionuclide calibrator simulations

The influence of a copper filter to differentiate the characteristic x-rays on a nitrogen filled NPL chamber has not been investigated. Furthermore, calibration factors for syringes do not appear in the official list of approved calibration factors published by NPL (NPL, 2015c). Syringe calibration factors for the NPL secondary standard calibrator have been previously published (Tyler and Woods, 2003) and are detailed in a NPL report (Tyler and Woods, 2002). However, users of Fidelis calibrators were notified via private correspondence that the syringe calibration factors were placed under review in 2008 and should not be used. Furthermore, additional correspondence with NPL in 2016 indicated that syringe calibration factors are unlikely to be included in any forthcoming Fidelis database dissemination. Investigating ^{123}I assay using the NPL nitrogen filled Fidelis calibrator forms the basis of the initial Monte Carlo simulations.

CHAPTER 4: MONTE CARLO SIMULATION OF A FIDELIS RADIONUCLIDE CALIBRATOR

4.1 Introduction

In the previous chapter the aims of the initial investigations were outlined to encompass the Monte Carlo modelling of a Fidelis radionuclide calibrator. In this chapter the performance specifications of a Fidelis radionuclide calibrator are outlined and assessments undertaken to ascertain current performance. The material and geometric compositions of the Fidelis radionuclide calibrator are detailed and a Monte Carlo model of the Fidelis was created. Initial simulations were undertaken to produce a sensitivity curve to characterise the performance of the Fidelis. Finally, validation of the Monte Carlo model was undertaken for a selection of radionuclides via comparison with the published NPL calibration factors.

4.2 Fidelis secondary standard calibrator performance specifications

The Fidelis is manufactured by Southern Scientific Ltd. and comprises a well type ionisation chamber connected to a laptop computer with associated software. The chamber is the same as the NPL calibrator type 271 described by Woods et al. (1983). In the paper the authors describe the requirements for which the calibrator was designed:

- Traceability to NPL national standards of radioactivity
- Separate and universally interchangeable ionisation chamber and electrometer modules
- Ionisation chamber to have the same calibration figures within ±0.2% for ^{60}Co, ±1% for ^{57}Co and ±6% for ^{125}I
- Response to be independent of pressure and temperature variations
- Maximum error due to saturation losses for 10 GBq of ^{99m}Tc to be not greater than 1%
- Accuracy of current measurement to be within ±1% for currents greater than 1pA

The Fidelis is a sealed, concentric cylinder type of calibrator and it is predominantly constructed of aluminium alloy. The chamber is filled with dry nitrogen to a pressure of 1 MPa. A polarising voltage of 1450 V is applied between the cathode and anode within the chamber (Woods et al., 1983). The electrometer integrated into the base of the chamber is the 'new state-of-the-art, high resolution, Pam Electrometer module' with a documented linearity to within ±1% (Southern Scientific Ltd., 2009).

A key parameter of a radionuclide calibrator is that the chamber is linear over a wide range of activity. This is particularly important when comparing measurements with Monte Carlo simulation, which is not subject to linearity issues due to sequential particle sampling. Woods et al. (1983) demonstrated that the chamber was linear up to an activity of 100 GBq of ^{99m}Tc (only 1% current loss observed). This value is generally in excess of what would be assayed for administered activities.

Woods et al. (1983) also demonstrated good reproducibility between different type-matched chambers. Reproducibility is an important factor in ensuring that calibration factors derived for the primary chamber are equally applicable to other type-matched chambers.

The Medical Physics Department at the University Hospital of Wales purchased a Fidelis system in 2009 (S/N 06049). When comparing a Monte Carlo model with Fidelis performance, it is important to ensure that the chamber is operating within its specified tolerances. This is particularly pertinent if the Monte Carlo model is used to derive new calibration factors. In terms of ensuring a good correlation between the Monte Carlo model and the physical system, the main performance characteristics include accuracy of the calibration factors (which relates to reproducibility between chambers) and activity linearity. These performance characteristics are considered in turn.

4.3 Reproducibility of the Fidelis

Before purchase, the Fidelis chamber was checked against the master chamber at NPL to ensure the response of the instrument was within specification. Five radioactive sources were assayed in the chamber and compared with the NPL master chamber. The ratio of the current measurements must be within the compliance ratio as specified in Table 4.1. The variation in current measurements was also checked between the NPL electronics and the Fidelis electronics. As can be seen by the results in Table 4.1, the specification was met or exceeded in all cases.

Radionuclide	Compliance ratio requirements	Test chamber current/standard chamber current	Expanded uncertainty	% difference between test chamber current measurements using NPL and Fidelis electronics
^{125}I	0.96 – 1.04	0.9933	±0.0087	-0.36%
^{241}Am	N/A	1.00265	±0.0029	-0.45%
^{57}Co	0.99 – 1.01	1.0076	±0.0030	-0.51%
^{137}Cs	N/A	1.0005	±0.0029	-1.03%
^{60}Co	0.997 – 1.003	1.0000	±0.0029	-0.50%

Table 4.1: Acceptance test results for the Fidelis S/N 06049

Continued assurance that the Fidelis is stable was provided by routine quality control protocols. The Fidelis has an in-built quality control routine that assess the amplifier offset, ambient background radiation levels and high voltage values. In addition, the response of the calibrator is checked using a 10 MBq ^{137}Cs sealed source, which

was initially assayed on the chamber by NPL. The constancy of the chamber response for the sealed source was assessed and has remained predominately within the specified tolerance of ±2% since purchase.

4.4 Accuracy of the Fidelis calibration factors

The calibration factors for each radionuclide and container combination are expressed in terms of the ionisation current (pA) per MBq of activity and are published on the NPL website (NPL, 2015c). Each calibration factor is published along with an associated uncertainty. For a P6 or Schott vial, the calibration factors issued by NPL are 1.685 pA/MBq ± 0.84% and 1.721 pA/MBq ± 0.90% respectively for 4 ml of ^{123}I.

A national inter-comparison exercise to assess the accuracy of hospital radionuclide calibrators for ^{123}I was conducted by NPL in November 2015. The Medical Physics Department at the University Hospital of Wales participated in the inter-comparison. Each department was issued with a Schott vial containing 4 ml of an ^{123}I solution. The solution was assayed using a number of field calibrators in the Department and also using the Fidelis. Following measurement and return of the results, a provisional vial activity value has been provided by NPL. The provisional results for the assay of a Schott vial containing 4 ml of ^{123}I (calibration factor 1.721 pA/MBq) are summarised in Table 4.2. The results show that the Fidelis is accurate to within +0.8% for an ^{123}I measurement in a Schott vial. As the calibration factors are within 2.2% for a Schott vial and a P6 vial, the implication is that a similar accuracy would be achieved with a P6 vial.

Fidelis measurement time	Fidelis reading (MBq)	Decay corrected activity to reference time (MBq)	Average activity (MBq)	% difference between NPL measured activity and Fidelis measured activity
11/11/2015 14:39	105.9	104.0	103.9	0.75%
11/11/2015 14:39	105.8	103.9		
11/11/2015 14:39	105.8	103.9		

Table 4.2: Results from a national inter-comparison exercise for ^{123}I undertaken in November 2015. The results show a less than 1% variation in the response of the Fidelis chamber compared to the national standard measurements and within the accuracy uncertainty stated for the calibration factor

4.5 Activity linearity of the Fidelis

An activity linearity assessment was undertaken using an elution vial containing a 10 ml solution of ^{99m}Tc with an initial activity of 12 GBq. The vial was placed in the well of the chamber and the Fidelis software used to log activity measurements every 100 seconds over the course of 65 hours.

Figure 4.1 shows the decay of the ^{99m}Tc sample over the duration of the assessment. As expected, the curve indicates exponentially decreasing activity.

Figure 4.2 shows the natural logarithm of the measured activity against time. The gradient of the linear best fit line corresponds to the decay constant for ^{99m}Tc. From this the half-life may be derived.

The half-life was calculated to be 6.025 hours, +0.3% from the expected value of 6.007 hours (Chiste et al., 2004). Acceptable linearity tolerances are specified in the NPL Measurement Good Practice Guide No. 93 (Gadd et al., 2006). The tolerance specified by Gadd et al. (2006) for a reference instrument is ±1%. The Fidelis also does not display any significant electrometer range changing discrepancies, which can result in errors when assaying either side of electrometer auto-ranging. This therefore means that the Fidelis is performing within the expected linearity tolerance over a wide range of activity.

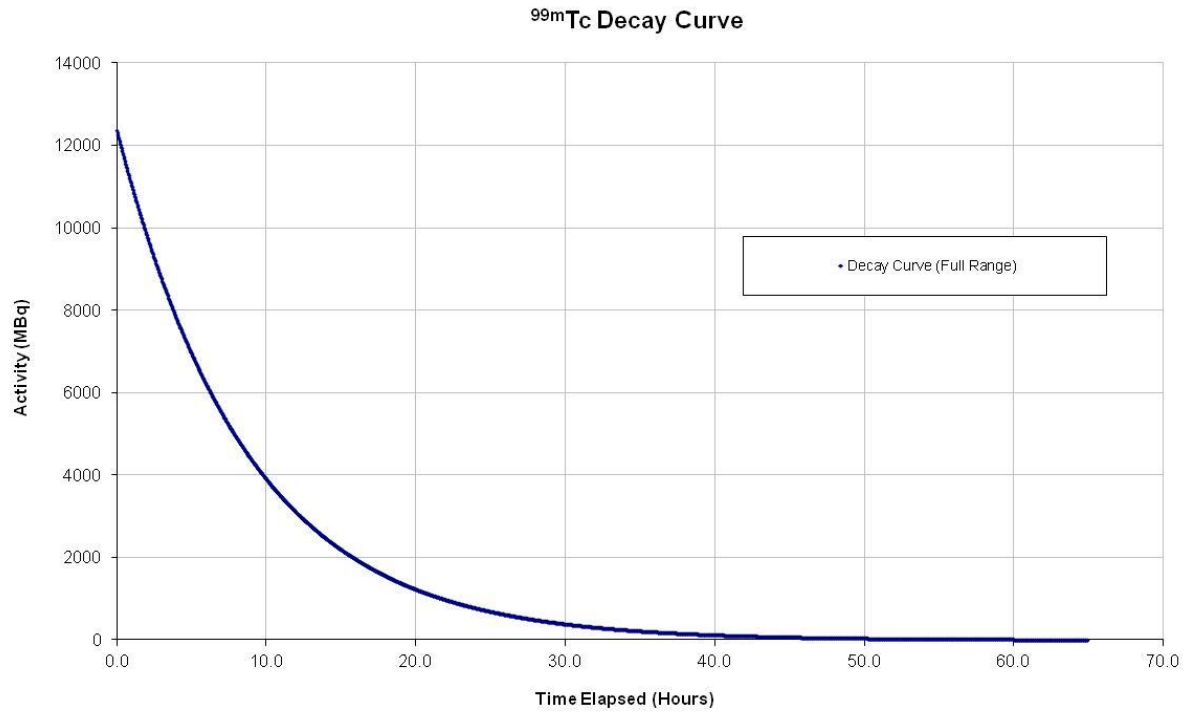

Figure 4.1: Fidelis decay curve for ^{99m}Tc

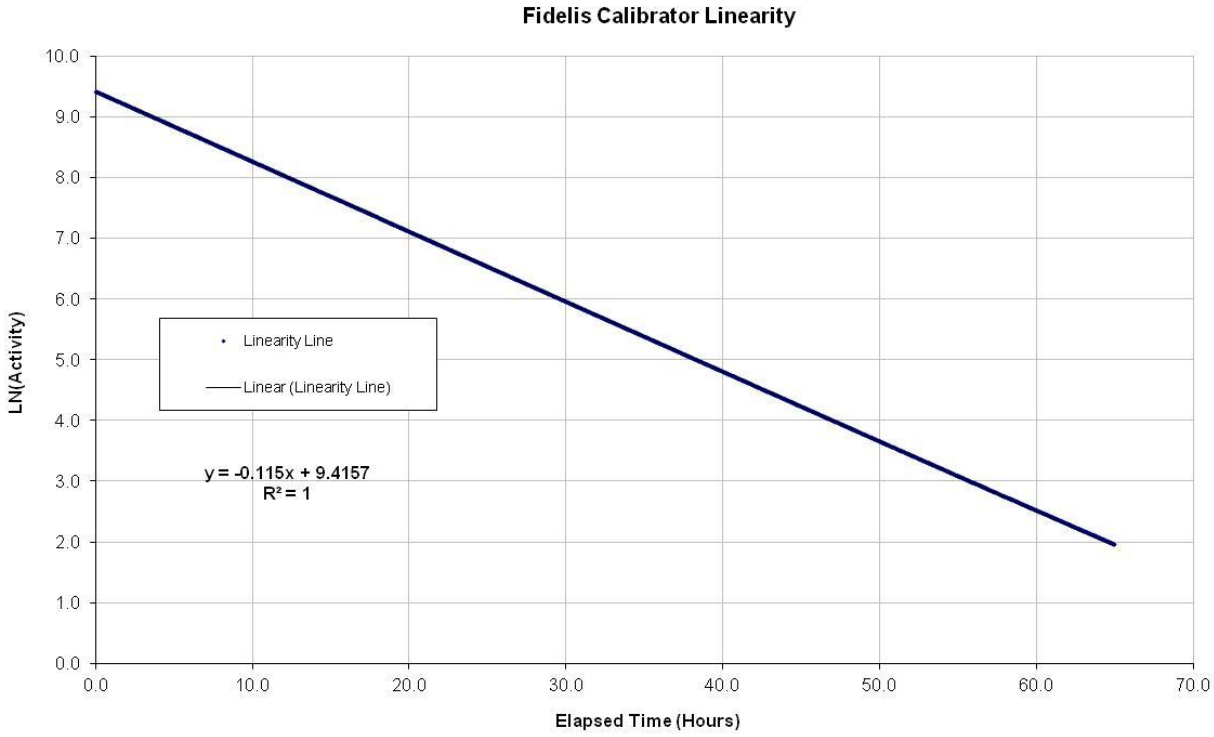

Figure 4.2: Determination of the half-life is achieved by using the decay constant as specified as the gradient of the straight line fit

4.6 Geometric structure of the Fidelis

Monte Carlo modelling of the Fidelis requires detailed knowledge of the materials and geometries of the system. Access to such information is commercially sensitive and therefore estimations have been made where appropriate.

The main component of the Fidelis that can be modelled is the chamber. The particulars of the electrometer are not important from a modelling perspective, as previously shown, the Fidelis displays activity linearity within the required specification.

The basic components of the chamber are the inner tube, outer tube, electrode, base and top. The dimensions of the various components are detailed in Table 4.3. The Fidelis has various connections from the electrode to the electrometer that are not replicated in the model. These additional connections represent a small total area of the sensitive volume under investigation and their effect is assumed to be negligible from a modelling perspective. As can be seen, each of the core components can be modelled as a series of cylindrical objects.

Component	Length (cm)	Diameter (cm)	Thickness (cm)
Inner tube	37.8	7.5	0.1
Outer Tube	36	19	0.25
Electrode	30	13	0.1
Base	1.9	19	0.1
Top	1.4	19	0.1

Table 4.3: Dimensions of the core components of the Fidelis chamber

The two other aspects of the Fidelis that require modelling are the jig and radioactive sample containers. The jigs are designed to ensure reproducible positioning of the sample container within the well of the chamber. Three jigs were supplied with the Fidelis, one for a 10 ml P6 vial, one for a 10 ml Schott vial and a jig for capsules. No jigs for the reproducible positioning of syringes within the chamber were supplied.

The validation was undertaken using the P6 jig supplied with the calibrator and a radionuclide solution within a P6 vial. The P6 jig has an internal diameter of 5.6 cm and a length from the base of the holder to the top of 21 cm. The internal diameter of the opening at the top of the P6 vial is taken to be 1.275 cm. The thickness of the main body of the vial is taken to be 0.12 cm.

4.7 Material composition of the Fidelis

Specifications for the materials were supplied by NPL and the manufacturers of P6 vials. The Fidelis chamber is primarily constructed of aluminium alloys as specified in the appropriate BS. Table 4.4 shows the material composition of the chamber (current BS is also noted).

Element	Top and Bottom	Outer Tube	Inner Tube	Electrode
	BS 1470 NS4 H6 (5251)	**BS 1471 HT30 (6082)**	**BS 1471 HT9 (6063)**	**BS 1470 S1B**
Aluminium	96.7	97.15	97.65	99.5
Silicon	0.4	0.7	0.2	0.15
Iron	0.5	0.5	0.5	0.15
Copper	0.15	0.1	0.1	0.05
Manganese	0.1	0.4	0.4	0.05
Magnesium	1.7	0.6	0.6	-
Chromium	0.15	0.25	0.25	-
Zinc	0.15	0.2	0.2	0.1
Titanium	0.15	0.1	0.1	-
Density ($g\ cm^{-3}$)	2.69	2.70	2.70	2.71

Table 4.4: Table of materials

The inner containment of the calibrator is filled with nitrogen gas to a pressure of 1 MPa. The Monte Carlo simulation requires materials to be specified in terms of density as opposed to pressure. The density of a gas can be calculated using the relationship:

$$P = R \times \rho \times T \quad \text{....Equation 4.1}$$

where P is the pressure (Pa), R is the individual gas constant (J kg^{-1} K^{-1}), ρ is the density (kg m^{-3}) and T is the temperature of the gas (K). Taking the pressure to be 1 MPa, the individual gas constant as 296.8 J kg^{-1} and the temperature as 294 K (taken to be 21 °C), the density of the nitrogen gas is calculated to be 0.01146 g cm^{-3}. This value is approximately ten times higher than the normal atmospheric density.

The P6 jig is modelled as PMMA with a density of 1.19 g cm^{-3} and the P6 vial is modelled as glass with a density of 2.40 g cm^{-3}.

4.8 Monte Carlo Fidelis model

The basic format of an MCNP5 input file consists of a text file composing the cell cards, surface cards, material cards and source definition. A detailed description of the MCNP5 input file for the Fidelis is provided in this section.

4.8.1 Cell card

The first section in the MCNP5 input file (cell cards) describes the cell information within the geometry.

```
Fidelis calibrator
c This is a model of the Fidelis Calibrator
c Cell card
    2     1 -0.0012 -2 #3 #4 #5 #6 #7 #8 #9 #10 #11        $universe
    3     3    -2.7 -3 4                                   $outer tube
    4     2   -2.69 (-5 :-6 )7 8 17 15 30                 $top plate
    5     4    -2.7 -7 8                                   $inner tube
    6    10   -2.71 -9 10                                  $electrode
    7     2   -2.69 (-11 :-12 )7                          $base plate
    8     5   -1.19 (-13 :-15 :-19 :-21 )14 16 18 20 31   $P6 jig
    9     9    -2.4 (-24 :-26 :-22 )28 23                 $P6 vial
   10     7      -1 -29                                    $radionuclide solution
   11     8 -0.01146 -4 7 #6 #4 #7                         $nitrogen gas
   12     0         2                                      $outside world
```

In the above example there are 11 separate cells that make up the geometry. The first column details the cell numbers, 2 through to 12. The second column details the material number that will be ascribed to the cell in the model. The materials are defined later in the input file. The third column details the density of the cell. A minus sign in front of the density value indicates the density is defined in g cm^{-3}. The numbers following the density value define the construction of the cell based on the

combination of surfaces that are defined in the surface card later on in the input file. A negative number identifies the internal aspect of surfaces and a positive number the external aspect. For example, the outer tube is defined as cell number 3, consisting of material number 3, a density of 2.7 g cm^{-3} and is defined as the closed region inside surface number 3 and outside surface number 4. Cell 8 is an example where a union of surfaces is used to define a complex geometry. Cell number 2 defines the limits of the modelled world. The modelled world identifies the total volume in which the geometry is confined. The modelled world is everything outside of the cells denoted by the hash symbol (#) and consists of air at atmospheric pressure.

4.8.2 Surface card

The second section of the MCNP5 input file contains all the surface information and is separated from the cell card by a blank line called a blank line delimiter.

The geometry of the calibrator is simplified by its cylindrical design. This has allowed the use of in-built macro body functions in the input file. The macro body used for the construction is a right circular cylinder (RCC). A RCC is defined by the following parameters:

RCC v_x v_y v_z h_x h_y h_z R

where v_x, v_y and v_z are the x, y and z Cartesian coordinates of the base of the cylinder, h_x, h_y and h_z represent the height of the cylinder in the x, y and z directions

and R is the radius of the cylinder. It can be seen from the surface cards that the outer tube of the chamber can be defined as the space between the internal surface of cylinder 4 and the external surface of cylinder 3.

```
c Surface Cards
    2         so 25                                  $Universe
    3        rcc 0 0 -17.1 0 0 36 9.5                $outer tube
    4        rcc 0 0 -17.1 0 0 36 9.25               $outer tube
    5        rcc 0 0 18.4 0 0 0.5 9.25               $top plate
    6        rcc 0 0 18.9 0 0 1.4 9.5                $top plate
    7        rcc 0 0 -18.9 0 0 37.8 3.75             $Inner Tube
    8        rcc 0 0 -18.9 0 0 37.8 3.65             $Inner tube
    9        rcc 0 0 -14 0 0 30 6.5                  $electrode
   10        rcc 0 0 -14 0 0 30 6.4                  $electrode
   11        rcc 0 0 -17.1 0 0 0.5 9.25              $base plate
   12        rcc 0 0 -19 0 0 1.9 9.5                 $base plate
   13        rcc 0 0 20.3 0 0 0.6 5.5                $jig
   14        rcc 0 0 20.3 0 0 0.6 2.8                $jig
   15        rcc 0 0 20.3 0 0 -19.5 3                $jig
   16        rcc 0 0 20.3 0 0 -19.5 2.8              $jig
   17        rcc 0 0 20.3 0 0 -1.4 2.8               $jig
   18        rcc 0 0 0.8 0 0 -0.2 1.2                $jig
   19        rcc 0 0 0.8 0 0 -0.2 3                  $jig
   20        rcc 0 0 0.6 0 0 -1 1.2                  $jig
   21        rcc 0 0 0.6 0 0 -1.2 1.4                $jig
   22        rcc 0 0 -0.4 0 0 4.565 1.0875           $P6 vial
   23        rcc 0 0 -0.28 0 0 4.39 0.9675           $P6 vial
   24        rcc 0 0 4.14 0 0 0.475 0.75625          $P6 vial
   26        rcc 0 0 4.61 0 0 0.36 0.995             $P6 vial
   27        rcc 0 0 4.785 0 0 0.2 0.6               $P6 vial
   28        rcc 0 0 4.105 0 0 0.97 0.63625          $P6 vial
   29        rcc 0 0 -0.28 0 0 1.36 0.9675           $radionuclide solution
   30        rcc 0 0 18.9 0 0 1.9 3.65               $jig
   31        rcc 2.9 0 3.8 0 0 10 2.9                $jig
```

The universe within which the model resides is a sphere of radius 25 cm. the specification of the sphere is:

SO R

where SO denotes a sphere centred at the origin and R is the radius of the sphere. Any particle reaching this surface of the sphere will be terminated at this point. The

radius is kept reasonably tight to the Fidelis model to negate particle histories that will not contribute to the tallies.

The MCNP5 model of the P6 vial is designed to replicate that of a P6 vial as closely as possible within the constraints of the MCNP5 geometry capabilities. The P6 vial consists of a number of curved surfaces that are impractical to model in MCNP5. The vial is therefore constructed of three separate cylinders to represent the body, neck and the top of the vial.

4.8.3 Mode card

The final section of the MCNP5 input file contains the information to allow the MCNP5 programme to interpret the file. The mode card specifies the type of transport to be considered in the simulation. The mode card is specified as follows:

```
mode  p
```

In this specification, the MCNP5 programme is instructed to undertake some simplification of the physics modelling by considering photon transport only. The simplification requires that all ionising events from photon interactions are transmitted in the same direction as the photon and that electron energy deposition is immediate (X-5 Monte Carlo Team, 2003).

4.8.4 Material card

The material card specifies the composition of each material.

```
m1    7000.          -0.78  $Air
      8000.          -0.22
m2    13000.        -0.967  $top plate and bottom
      14000.        -0.004 26000.         -0.005 29000.         -0.0015
      25000.        -0.001 12000.         -0.017 24000.         -0.0015
      30000.       -0.0015 22000.        -0.0015
m3    13000.       -0.9715  $outer tube
      14000.        -0.007 26000.         -0.005 29000.          -0.001
      25000.        -0.004 12000.         -0.006 24000.         -0.0025
      30000.        -0.002 22000.         -0.001
m4    13000.       -0.9765  $inner tube
      14000.        -0.002 26000.         -0.005 29000.          -0.001
      25000.        -0.004 12000.         -0.006 24000.         -0.0025
      30000.        -0.002 22000.         -0.001
m5    1000.         -0.081  $jig
      6000.         -0.599 8000.           -0.32
m7    1000.         -0.112  $radionuclide solution
      8000.         -0.888
m8    7000.              1  $nitrogen gas
m9    8000.          -0.46  $P6 vial
      11000.          -0.1 14000.          -0.34 20000.            -0.1
m10   13000.         -0.995  $electrode
      29000.       -0.0005 14000.        -0.0015 26000.         -0.0015
      25000.       -0.0005 30000.         -0.001
```

Each material is firstly defined by a number, in this instance m1 through to m10. These numbers are used in the second column of the cell cards to define the material for that particular cell. The next number indicates the atomic component in the format:

ZZZAAA.nnX

where ZZZ is the atomic number, AAA is the mass number, nn is the cross sectional identifier (default cross sectional library used if left blank) and X is the class of data (again, default used if left blank). Only the pure element form is considered in this

model and therefore the mass numbers are not adjusted. All other defaults are accepted.

Next to the atomic definition is the fraction. The fraction can either be expressed as a nuclide fraction or, with a negative sign prefix, as a weight fraction. For example, material 7 is defined as water based solution. This could be expressed as

```
m7          1000        -0.112
            8000        -0.888
```

or

```
m7          1000        0.667
            8000        0.333
```

Both of these are acceptable nomenclatures.

4.8.5 Importance card

The first line beginning with imp:p details the importance of each of the cells.

```
imp:p              1 9r                    0  $ 2, 12
```

The importance function is a key element of the MCNP5 code in undertaking variance reduction and allowing statistically significant results for a smaller number of simulated particles. As the active region (nitrogen gas) fully surrounds the sample, variance reduction is less of an issue in gaining a statistically relevant result in this

geometry. In this example, all the cells have the sample importance value except the outside world, where a particle reaching this point will be terminated.

4.8.6 Source definition card

The source definition card defines the particulars of the source.

```
sdef erg=d2 rad=d1 cell=10 par=2
si1 0 2
sp1 -21 2
si2 l 0.02720 0.02747 0.03094 &          $Photon Energies
0.03100 0.03171 0.1590 0.2480 &
0.2810 0.3463 0.4400 0.5053 &
0.52900 0.53850 0.62460 0.68790 &
0.73580 0.78360
sp2 0.24600 0.45800 0.04460 &          $Photon Probabilities
0.08660 0.02660 0.82800 &
0.00071 0.00079 0.00125 &
0.00425 0.00314 0.01380 &
0.00379 0.00083 0.00027 &
0.00061 0.00059
```

In the above example an ^{123}I source is simulated. The particle type is defined as par=2 which simulates photons. The energies and emission probabilities of the source are specified erg=d2 with reference to si2 and sp2. All energies are in MeV. The cell=10 card identified that the photons are to emanate from cell 10, the radionuclide solution in the P6 vial. When using the cell card to identify a cell for emissions of the photons, the extent of the photons and sampling emission distributions also have to be specified using the rad card. The rad=d1 identifies the distributions as per the si1 and sp1 cards. The distributions are set to be spherical with a radius of 2 cm and a uniform sampling within this region. Providing this distribution lies within cell 10, the photons will be simulated at a uniformly random location within the cell volume.

4.8.7 Tally card

The tally card within the input file instructs the MCNP5 programme what information to return from the simulation. All simulations must include a tally card or a critical failure will be returned.

```
f6:p 11
sd6 1
```

The tally selected for this initial simulation is the f6 tally. The f6 tally provides a track length estimate of energy deposited in MeV normalised per starting particle. Cell 11, the nitrogen gas, is defined as the volume over which the tally is acquired. The ionisation current (*I*) generated in a radionuclide calibrator can be expressed as:

$$I = \frac{\mathrm{NeE_d}}{\mathrm{W}} \quad \text{...Equation 4.1}$$

where N is the number of photons emitted per second (assumed monoenergetic), e is the electron charge, W is the energy required to create an ion pair in the gas and E_d is the energy deposited in the gas per photon of emission (Gostely and Laedermann, 2000). The value of W is dependent on the gas used in the chamber but is typically between 20 and 45 eV (Prekeges, 2011, p.3). For a given sample activity, the ionisation current is dependent on the energy deposited in the gas and therefore the f6 tally is a suitable surrogate for ionisation current.

Each tally result also has an estimated relative error, defined as one standard deviation of the mean, divided by the mean. (X-5 Monte Carlo Team, 2003, p.1-6). The significance of the range of errors is given in Table 4.5.

Range of estimated relative error	Quality of the tally
0.5 to 1.0	Not meaningful
0.2 to 0.5	Factor of a few
0.1 to 0.2	Questionable
<0.10	Generally reliable
<0.05	Generally reliable for point detectors

Table 4.5: Estimated relative errors and the suggested corresponding quality of the tally (X-5 Monte Carlo Team, 2003, p.1-7)

An estimated relative error of 0.10 equates to an uncertainty in the tally of ±10% at one standard deviation of the mean (following the central limit theorem). At three standard deviations, the uncertainty is ±30%. Relative errors in excess of 0.10 can therefore cast doubt on the reliability of the tally result. For the remaining MCNP5 simulations undertaken, a more stringent ±5% maximum uncertainty was employed to improve the tally precision. However, the relative error gives no indication of the accuracy of the result. which can be estimated by comparative measurements with the physical system (X-5 Monte Carlo Team, 2003, p.1-6).

4.8.8 Particle and print card

The final three lines in the MCNP5 input file specify the number of particles to be simulated and the printing requirements of the returned tallies.

```
nps 1E6
prdmp -5 -5 1
print
```

In this instance, the number of particles simulated is 1×10^{6}. As discussed in Chapter 2, the estimated relative error depends on the number of particle histories. The number of histories required to meet the minimum ±5% uncertainty constraint specified in 4.8.7 was determined by increasing the number of histories until the constraint was achieved. (Any instances where the constraint was not met are noted where applicable). The prdmp and print functions prompt the MCNP5 programme to return the tally results periodically and also as a final print out.

4.8.9 Geometry visualisation

Distributed with MCNP5 is a visualisation tool called "vised" (version MCNP5-Nov-2005-19L). The visual editor is useful in confirming that the geometries are accurate and as described in the input file.

The first visualisation shown in Figure 4.3 is the outer tube, base and top of the calibrator. The chamber has been rotated to provide a 3D visualisation of the chamber for more detail.

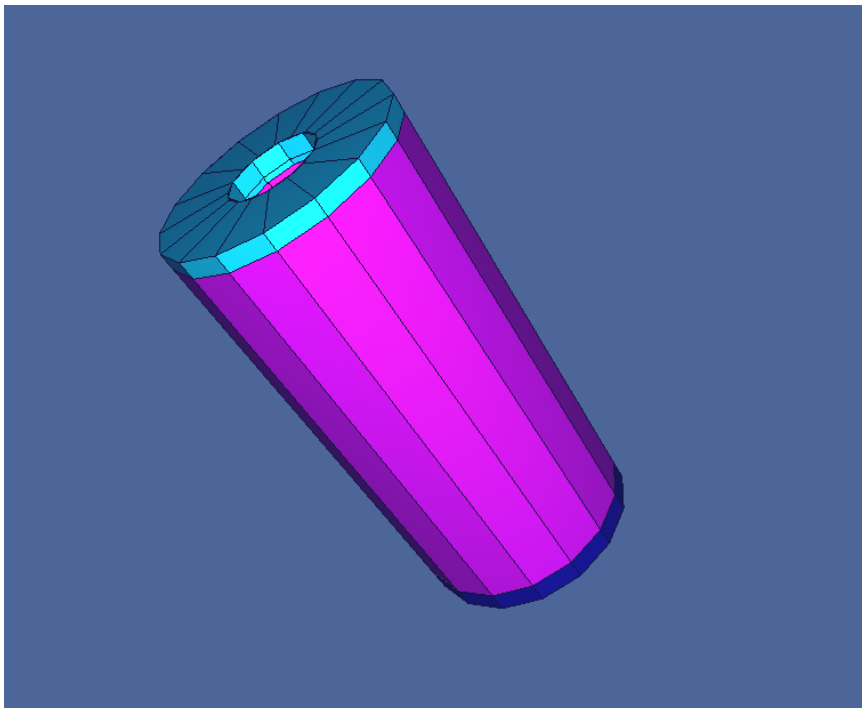

Figure 4.3: Base, top and outer tube of the Fidelis chamber

The next visualisation (Figure 4.4) shows the inner tube and the surrounding electrode. The nitrogen gas is composed of the volume between inner and outer tube excluding the electrode.

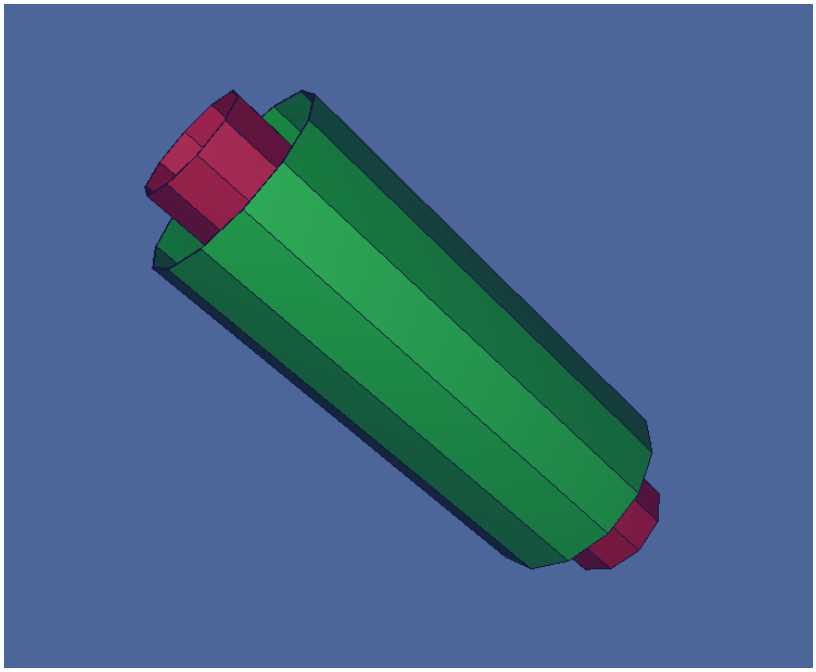

Figure 4.4: Inner tube and electrode

The P6 vial jig and the vial can be seen in Figure 4.5. An opening in the jig allows for the placement of the P6 vial.

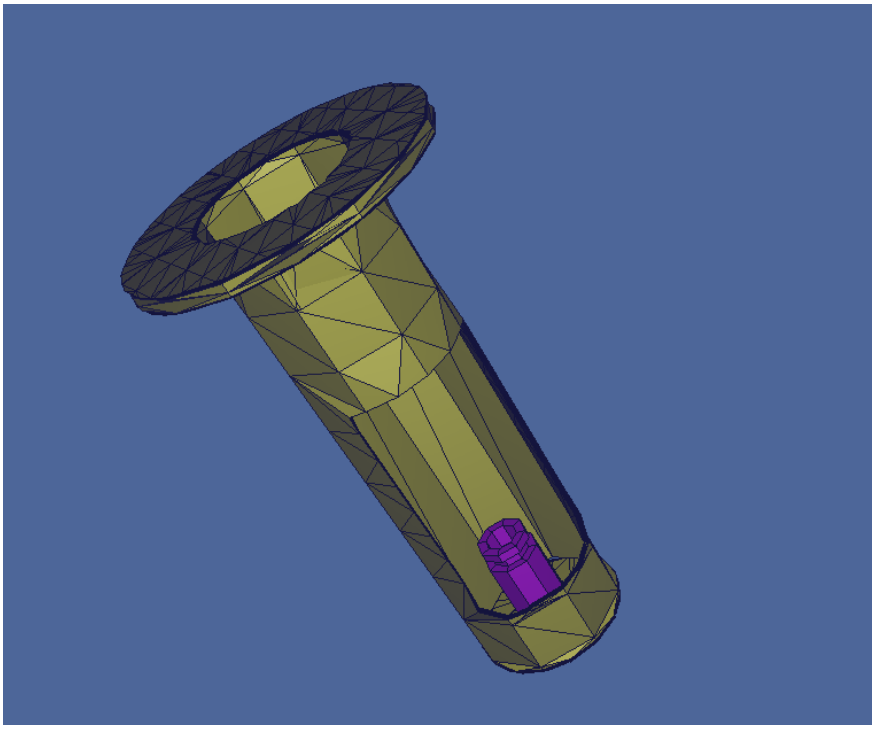

Figure 4.5: Visual depiction of the jig and the vial

2D representations of the geometry are shown in Figures 4.6 and 4.7. The first figure shows a cross section through the middle of the calibrator. The vial can be seen resting in the jig and located in the centre of the chamber. The second figure is an aerial cross section that shows the geometry as a series of right centred cylinders.

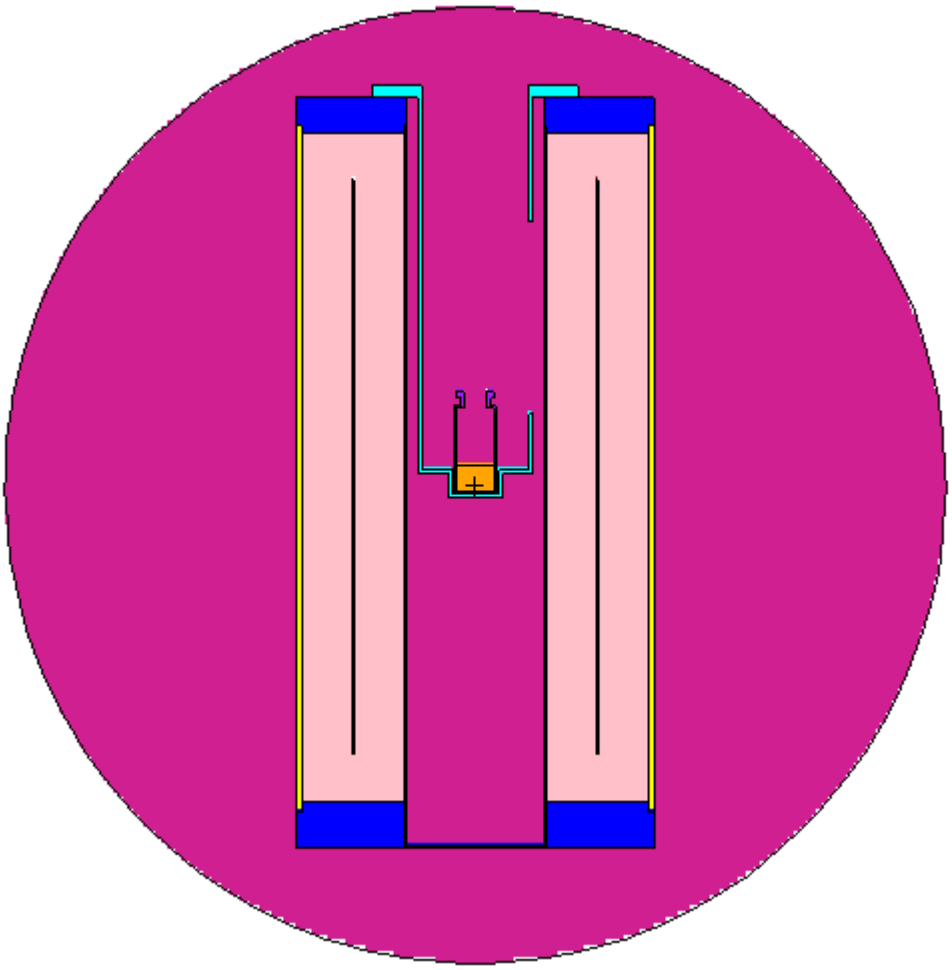

Figure 4.6: Cross-sectional depiction through the sagittal aspect of the Fidelis

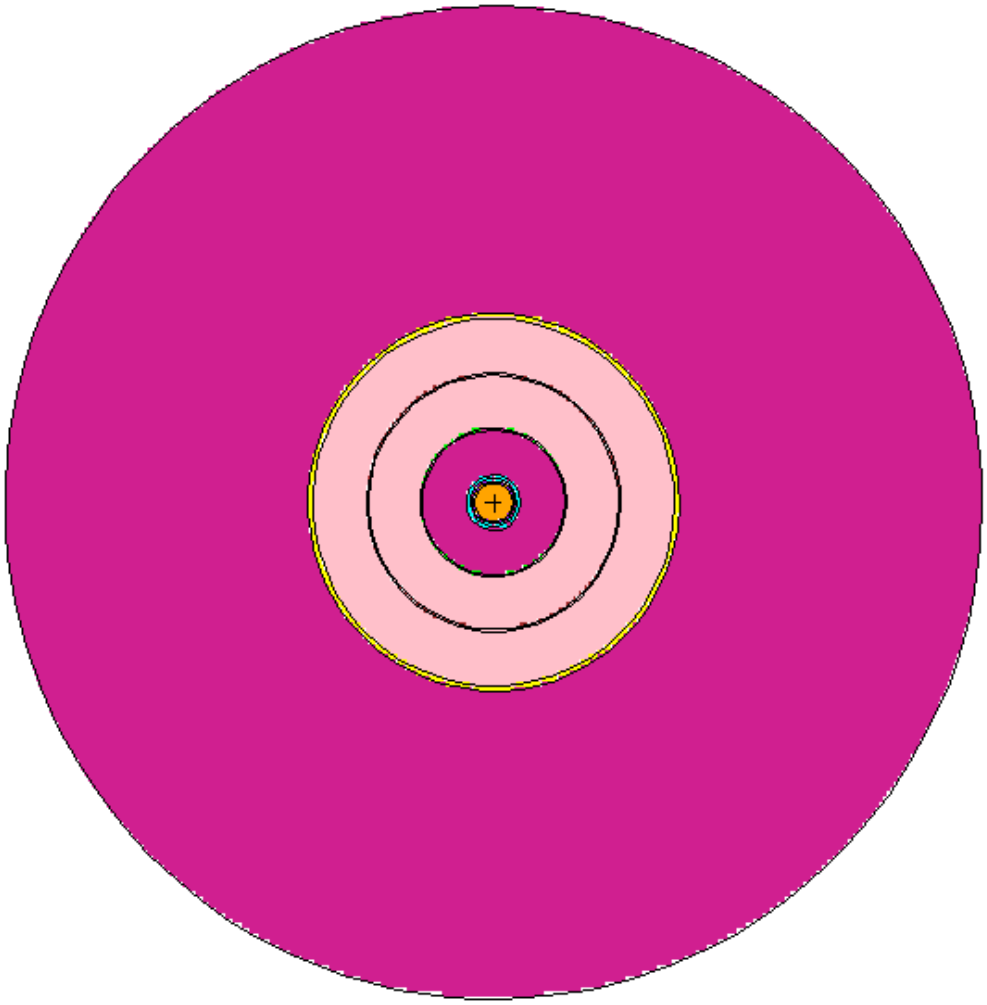

Figure 4.7: Cross-sectional depiction through the transverse aspect of the Fidelis

4.9 Validation of the Monte Carlo model

An integral part of a calibrator response is the sensitivity of the calibrator to photons of varying incident energy. The sensitivity of the calibrator depends on a number of aspects including the calibrator design and material composition. Prior to modelling, the response of a calibrator would be assessed experimentally, using standard sources. In a similar method to the determination of calibration factors, with the additional knowledge of the abundance and emissions of the radionuclide, a sensitivity curve can be experimentally determined. Once the sensitivity curve for the calibrator has been characterised, it is possible to derive calibration factors for radionuclides providing the emission and energy characteristics are known.

The advantage of applying a Monte Carlo approach is that monoenergetic photons can be simulated and therefore issues regarding the accurate characterisation of radionuclides used for the sensitivity curve determination are negated. However, these issues are still present when considering the derivation of calibration factors.

The initial MCNP5 model of the Fidelis was concerned with the generation of a sensitivity curve to elucidate potential issues with the assay of ^{123}I.

4.9.1 Monte Carlo Fidelis sensitivity curve

To produce the sensitivity curve for the Monte Carlo Fidelis model, monoenergetic photons ranging from 10 keV up to 700 keV were simulated from an aqueous radionuclide solution within the P6 vial. Each simulation was run for 1×10^6 photons and the average energy deposited in the nitrogen gas per starting particle was recorded. The statistical precision of each tally was inspected to ensure that the estimated relative error was less than 0.05.

The results of the simulation are shown in Table 4.6.

Figure 4.8 shows the MCNP5 modelled sensitivity curve for the full energy range simulated as per Table 4.6.

The region of particular interest for ^{123}I within the sensitivity curve concerns 20 to 200 keV. For clarity, this region is reproduced in Figure 4.9.

Photon Energy keV	Energy deposited MeV	Energy deposited keV	Energy deposited eV
2.5	0.00	0.00	0.00
5.0	0.00	0.00	0.00
7.5	0.00	0.00	0.00
10.0	0.00	0.00	0.00
12.5[a]	1.10×10^{-8}	0.00	0.01
15.0[a]	5.30×10^{-7}	0.00	0.53
17.5	4.75×10^{-6}	0.00	4.75
20.0	1.67×10^{-5}	0.02	16.72
22.5	3.50×10^{-5}	0.04	35.03
25.0	5.48×10^{-5}	0.05	54.84
27.5	7.19×10^{-5}	0.07	71.93
30.0	8.51×10^{-5}	0.09	85.06
32.5	9.43×10^{-5}	0.09	94.30
35.0	1.00×10^{-4}	0.10	100.23
40.0	1.06×10^{-4}	0.11	105.71
50.0	1.09×10^{-4}	0.11	108.81
60.0	1.14×10^{-4}	0.11	114.22
70.0	1.24×10^{-4}	0.12	124.34
80.0	1.38×10^{-4}	0.14	138.35
90.0	1.55×10^{-4}	0.15	154.97
100.0	1.74×10^{-4}	0.17	173.63
110.0	1.96×10^{-4}	0.20	196.40
125.0	2.26×10^{-4}	0.23	225.54
150.0	2.81×10^{-4}	0.28	281.19
175.0	3.39×10^{-4}	0.34	338.96
200.0	3.98×10^{-4}	0.40	397.68
250.0	5.15×10^{-4}	0.52	515.15
300.0	6.31×10^{-4}	0.63	631.15
350.0	7.45×10^{-4}	0.75	745.45
400.0	8.58×10^{-4}	0.86	857.77
450.0	9.67×10^{-4}	0.97	966.68
500.0	1.07×10^{-3}	1.07	1074.21
550.0	1.18×10^{-3}	1.18	1178.07
600.0	1.28×10^{-3}	1.28	1280.19
650.0	1.38×10^{-3}	1.38	1380.13
700.0	1.48×10^{-3}	1.48	1476.98

[a] relative error exceeded 0.05

Table 4.6: Energy deposited per starting particle in the nitrogen gas

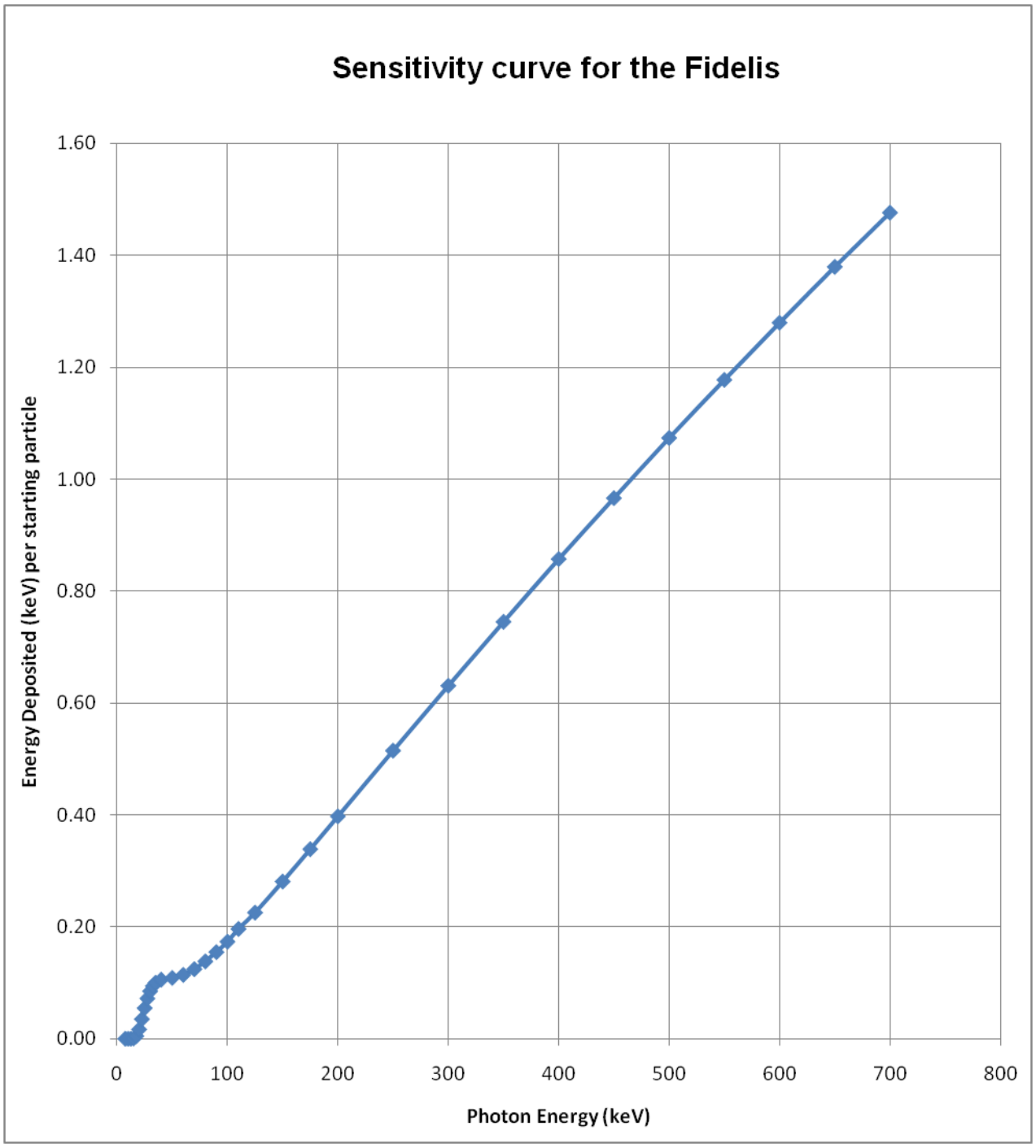

Figure 4.8: Monte Carlo sensitivity curve for the Fidelis model

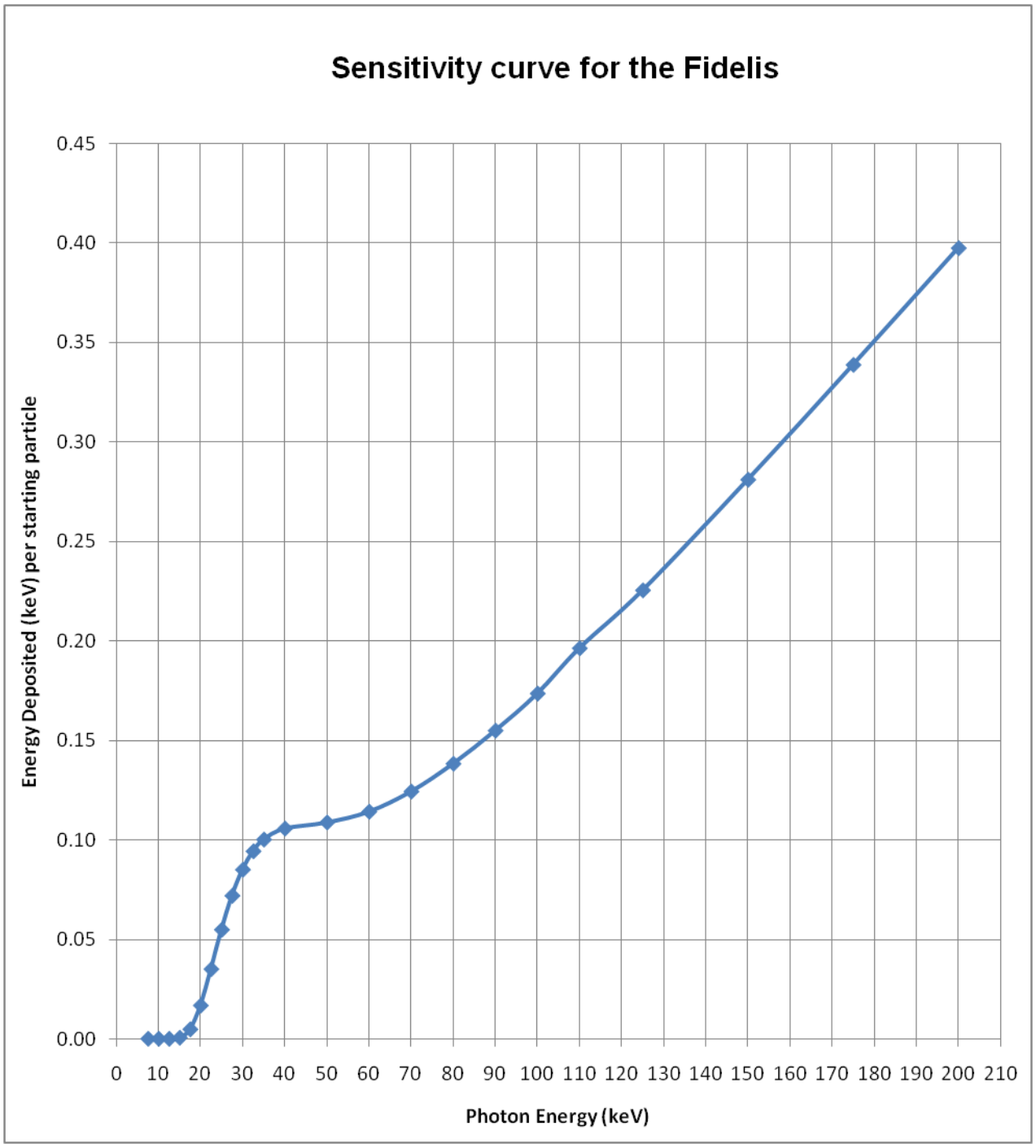

Figure 4.9: Monte Carlo sensitivity curve for the Fidelis model in the region 7.5 – 200 keV

4.9.2 Discussion of Monte Carlo Sensitivity curve

In this particular configuration, the threshold simulation photon energy for energy deposition in the nitrogen gas is 12.5 keV. In two instances the relative error (noted by a subscript [a]) exceeded 0.05. These related to the two low energy photon simulations at 12.5 keV and 15.0 keV. With particular reference to the emissions of ^{123}I, the low energy x-ray emissions around 27 to 31 keV are located on an increasing gradient in the sensitivity curve. The sensitivity of the 159 keV gamma radiation in this configuration is approximately 4 times higher than that of the x-rays. The sensitivity curve therefore implies that the predominant contribution to the ionisation current for ^{123}I in the modelled configuration will be the principal gamma radiation.

4.9.3 Validation of the sensitivity curve

Validation of the measurements undertaken on the Fidelis is the ideal situation to allow for a comparison with the Monte Carlo model. Potentially, practical measurements could be made to validate the model for a known number of radionuclide solutions. However, this can be difficult because of the unknown activity impurities. Alternatively, using a Monte Carlo model, a number of radionuclides in a P6 vial can be simulated and compared with the Fidelis factors generated by NPL. The radionuclides used for assessment were: ^{109}Cd, ^{241}Am, ^{51}Cr, ^{7}Be, ^{57}Co, ^{99m}Tc, ^{67}Ga, ^{139}Ce, ^{123}I, ^{113m}In, ^{203}Pb, ^{75}Se, ^{131}I, ^{111}In, ^{137}Cs, ^{54}Mn and ^{60}Co. These radionuclides were chosen for the validation due to their predominant photon only emissions and the fact that the emissions have been characterised in the literature.

Table 4.7 details the principal emissions and emission probabilities of these radionuclides.

Radionuclide	Principal x-ray or gamma emissions (keV)	Emission probability (%)
^{109}Cd	88.03 22.16 21.99 24.94 25.46 24.91 29.84 31.86	3.61 54.7 29.0 9.85 2.76 5.05 4.63 3.64
^{241}Am	26.34 33.19 59.54 13.93 17.51 20.98 15.88 11.89	2.4 0.119 35.7 22.4 30.5 7.31 0.505 1.23
^{51}Cr	320.1 4.952 4.945 5.427 5.427	9.83 13.3 6.7 1.76 0.888
^{7}Be	477.6	10.3
^{57}Co	14.41 122.1 136.5 692.0 6.404 6.391 7.058 7.058	9.19 85.6 10.6 0.16 33.4 16.9 4.51 2.29
^{99m}Tc	140.5 18.37 18.25 20.62	88.9 4.03 2.12 0.688
^{67}Ga	91.27 93.31 184.6 209.0 300.2 393.5 494.2 794.4 887.7 8.639 8.616	3.07 38.3 20.9 2.37 16.8 4.7 0.068 0.0513 0.145 32.8 16.7

	9.572 9.572	4.49 2.30
^{139}Ce	165.9 34.42 33.03 37.8 38.75 37.72 4.649 5.123	79.1 42.4 23.1 8.27 3.10 4.28 4.93 5.20
^{123}I	27.20 27.47 30.94 31.00 31.71 159.00 248.00 281.0 346.3 440.0 505.3 529.0 538.50 624.60 687.90 735.80 783.60	24.6 45.8 44.6 8.66 2.66 82.80 0.071 0.079 0.125 0.425 0.314 1.380 0.379 0.083 0.027 0.061 0.059
^{113m}In	391.7 24.21 24 27.28 27.24	64.2 13.1 6.99 2.40 1.24
^{203}Pb	279.2 401.3 680.5 72.87 70.83 82.57 84.97 82.11 10.26 12.23 14.41	80.1 3.44 0.697 43.1 25.5 9.84 4.27 5.12 15.8 15.3 2.83
^{75}Se	66.05 96.73 121.1 136.0 198.6 264.7 279.5 303.9 400.6 10.54 10.51	1.1 3.5 17.7 60.6 1.5 59.4 25.2 1.31 11.3 31.8 16.3

	11.73	4.68
^{131}I	80.18 17.72 284.3 325.8 364.5 503.0 637.0 624.7 722.9 29.78 29.46	2.62 0.265 6.06 0.251 81.2 0.361 7.27 0.22 1.80 2.59 1.40
^{111}In	171.3 245.5 23.17 22.98 26.09 26.64 26.06	90.5 94.0 44.3 23.6 8.07 2.35 4.14
^{137}Cs	661.66	84.99
^{54}Mn	834.8	100
^{60}Co	1173 1332	99.9 100

Table 4.7: Principal photon energies and emission probabilities for the radionuclides used to validate the Monte Carlo model

The radionuclides detailed in Table 4.7 were simulated as solutions within the P6 vials and the energy deposited in the nitrogen gas tallied. Each simulation was run for 1×10^6 photons and the average energy deposited in the nitrogen gas per starting particle was recorded. The statistical precision of each tally was inspected to ensure that the estimated relative error was less than 0.05.

Table 4.8 details the results of the simulations. Columns 1, 2 and 3 detail the radionuclide used in the simulation, the published NPL calibration factor (P6 vial) and the published uncertainty in the calibration factor. The 4th column details the

fractional calibration factor as published by NPL for a P6 vial relative to ^{60}Co. The energy deposited is then stated per MeV and keV respectively per starting photon for the Monte Carlo model. The energy deposited in the nitrogen gas must be normalised to the total emission probability per radioactive decay. For example, the principal photon for ^{51}Cr has a 9.83% emission probability. As Monte Carlo code samples sequential photons, the total recorded energy deposition is approximately 10 times higher than what would be seen for a sample of ^{51}Cr in the Fidelis. Similarly, ^{60}Co has an emission probability of 199.9% for both of the principal photons, the energy deposited in the model is therefore approximately half of what would occur with a radioactive sample.

The fractional calibration factors for the Monte Carlo model and the published NPL values are graphically represented in Figure 4.10.

4.9.4 Discussion of the sensitivity curve validation

The Monte Carlo model shows good concordance with the physical calibration factors derived by NPL over the energy ranges from 20 – 1200 keV. As there is a close relationship with the fractional calibration factors, estimations of the calibration factors based on the Monte Carlo simulations are possible. Two methods may be utilised to undertake a derivation of a new calibration factor. Firstly, for the configuration simulated, the sensitivity curves in Figures 4.8 and 4.9 may be used to calculate a calibration factor relative to ^{60}Co. Secondly, Monte Carlo simulations may be undertaken for this model and new calibration factors derived based on the fractional energy deposition in the nitrogen gas.

Radionuclide	Fidelis Calibration Factor (pA/MBq)	Fidelis Uncertainty in factor (%)	Fractional Fidelis calibration factor	MCNP5 Fidelis energy deposited (MeV)	MCNP5 Fidelis energy deposited (keV)	Total emissions per starting particle	MCNP5 normalised to emissions per starting particle	Fractional MCNP5 calibration factor
^{109}Cd	0.1176	0.67	0.005	3.70E-05	0.04	1.132	0.042	0.009
^{241}Am	0.228	0.38	0.010	4.55E-05	0.05	1.002	0.046	0.009
^{51}Cr	0.3327	0.67	0.015	2.05E-04	0.20	0.325	0.067	0.014
^{7}Be	0.5182	1.17	0.023	1.03E-03	1.03	0.103	0.106	0.022
^{57}Co	1.174	0.67	0.053	1.33E-04	0.13	1.627	0.217	0.045
^{99m}Tc	1.227	0.84	0.055	2.42E-04	0.24	0.957	0.232	0.048
^{67}Ga	1.547	1.34	0.070	2.12E-04	0.21	1.427	0.303	0.063
^{139}Ce	1.652	0.84	0.075	1.95E-04	0.19	1.704	0.332	0.069
^{123}I	1.685	0.84	0.076	2.02E-04	0.20	1.720	0.348	0.072
^{113m}In	2.72	0.67	0.123	6.27E-04	0.63	0.879	0.551	0.114
^{203}Pb	3.134	0.67	0.141	3.34E-04	0.33	2.060	0.689	0.143
^{75}Se	3.923	1.67	0.177	3.34E-04	0.33	2.344	0.782	0.162
^{131}I	3.999	0.34	0.180	7.89E-04	0.79	1.040	0.821	0.170
^{111}In	4.088	0.67	0.184	3.03E-04	0.30	2.670	0.810	0.168
^{137}Cs	5.751	0.67	0.259	1.40E-03	1.40	0.850	1.192	0.247
^{54}Mn	8.148	0.34	0.368	1.73E-03	1.73	1.000	1.728	0.358
^{60}Co	22.17	0.38	1.000	2.41E-03	2.41	1.999	4.824	1.000

Table 4.8: Results of the validation of the Monte Carlo Fidelis compared to the published NPL calibration factors

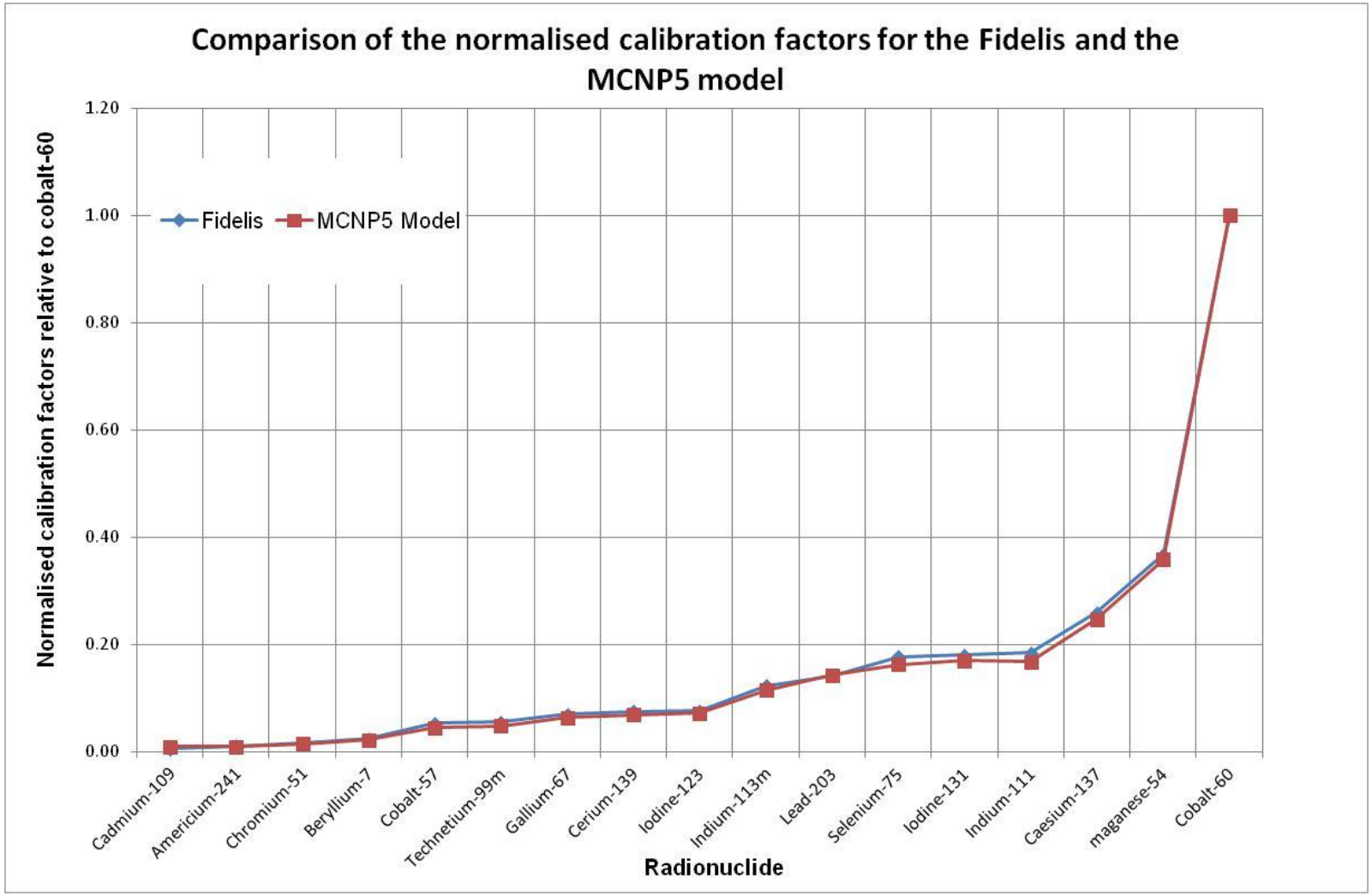

Figure 4.10: Graphical representation of the normalised calibration factors for the Fidelis compared to the Monte Carlo model

CHAPTER 5: MONTE CARLO SIMULATION OF FACTORS INFLUENCING THE PERFORMANCE OF A FIDELIS CALIBRATOR

5.1 Introduction

In the previous chapter a Monte Carlo model of a Fidelis radionuclide calibrator was produced and validated against NPL published calibration factors.

As previously stated, syringe factors for the Fidelis calibrator do not appear in the published list of NPL approved calibration factors (NPL, 2015c). The knowledge of accurate syringe factors is important for all radionuclide calibrators and in particular the Fidelis secondary standard calibrator, where cross-calibrations of these factors may be undertaken against a field calibrator.

In this chapter, a syringe calibration factor is derived for a commonly used syringe for intra venous administrations within the Medical Physics Department of the University Hospital of Wales, namely a 1 ml BD Plastipak™ syringe.

Typically, most radionuclide calibrators use a jig to hold the syringe in a reproducible position. However, in this instance, there is no syringe jig supplied with the Fidelis. Substitute jigs are not considered here as the difference in calibration factor is assessed for the syringe composition as opposed to any jig composition that may provide absorption and scatter media.

5.2 Monte Carlo syringe model

The Monte Carlo model of a 1 ml BD Plastipak™ syringe is shown in Figure 5.1. Similar to the Monte Carlo design of the P6 vial, the syringe consists of a number of cylindrical surfaces which, when combined together, form the tip of the syringe, the main outer shaft and the rubber tipped plunger. The syringe is predominately constructed of plastic with a wall thickness of 0.1 cm and a density of 1.19 g cm^{-3}. The rubber tip at the end of the plunger has a density of 0.92 g cm^{-3}.

As per local protocol in the Medical Physics Department, assays of radioactivity in a syringe are undertaken with a blind hub. The blind hub is placed on the tip of the syringe to help ensure the contents remain sterile during the assay and transport of the radiopharmaceutical and also to prevent loss of liquid from the syringe.

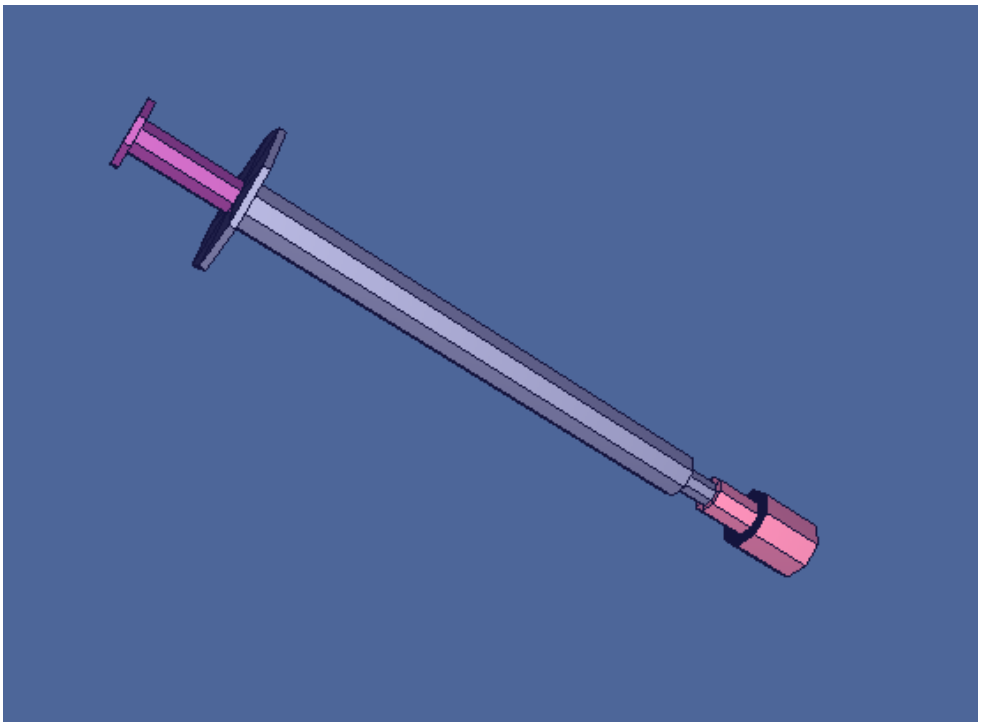

Figure 5.1: Monte Carlo model of a 1 ml BD Plastipak™ syringe

The syringe location within the well of the chamber can be seen in Figure 5.2.

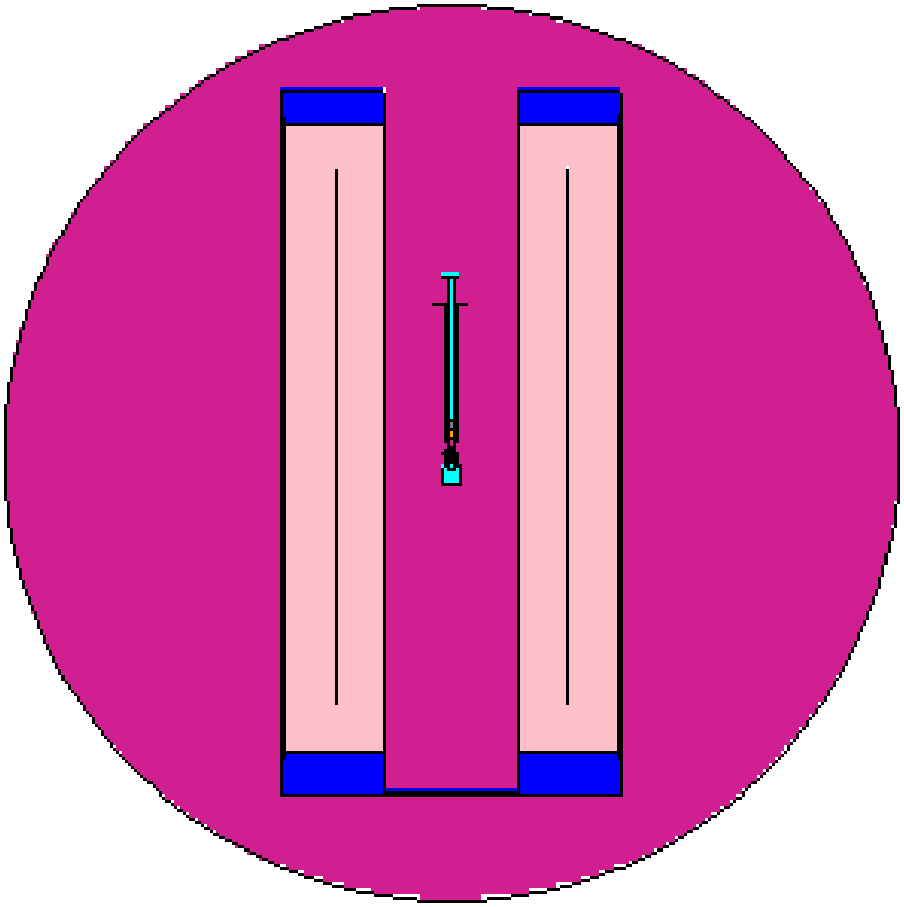

Figure 5.2: location of the syringe within the Fidelis model

5.3 Characterisation of volume effect for ^{123}I in a 1 ml syringe

The position of the syringe in the chamber is simulated to be similar to that of the P6 vial described in chapter 4. However, the volume of the syringe is considerably lower than the 4 ml simulated in the P6 vial. Variations in syringe volume are known to have an effect on the amount of ionisation current produced (Gadd et al., 2006). Typically, volumes between 0.1 and 0.5 ml are dispensed by the radiopharmacy in the Medical Physics Department. It is therefore prudent to determine the variation in energy deposited in the chamber between these volumes.

A syringe of construction detailed in section 5.2 was modelled in the Fidelis chamber with a series of simulations. Initially, the syringe contained a 0.1 ml solution of ^{123}I and following each simulation, the volume solution was incremented to 0.5 ml in 0.1 ml steps. Each simulation was run for 1×10^6 photons and the average energy deposited in the nitrogen gas per starting particle was recorded. The statistical precision of each tally was inspected to ensure that the estimated relative error was less than 0.05.

5.3.1 Volume effect results

The energy deposited in the nitrogen gas for each syringe volume is shown in Table 5.1.

Syringe volume (ml)	Energy deposited (MeV)	Energy deposited (eV)	Ratio to 0.1 ml
0.1	2.44×10^{-4}	243.87	1.000
0.2	2.43×10^{-4}	243.10	0.997
0.3	2.43×10^{-4}	242.78	0.996
0.4	2.43×10^{-4}	242.58	0.995
0.5	2.42×10^{-4}	242.39	0.994

Table 5.1: variation in energy deposition per syringe radionuclide solution volume of ^{123}I

The variation in energy deposited per syringe volume can be seen in Figure 5.3.

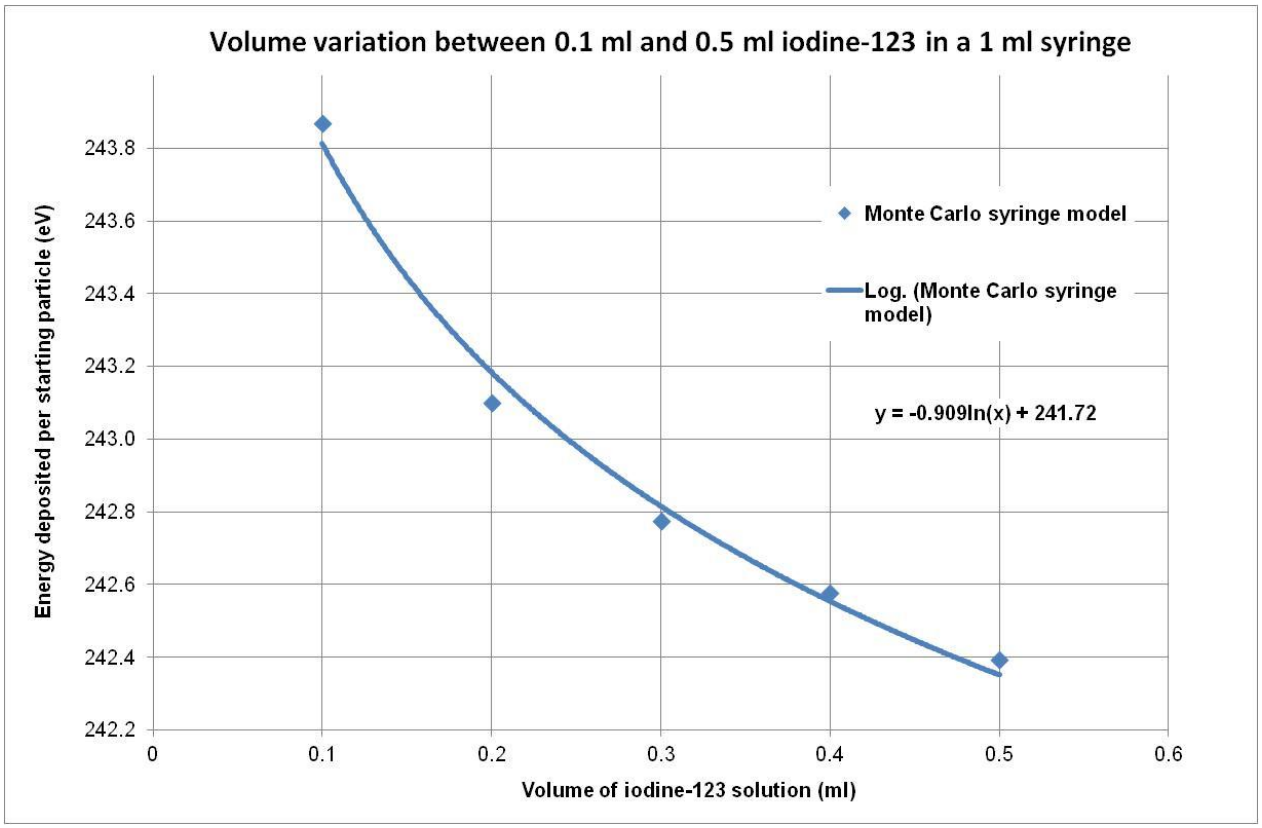

Figure 5.3: Syringe volume variation for 1 ml BD Plastipak™ syringe

5.3.2 Discussion of volume effect for ^{123}I in a 1 ml syringe

As can be seen from Table 5.1, there is less than 1% variation in the energy deposited per starting particle in the nitrogen gas between 0.1 ml and 0.5 ml. A least squares fit model was used in Excel™ to characterise the relationship between the energy deposited and the syringe volume and is given by:

Energy deposited per starting particle (eV) = -0.909ln(volume (ml)) + 241.72 ....

Equation 5.1

This logarithmic relationship allows for a calibration factor derived for this syringe at a given volume to be transferred to the same syringe at a different volume.

5.3.3 Derivation of syringe calibration factors

The variation in energy deposited by the 1 ml BD Plastipak™ syringe for different volumes can be compared with the P6 vial as shown in Table 5.2. The calibration factor for the P6 vial was validated in chapter 4 for the Monte Carlo model for ^{123}I. Instead of being considered in terms of pA/MBq, for modelling purposes the calibration factor can be considered in terms of energy deposited per starting particle. As the energy deposited is normalised per starting particle, the energy deposited in the syringe simulations can be compared to the P6 vial. The ratio of the energy deposited in the nitrogen gas for the syringe and vial can be used to determine the percentage difference and to derive a new calibration factor for the syringe.

Container	Volume (ml)	Energy deposited (MeV)	Fidelis published calibration factor (pA/MBq)	Fidelis derived calibration factor (pA/MBq)	% difference to vial
P6 vial	4.0	2.02×10^{-04}	1.685	1.685	0.0
BD Plastipak™ 1ml syringe	0.1	2.44×10^{-04}	-	2.034	20.7
BD Plastipak™ 1ml syringe	0.2	2.43×10^{-04}	-	2.0027	20.3
BD Plastipak™ 1ml syringe	0.3	2.43×10^{-04}	-	2.024	20.1
BD Plastipak™ 1ml syringe	0.4	2.43×10^{-04}	-	2.023	20.0
BD Plastipak™ 1ml syringe	0.5	2.42×10^{-04}	-	2.021	20.0

Table 5.2: Percentage difference between the vial and the syringe simulations with derived syringe calibration factors

5.3.4 Discussion of syringe calibration factors

For this particular example of a 1 ml BD Plastipak™ syringe, we can see from Table 5.2 that there is up to 21% increase in the energy deposited in the nitrogen gas when the ^{123}I is in a syringe as compared to a P6 vial. These figures are in keeping with those reported by Tyler and Woods (2003). The authors reported that the range of syringe factors for a number of syringes containing ^{123}I was between 1.71 – 1.90 pA/MBq. The maximum calculated calibration factor of 2.034 pA/MBq is somewhat above the authors quoted range, but the paper does not specify the particulars of the syringes that they used for assay. However, it must be borne in mind that these calibration figures do not appear in the published NPL calibration factors document (NPL, 2015c).

Although the variation in calibration factors for only one syringe is presented for analysis here, it is evident that the percentage differences observed in the model, while consistent for this type of calibrator, are somewhat reduced to those quoted for other chambers in the literature. As previously explained, the design of the chambers varies little and it is mainly the composition of the chamber materials and gas that change between models. The literature predominately presents chambers with argon as a chamber gas. An analysis of the Fidelis sensitivity curve with argon gas is therefore presented for comparison with nitrogen.

5.4 Fidelis chamber sensitivity curve with argon gas

The sensitivity curve for an argon filled chamber has been experimentally determined and presented in the literature previously (Suzuki et al., 1976). Figure 5.4 shows the sensitivity curve for a Capintec calibrator filled with argon.

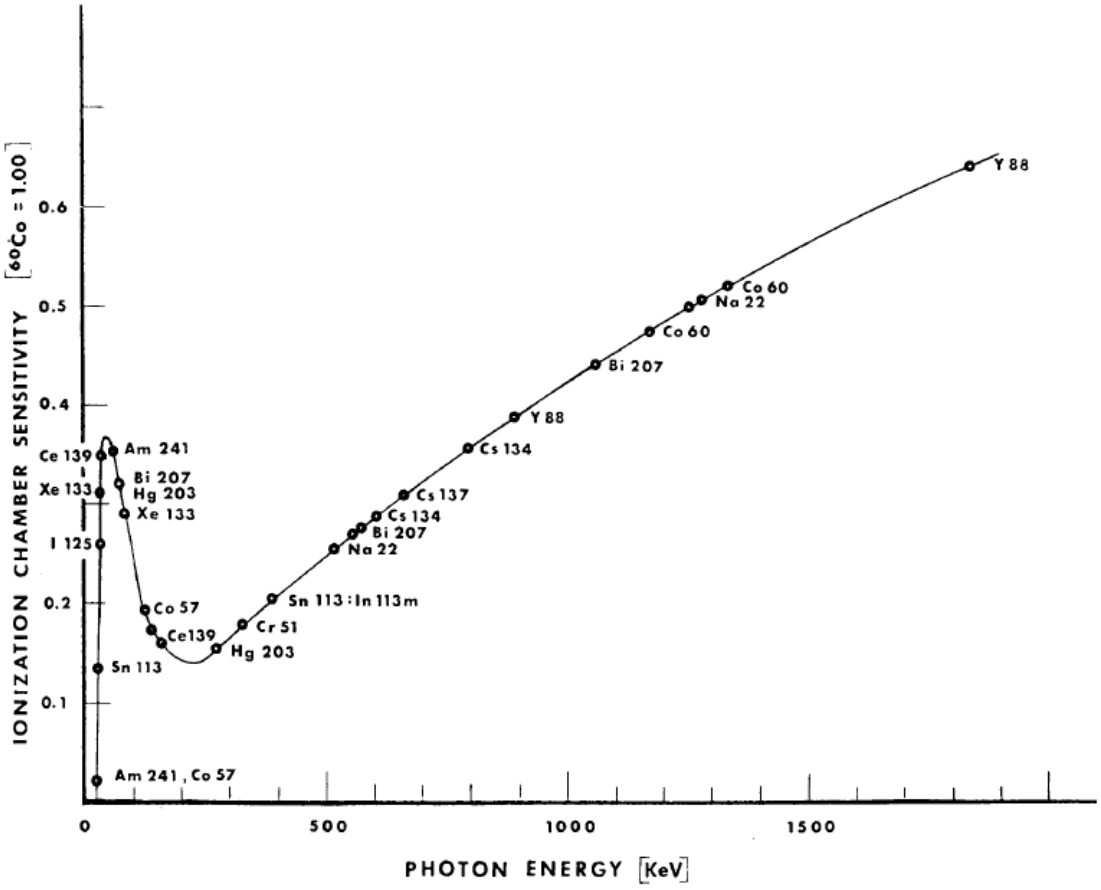

Figure 5.4: Sensitivity curve for a Capintec argon filled calibrator (reproduced from (Suzuki et al., 1976)).

The Monte Carlo model used in Chapter 4 was adjusted to change the chamber gas from nitrogen to argon. Argon has an atomic number of 18 as compared to 7 for nitrogen. The pressure of the argon gas was kept consistent with the nitrogen gas at 1 MPa.

The individual gas constant for argon is 208.1 J kg^{-1} K^{-1} and the density of the gas was calculated to be 0.01634 g cm^{-3}.

The results of the simulations can be seen in table 5.3 and are graphically displayed in Figure 5.5.

Photon Energy keV	Energy deposited MeV	Energy deposited keV	Energy deposited eV
10	0	0.0	0.0
20	3.69×10^{-04}	0.3694	369.4
25	1.39×10^{-03}	1.3899	1389.9
30	2.31×10^{-03}	2.3058	2305.8
35	2.75×10^{-03}	2.7495	2749.5
40	2.81×10^{-03}	2.8097	2809.7
45	2.68×10^{-03}	2.6774	2677.4
50	2.46×10^{-03}	2.4600	2460.0
55	2.23×10^{-03}	2.2298	2229.8
60	2.02×10^{-03}	2.0168	2016.8
65	1.82×10^{-03}	1.8216	1821.6
70	1.65×10^{-03}	1.6509	1650.9
75	1.50×10^{-03}	1.5031	1503.1
80	1.38×10^{-03}	1.3788	1378.8
85	1.27×10^{-03}	1.2710	1271.0
90	1.18×10^{-03}	1.1802	1180.2
95	1.10×10^{-03}	1.1027	1102.7
100	1.04×10^{-03}	1.0366	1036.6
125	8.34×10^{-04}	0.8335	833.5
150	7.51×10^{-04}	0.7505	750.5
175	7.30×10^{-04}	0.7296	729.6
200	7.42×10^{-04}	0.7418	741.8
225	7.73×10^{-04}	0.7731	773.1
250	8.18×10^{-04}	0.8181	818.1
275	8.69×10^{-04}	0.8694	869.4
300	9.26×10^{-04}	0.9258	925.8
400	1.18×10^{-03}	1.1751	1175.1
500	1.43×10^{-03}	1.4329	1432.9
600	1.69×10^{-03}	1.6862	1686.2
700	1.93×10^{-03}	1.9319	1931.9

Table 5.3: Energy deposited per starting particle in the argon gas

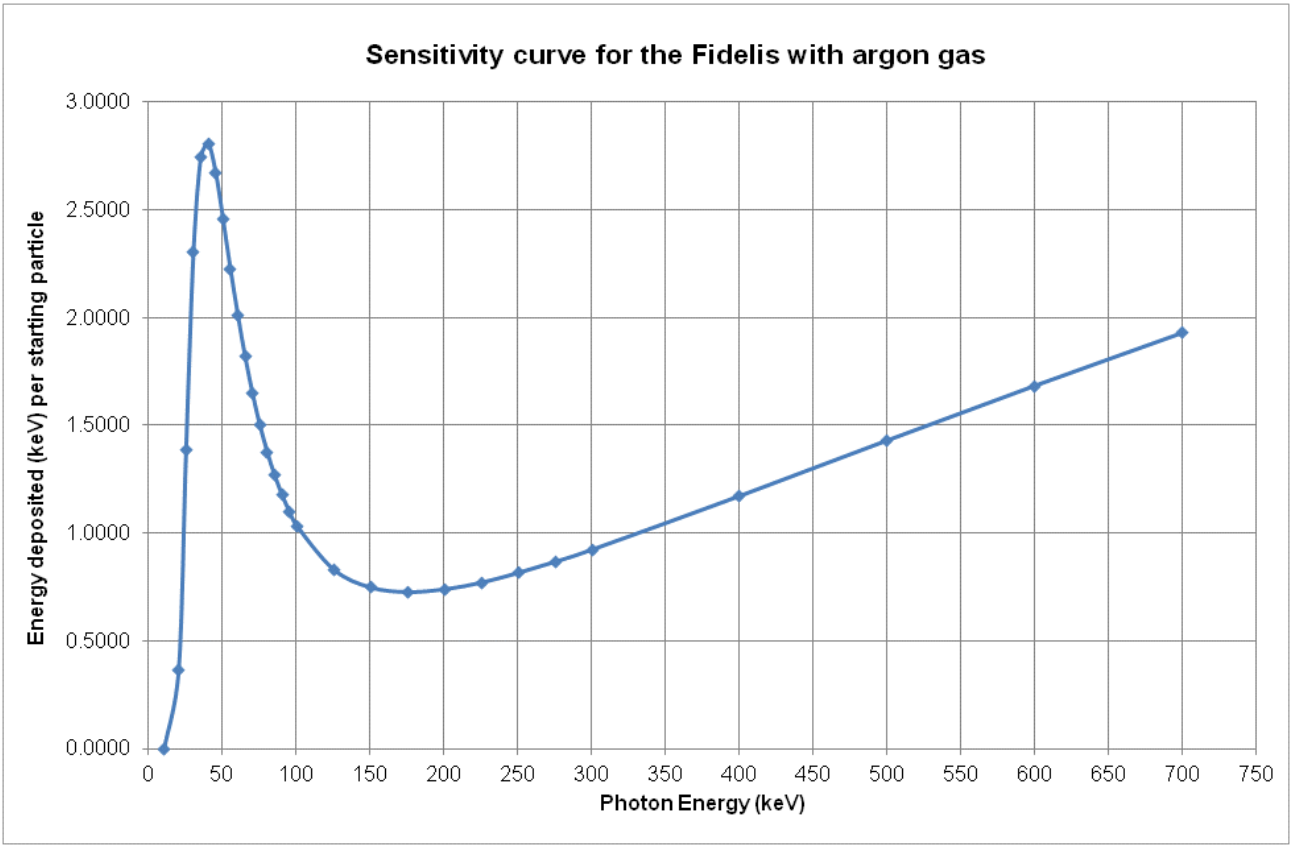

Figure 5.5: Monte Carlo sensitivity curve for the Fidelis with argon gas

5.4.1 Discussion Fidelis chamber sensitivity curve with argon gas

The sensitivity curve for the Fidelis chamber with argon gas shows a marked difference from the nitrogen sensitivity curve as shown in Figure 4.8. The argon sensitivity curve closely resembles the shape of the Capintec curve published by Suzuki et al. (1976). A peak in the sensitivity curve is seen at approximately 45 keV, with significant variation in sensitivity between 10 and 45 keV, the range in which the characteristic x-ray emissions of ^{123}I occur. The main gamma emission of ^{123}I (159 keV) appears close to a local minimum within the sensitivity curve. For nitrogen the principal ^{123}I gamma emission was approximately four times as great as that of the characteristic x-rays (from the sensitivity curve). For argon, we see that the relative

sensitivity has switched in favour of the characteristic x-rays, ranging from unity to three times more sensitive for x-rays in the region of 27 – 31 keV.

5.4.2 Derivation of syringe calibration factors for fidelis filled with argon

To investigate further the use of argon as the chamber gas in the Fidelis, the experiments simulated in sections 5.3.1 and 5.3.3 were repeated.

The variation in energy deposited per syringe volume can be seen in Table 5.4 and graphically displayed in Figure 5.6.

Syringe volume	Energy deposited (MeV)	Energy deposited (eV)	Variation
0.1	2.32×10^{-03}	2323.44	1.000
0.2	2.31×10^{-03}	2309.26	0.994
0.3	2.31×10^{-03}	2305.57	0.992
0.4	2.30×10^{-03}	2302.99	0.991
0.5	2.30×10^{-03}	2301.24	0.990

Table 5.4: syringe volume variation with argon gas

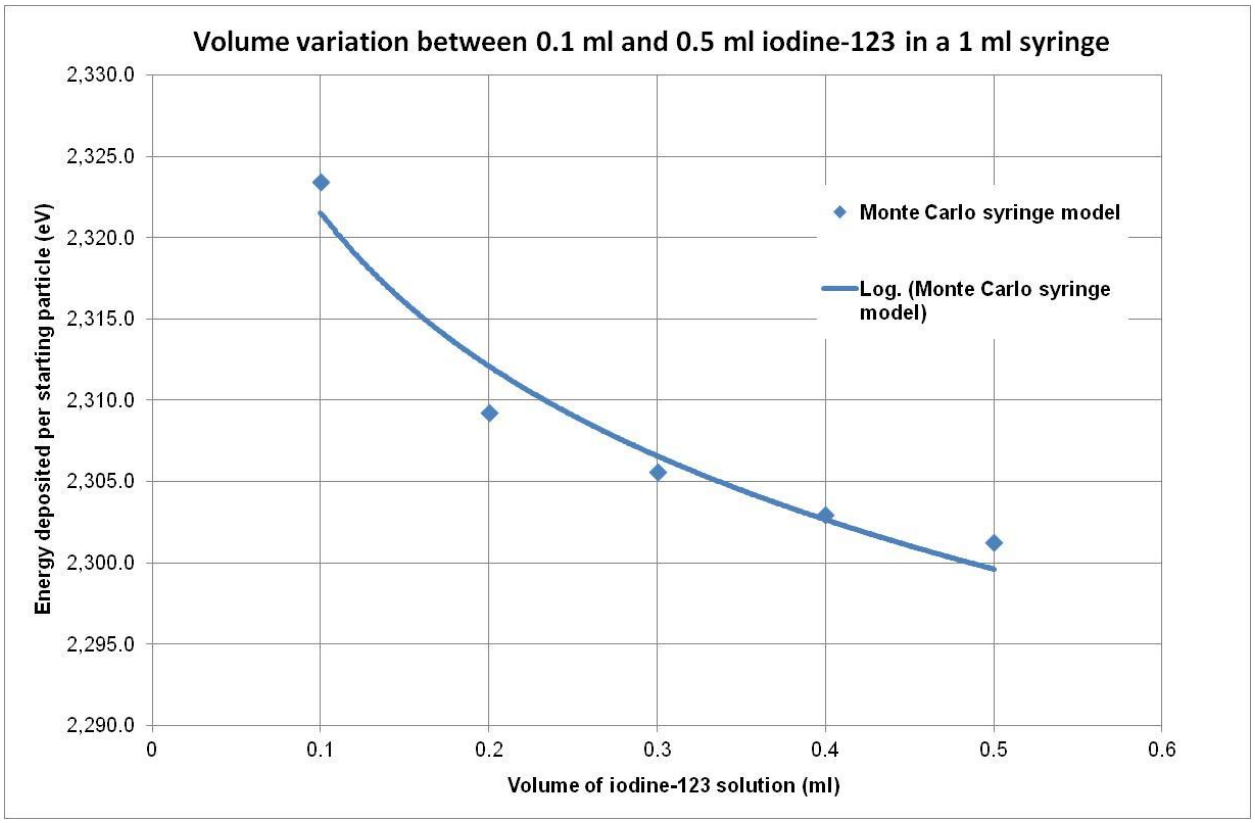

Figure 5.6: Syringe volume variation for 1 ml BD Plastipak™ syringe with a Fidelis argon filled chamber

The variation in energy deposited by the 1 ml BD Plastipak™ syringe for different volumes can be compared with the P6 vial as shown in Table 5.5. There are no published calibration factors for the Fidelis with argon chamber gas. An estimation of the Fidelis chamber factor was undertaken as follows. The ratio of the energy deposited in the gas for a P6 vial was taken for the argon gas compared to the nitrogen gas and multiplied by the P6 calibration factor for nitrogen. This results in a calibration factor of 11.48 pA/MBq for a P6 vial in an argon filled Fidelis as opposed to 1.685 pA/MBq for nitrogen filled Fidelis.

Container	Volume (ml)	Energy deposited (MeV)	Fidelis derived calibration factor (pA/MBq)	% difference to vial
P6 vial	4.0	1.38×10^{-03}	11.48	0.0
BD Plastipak™ 1ml syringe	0.1	2.32×10^{-03}	16.05	68.8
BD Plastipak™ 1ml syringe	0.2	2.31×10^{-03}	16.01	67.8
BD Plastipak™ 1ml syringe	0.3	2.31×10^{-03}	16.00	67.5
BD Plastipak™ 1ml syringe	0.4	2.30×10^{-03}	16.00	67.3
BD Plastipak™ 1ml syringe	0.5	2.30×10^{-03}	16.00	67.2

Table 5.5: Percentage difference between the vial and the syringe simulations for argon gas

5.4.3 Discussion of derived of syringe calibration factors for the fidelis filled with argon

The results validate some of the previous work that shows a range of 60 – 80 % difference in the reading between a vial and a syringe in an argon filled chamber. This is an interesting observation as it means that nitrogen filled chambers are more advantageous than argon filled chambers in ensuring a smaller variation when assaying ^{123}I. The variation in calibrator response between a P6 vial and a 1 ml syringe for a nitrogen filled chamber was found to be up to 21%. The reason for the reduced variation can be deduced from Figures 4.8 and 4.9. The sensitivity of the chamber to the low energy x-ray emissions of ^{123}I is four times less than the principal gamma peak. Hence the contribution of the x-rays to the response of the chamber is lower than that observed for argon gas. One of the reasons why argon remains

more prevalent within radionuclide calibrators can be seen with the sensitivity curve for argon and the derived argon calibration factors. The energy deposited in the chamber is of the order of ten times higher for argon as opposed to nitrogen. This is advantageous in terms of optimising the amount of ionisation current produced per unit activity which, in turn, may lead to an increase in accuracy of ionisation current measurement.

5.5 Use of a copper filter in the Fidelis

As has been previously demonstrated, the degree of correction for a syringe in a Fidelis nitrogen filled chamber is somewhat lower than that for an argon filled chamber. The most commonly applied approach for correcting this discrepancy is the use of a copper filter. The following simulations were undertaken to determine the optimum thickness of copper to negate the discrepancy for nitrogen and argon filled Fidelis chambers. In both cases the copper filter was simulated in the Fidelis chamber. The vial jig was removed for the simulations with the copper filter. The geometry for the syringe can be seen in Figure 5.7. The length of the copper filter was such that it extended beyond the length of the calibrator.

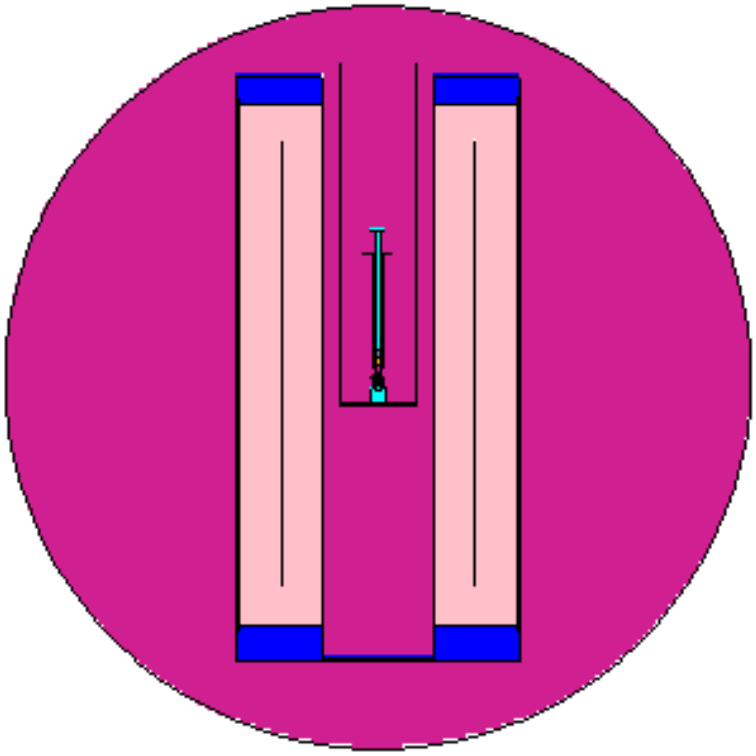

Figure 5.7: Fidelis calibrator with syringe and copper filter

The simulations were undertaken from 0.05 mm to 1.0 mm of copper and compared with the result without copper. The results are tabulated in Table 5.6. A graphical representation of the ratio of the copper filter measurements for nitrogen and argon can be seen in Figure 5.8.

	Nitrogen			Argon		
Cu filter thickness (mm)	Syringe Energy deposited (MeV)	Vial Energy deposited (MeV)	Ratio	Syringe Energy deposited (MeV)	Vial Energy deposited (MeV)	Ratio
0	2.44×10^{-4}	2.02×10^{-4}	1.207	2.32×10^{-3}	1.38×10^{-3}	1.688
0.05	2.05×10^{-4}	1.85×10^{-4}	1.109	1.33×10^{-3}	8.93×10^{-4}	1.487
0.1	1.86×10^{-4}	1.74×10^{-4}	1.070	8.55×10^{-4}	6.36×10^{-4}	1.344
0.2	1.71×10^{-4}	1.65×10^{-4}	1.038	4.98×10^{-4}	4.40×10^{-4}	1.133
0.3	1.66×10^{-4}	1.61×10^{-4}	1.029	4.00×10^{-4}	3.84×10^{-4}	1.041
0.4	1.63×10^{-4}	1.58×10^{-4}	1.027	3.68×10^{-4}	3.65×10^{-4}	1.010
0.5	1.60×10^{-4}	1.56×10^{-4}	1.028	3.55×10^{-4}	3.55×10^{-4}	1.001
0.6	1.58×10^{-4}	1.54×10^{-4}	1.029	3.49×10^{-4}	3.49×10^{-4}	0.999
0.7	1.56×10^{-4}	1.51×10^{-4}	1.029	3.43×10^{-4}	3.44×10^{-4}	0.999
0.8	1.54×10^{-4}	1.49×10^{-4}	1.030	3.38×10^{-4}	3.39×10^{-4}	1.000
0.9	1.51×10^{-4}	1.47×10^{-4}	1.031	3.34×10^{-4}	3.33×10^{-4}	1.002
1	1.49×10^{-4}	1.45×10^{-4}	1.032	3.30×10^{-4}	3.28×10^{-4}	1.004

Table 5.6: Syringe and vial energy deposition in nitrogen or argon with varying thicknesses of copper

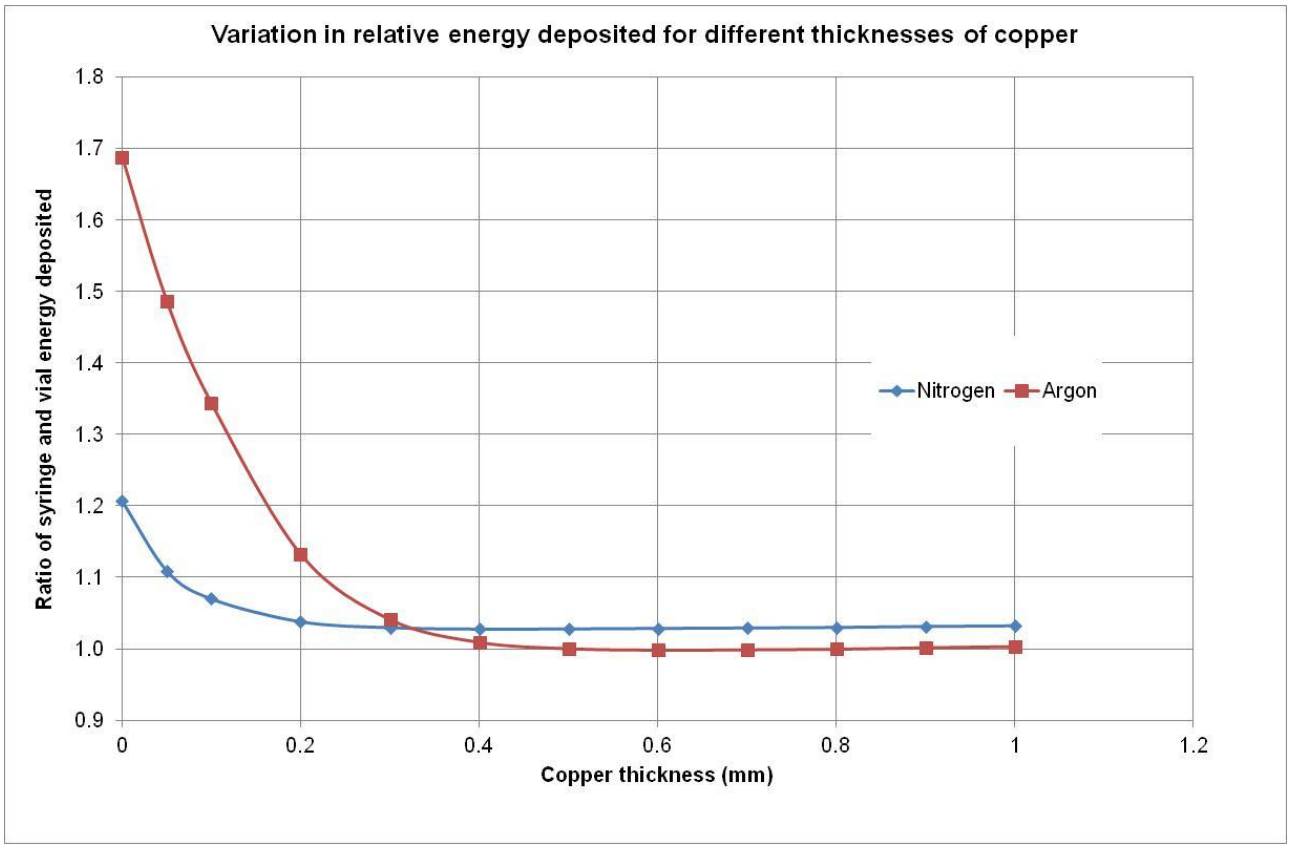

Figure 5.8: Copper filter ratios for nitrogen and argon

5.5.1 Discussion of the use of a copper filter in the Fidelis

From Table 5.6 and Figure 5.8 we can again see the variation in energy deposited between a syringe and a vial copper filtration. The optimal copper filtration thickness for the nitrogen filled Fidelis is 0.3 mm, where the ratio of the syringe and vial readings stabilises to 3% of each other. For the argon filled Fidelis, stability is not achieved until 0.5 mm of copper filtration. However, the ratios of the syringe and vial measurements are unity, meaning that a copper filter is an excellent choice for a argon filled calibrator. The copper filter Fidelis calibration factors can be calculated by comparing the ratio of energy deposited in the gas with and without the optimal thickness of copper filtration. This can then be related to either the NPL published

factor for a P6 vial or the factor derived for the Fidelis with nitrogen. For nitrogen with a 0.3 mm thick copper filter, the ^{123}I copper filter calibration factor is 1.34 pA/MBq and for argon, the factor is 2.96 pA/MBq with 0.5 mm copper filtration.

5.6 Copper filter field radionuclide calibrator determination

For subsequent syringe measurements, it is necessary to cross-calibrate a field radionuclide calibrator for ^{123}I. The Medical Physics Department has three Capintec-CRC15R radionuclide calibrators for the routine assay of radiopharmaceuticals.

A 4 ml solution of ^{123}I was dispensed into a Schott vial with the weight of the vial measured before and after filling to determine the mass of the solution. The activity of the Schott vial was then ascertained on the Fidelis calibrator using the appropriate calibrator factor.

The activity of the Schott vial was measured using the three Capintec Calibrators with a 0.6 mm copper filter and compared to the Fidelis measurement. The Capintec calibration factor was adjusted when using the copper filter to show the same decay corrected reading as the Fidelis.

5.6.1 Results

The activity of the ^{123}I in the Schott vial was 140.4 MBq as assayed in the Fidelis. A Capintec calibration factor of #54 was derived based on the best concordance with the decay corrected Fidelis measurement. This copper filter calibration factor was implemented into routine practice and used for subsequent measurements in chapter 7.

5.7 Summary

In this chapter a number of investigations were undertaken to determine the uncertainty in measuring ^{123}I in a vial as compared to a syringe using the Fidelis. The results showed that for nitrogen filled chambers, up to 21% variation in measurement was seen. Based on the Monte Carlo simulations, a method for determining syringe calibration factors was devised and a number of Fidelis calibration factors for a BD Plastipak™ 1ml syringe were derived.

The majority of commercially available calibrators employ argon as a chamber gas as opposed to nitrogen. The benefit of using argon is that its higher atomic number means the cross-section for the photoelectric effect is significantly higher. This result was evident when a sensitivity curve was generated for the Fidelis using argon as the chamber gas. The sensitivity curve derived for the argon filled chamber was similar to that previously seen in the literature (Suzuki et al., 1976). When comparing the ^{123}I vial and syringe measurements, up to 69% variation was observed. Again, this is in keeping with previously reported variations in the literature.

Finally, copper filter simulations were undertaken for the syringe and vial for both nitrogen and argon filled Fidelis chambers. Copper was shown to be an effective attenuating material for the low energy x-ray emissions of ^{123}I. For a nitrogen filled Fidelis chamber, 0.3 mm copper was sufficient to reduce the variation in the vial and syringe measurement to 3%. For argon, approximately double the copper filter thickness was required to reach unity in the ratio.

CHAPTER 6: RADIOIODINE THYROID UPTAKE AND ASSOCIATED UNCERTAINTIES

6.1 Introduction

In the previous two chapters, the potential uncertainties of the assay of ^{123}I were detailed. In this chapter, the application of radioiodine in nuclear medicine is presented. The anatomy and physiology of the thyroid gland is described as the predominant target tissue following radioiodine administration. The thyroid uptake assessment as a means to differentiate between different thyroid diseases is detailed along with a discussion of some of the inherent uncertainties in the assessment. Finally, the aim of this section of work is presented.

6.2 The thyroid gland

The thyroid gland is a member of the endocrine system of glands. Along with the nervous system, one of the roles of the endocrine system is to maintain a stable internal environment within the body. To achieve this, glands secrete hormones into the blood stream and these target specific cells. The effects of the hormone are manifested in all parts of the body that have recepter cells specific to that hormone. The thyroid gland is located in the neck and consists of two lateral lobes (right thyroid gland and left thyroid gland) and a narrow connecting isthmus (Figure 6.1). The thyroid is anterolateral to the trachea and located below the larynx (Patton and Thibodeau, 2013).

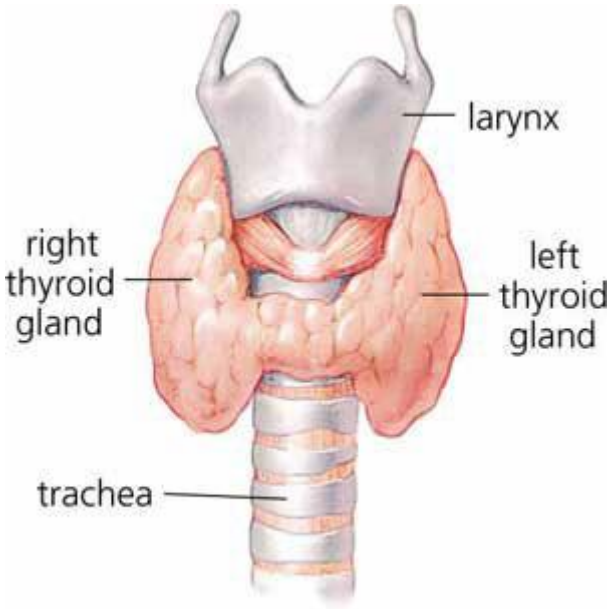

Figure 6.1: Schematic of the thyroid gland (MedicalTerms.info, 2012)

The tissues within the thyroid gland contain small spherical follicular cells which absorb I^- from the blood. Once within the follicles, I^- is converted to iodine before being synthesised and stored as a precursor to the excreted thyroid hormones. Iodine is therefore an important part of an individual's dietary intake and it is essential to ensure sufficient blood concentrations are available for absorption into the thyroid gland (and the subsequent production and release of thyroid hormones).

The two main excreted hormones are T_3 and T_4, with the latter commonly known as thyroxine. The thyroid gland is stimulated to release thyroid hormones due to the influence of TSH, which is released from the pituitary gland. The release of T_3 and T_4 into the blood results in an increase in the metabolic rate of cells. Through negative feedback, the levels of T_3 and T_4 are maintained within the blood to ensure normal rates of cell metabolism.

6.3 Diseases of the thyroid

A number of diseases (both malignant and benign) have been identified that are related to the function of the thyroid. Of particular interest to nuclear medicine applications include thyroid cancers, hyperthyroidism and hypothyroidism. This study concentrates only on the diagnostic nuclear medicine assessment of hyperthyroidism and hypothyroidism.

Hyperthyroidism (clinically known as thyrotoxicosis) is defined as the syndrome resulting from an excessive amount of circulating thyroid hormones. As the thyroid hormones are present throughout the body, an excess of hormones will affect a number of functional systems including the cardiovascular, respiratory and gastrointestinal systems. Clinical signs and symptoms of hyperthyroidism include increased heart rate, behavioural changes, anxiety and decrease in weight due to the increased cellular metabolic rate (Lazarus, 1994). A number of different etiologies can cause hyperthyroidism, with the most prevalent being Graves' disease (Vanderpump, 2011). The three main treatments for Graves' disease are anti-thyroid medications, sub-total thyroidectomy and radioiodine (Wheetman, 1994).

Hypothyroidism is a term collectively used to describe a number of diseases that result in a reduction in thyroid hormones or, more rarely, a moderation of their effect on tissues (Amino and Tachi, 1994). Common symptoms of hypothyroidism include tiredness, lack of concentration, cold intolerance and unexplained weight gain (Ladenson, 2003). Similar to hyperthyroidism, a number of different etiologies can cause the condition including dietary iodine insufficiency. The most common cause of hypothyroidism in iodine-replete individuals is conditions of an autoimmune

nature, including Hashimoto's thyroiditis (Amino and Tachi, 1994). Hypothyroidism can usually be effectively treated with medications designed to synthetically replace the depleted thyroid hormones blood levels.

6.4 Nuclear medicine thyroid uptake assessment

Clinical diagnosis of hypo- or hyperthyroidism is usually based on a detailed patient history and biochemical testing. Although generally sufficient to make a diagnosis of hypo- or hyperthyroidism, the exact etiology of the underlying disease may not be apparent from such assessments. This is especially important to ascertain as the choice of therapy is dictated by the cause of the condition.

The assessment of radioiodine thyroid uptake has become a widespread diagnostic nuclear medicine tool for assisting in the differentiation of hypothyroidism, or more usually, hyperthyroidism etiologies. The thyroid uptake is expressed as the percentage of administered radioiodine in the thyroid at a given time post administration. For hyperthyroidism, disorders can be separated into those that result in a high radioiodine uptake and those with a low radioiodine uptake. High radioiodine uptake treatments include medications, radioiodine therapy and surgery. Low radioiodine uptake is also associated with inflammatory thyroid conditions (subacute thyroiditis) or an extrathyroidal source of thyroid hormones. In this case, radioiodine is not an appropriate therapy as uptake of the tracer in the thyroid is very low and would provide little therapeutic benefit. Medications are often employed and found to be effective in offering symptomatic relief (such as beta-adrenergic blocking agents) for the majority of patients (Ross, 2003).

The thyroid uptake counter is one of two pieces of equipment used to assess the uptake of radioiodine within the thyroid. The other commonly used piece of equipment is a gamma camera, where the assessment of radioiodine uptake is undertaken in conjunction with imaging the radiopharmaceutical distribution in the thyroid gland. The measurement technique consists of the administration of radioiodine and following a suitable uptake period, typically of the order of 2 to 6 hours, the accumulation of the radioiodine in the thyroid is assessed by the relative thyroid external radiation measurement compared to a standard activity within an appropriate tissue equivalent phantom.

The two main radionuclides used for the assessment of thyroid uptake are ^{131}I and ^{123}I, which are usually administered orally in the form of sodium iodide solution. The radioiodine is absorbed by the thyroid gland and is effectively trapped for the duration of the investigation. Biologically, both isotopes are treated identically in the body. Historically, ^{131}I was commonly used for thyroid uptake assessments as it was the more widely available radioiodine. With the widespread availability of ^{123}I in the 1980s, ^{123}I uptake assessments were found to be an effective surrogate for ^{131}I with the added advantage of reduced patient radiation dose and completion of the assessment on the same day as administration (Floyd et al., 1985).

Like other nuclear medicine diagnostic procedures, standardisation of data acquisition is essential for reproducible thyroid uptake assessments and interpretation. Standardisation of the thyroid uptake measurement technique using ^{131}I was first proposed by the IAEA to ensure a consistent approach in the assessment (IAEA, 1962). More recent guidelines for undertaking the thyroid uptake assessment have been developed by the BNMS (BNMS, 2003) and the SNM (Balon et al., 2006). The SNM guidelines also quote a normal ^{123}I thyroid uptake reference range of between 6% and 18% (for a 4 hour uptake), although, the guidelines caution that reference ranges may be influenced by other factors including the available equipment and patient population.

6.5 Review of the uncertainties associated with thyroid uptake assessments

The need for a consistent measurement technique has been well documented to ensure the validity and reproducibility of thyroid uptake assessments. The measurement usually consists of an assessment of the radioactivity in the neck as compared to a similar assessment of the radioactivity in a surrogate neck phantom. The measurements are usually conducted over a short period of each other and therefore the need to decay correct between each measurement is negated. An alternative approach, as adopted by the Medical Physics Department at the University Hospital of Wales, is to undertake two neck phantom measurements, as soon as possible prior to and then proceeding the neck assessment. The average of these measurements is therefore seen as an approximate mean value of the neck phantom measurements at the time of the patient measurements. It is important to note that the thyroid uptake assessment is not an absolute assessment of the radioiodine uptake in the thyroid, but a relative assessment as compared to a

suitable standard, as in this case, an equivalent or scaled activity of the radionuclide administered to the patient in a neck phantom. As previously noted, the need to determine normal ranges locally for the equipment and measurement arrangements is acknowledged by the SNM and published normal ranges should be used with caution (Balon et al., 2006). The SNM procedural guidelines identify the following as potential sources of error (Balon et al., 2006):

- Variations in neck to detector distance
- Inappropriate neck phantom
- Improper centring of the probe over the patient's neck
- Electronic instability
- Background variation
- Interfering food or medications
- Contamination of the neck phantom
- Recent administration of other radionuclides

Each source of uncertainty is further explored along with an analysis of the potential detriment to the accuracy of the thyroid uptake assessment.

6.5.1 Variations in neck to detector distance

Variations in neck to detector distance will originate from either poorly reproduced setup between the neck phantom and patient measurements or variations in thyroid depth within the patients neck. Typical measurement distances between the neck and the surface of the detector are in the range 25 and 30 cm (Balon et al., 2006). Any change in distance from the surface of the neck to the face of the detector will affect the measurement due to the inverse square law, resulting in an increase or decrease in the flux of photons hitting the face of the detector. Due to the nature of the inverse square law, small variations in distance can propagate as significant differences in flux at the face of the detector. For example, a change of 1 cm from 29 cm to 30 cm would result in a difference of 6.6% in the measured flux at the surface of the detector. Some method is therefore required to ensure that the neck to detector or phantom to detector distance remains consistent between measurements. Within the Medical Physics Department at the University Hospital of Wales, a 10 cm spacer is located at the end of the detector collimator to assist in the vertical positioning of the detector above the patients neck.

The effect of variations in thyroid depth in the neck on the thyroid uptake assessment will be two fold. Firstly, the distance will increase between the thyroid and the detector. As discussed in the previous paragraph, any changes in thyroid to detector distance will have a deleterious effect due to the inverse square law. Secondly, the amount of soft tissue between the thyroid and the face of the detector will also increase (in the case of increased thyroid depth). The result will be an increase in soft tissue attenuation via photoelectric absorption and Compton scattering. Any

increase in attenuation will ultimately affect the number of photons emanating from the thyroid that are measured within the counting window and incorporated into the thyroid uptake assessment.

Variation in the size of the thyroid, the depth of the thyroid in the neck and separation of the thyroid lobes has been previously investigated. In a phantom study by O'Connor and Malone (1978), a strong dependence on the activity measured using a thyroid uptake counter was found with respect to thyroid depth for ^{131}I, ^{99m}Tc and ^{125}I. A much weaker dependence on variations in thyroid size and lobe separation was determined. The authors also noted the range of typical thyroid depths and standard deviation in the population and indicated that there were significant variations.

The estimation of a correction factor for thyroid depth following ^{123}I administration has been proposed previously by Martin and Rollo (1977). The method involved taking the ratio of the measured counts in the x-ray peak and those measured in the main gamma peak. The authors were able to produce a calibration curve to correct for thyroid depth. In a sample of 40 patients, the authors estimated a mean thyroid depth of 2.74 cm with the majority of thyroids at a greater depth than 1.5 cm, corresponding to the depth of the surrogate thyroid in the thyroid phantom. This discrepancy, once corrected, resulted in a increase of 23% in the uptake measurements on average and in the extreme up to +130% (Martin and Rollo, 1977). However, the depth correction was based on a neck and thyroid gland phantom in which the depth of the thyroid was simulated with test tubes containing ^{123}I. Applying this approach to a clinical situation is uncertain as the depth of the

thyroid in the neck is not likely to be uniform in all directions and specific to a particular patient.

More recently, a phantom study has been undertaken to assess the uncertainties in the determination of ^{131}I activity with varying thyroid positions in the neck (Ośko et al., 2007). A correction factor for thyroid depth was devised based on the ratio of counts in the principal gamma peak of ^{131}I compared to a region in the Compton scattering band. When applying the calibration to a group of 95 patients, thyroid depths in excess of the standard 20 mm depth were noted. A variation in ^{131}I activity up to 30% due to thyroid depth was seen for the majority of patients.

6.5.2 Inappropriate neck phantom

As previously mentioned, quantitative radioiodine uptake in the thyroid is not the primary function of a standard thyroid uptake assessment. The assessment is based on a comparison against a standard neck phantom and therefore the dimensions and composition of the phantom are going to determine the value of the calculated thyroid uptake assessment. The IAEA guidance recommends a PMMA neck phantom for assessment of radioiodine thyroid uptake (IAEA, 1962). Vahjen et al. (1992) demonstrated significant differences in the assessment of thyroid uptake when using a water phantom as opposed to the recommended PMMA phantom. This was due to the differing attenuation properties and dimensions of the different phantoms. In some cases, they noted for patients with high radioiodine uptake, estimation of the thyroid uptake was in excess of 100% when using the water phantom. A PMMA type phantom as suggested by the IAEA was deemed to be more

appropriate (Vahjen et al., 1992). Vahjen et al. (1992) also noted the importance of considering the differences in phantoms when comparing thyroid uptake measurements between different centres. Chervu et al. (1982) also demonstrated significant errors, up to 23%, were seen when using three different "IAEA neck phantoms" with slight differences in ^{123}I source positioning.

As an alternative to using a neck phantom, the use of dual energy ^{123}I imaging has been reported by Shapiro et al. (2014) for assessing thyroid uptake. In this case imaging of the thyroid was undertaken on a gamma camera using the 159 keV principal gamma emission photopeak window and a 130 keV scatter window. The ratio of thyroid counts in the two respective images was used to compensate for the loss of counts due to absorption in the neck. A high degree of concordance was noted between the results of the proposed method and uptake as assessed via 24 hour urine sampling. This method indicates another application of dual counting in the iodine spectrum as detailed in the previous section.

6.5.3 Improper centring of the uptake counter over the patient's neck

Improper centring of the uptake counter over the patient's neck is acknowledged to be a source of error but is noted as not having been examined in the literature to any great extent. Improper centring of the uptake counter is due to lateral error in positioning above the thyroid gland. Positioning is usually undertaken without any adjunct imaging and is mainly based on the operator’s expectation of the likely position of the thyroid gland. Another source of positioning error that can be introduced is via a slight tilt in the detector away from the normal to the thyroid. Any

tilt will result in the face of the detector not presenting at 90° to the thyroid gland. The result would be a reduction in the assessment of thyroid uptake, as the angle of acceptance of gamma rays emitting from the thyroid will effectively be reduced.

6.5.4 Electronic instability

Any electronic instability in the thyroid uptake counter equipment will have a negative effect on the thyroid uptake assessment. An assessment to simulate the effect of electronic instability was undertaken by Chervu et al. (1982) by varying the high voltage applied to the PMT and determining the variation of the detected counts as measured by a single channel analyser. The results showed that significant errors can be introduced if the high voltage is unstable and the time between the neck and thyroid measurements is protracted.

It has also been demonstrated that dead time issues result in significant uncertainty in the thyroid uptake assessment. Maguire (1998) assessed the dead time losses for 3.7 MBq ^{123}I in a thyroid phantom measured on three different thyroid uptake counter systems. Two systems showed a percentage error between the measured and expected count rate of 1.2% and 4.4% respectively. The remaining system showed a much larger error of 25.2%. Lee et al. (1995) also demonstrated 10% count losses for a thyroid uptake counter for 1.85 MBq ^{123}I in a thyroid phantom

6.5.5 Background variation

Background variations can be an issue and is determined by the ambient background in the vicinity of the uptake counter and via a contribution from extra thyroidal accumulation of the radiopharmaceutical.

Ambient background count rates in the vicinity of the uptake counter will depend on the location of the counter with respect to natural and artificial sources of radiation. Short term variability may be somewhat unavoidable, for example due to other patients in the vicinity who have been administered radiopharmaceuticals. The current practice in the Medical Physics Department at the University Hospital of Wales is to undertake a background count rate check prior to use [in this regard one is also assessing if the thyroid uptake counter is contaminated]. When using a spectral display, any discrepancies between the expected background spectrum displayed and that observed should warrant further inspection.

The contribution of extra thyroidal radiopharmaceutical accumulation may influence the thyroid uptake assessment. The use of a collimator on the uptake counter is designed to reduce the influence of radiopharmaceutical accumulation outside of the thyroid. However, a certain proportion of blood and tissue accumulation above and below the thyroid will contribute to the assessment. An assessment of extra thyroidal uptake may be made by undertaking a background measurement on the leg, taken as an approximation to the neck. Subsequent measurements can be background corrected based on this value.

6.5.6 Interfering food/medications

Both the BNMS and SNM guidelines outline the issues surrounding excessive dietary intake of iodine prior to the assessment. This is negated by patient counselling prior to the assessments.

6.5.7 Contamination of the neck phantom

Radioactive contamination of the neck phantom will result in a falsely high count rate when measured. Any increase in phantom count rate when compared to the patient will result in a lower assessment of the thyroid uptake. Radioactive contamination of the neck phantom may be identified as an unusually high count rate compared to that expected. Radioactive contamination monitoring of the phantom using a suitable radiation monitor would be able to distinguish between an issue with the ambient background or if indeed the phantom has become contamination. If the latter is true, the phantom would not be suitable for thyroid uptake assessments until fully decontaminated (either via decontamination techniques or allowing for sufficient natural radioactive decay).

6.5.8 Recent administration of other radionuclides

Any other recent administrations of radiopharmaceuticals to the patient may produce erroneous results. The effective half-life of the competing radiopharmaceutical needs to be borne in mind when considering the appropriateness of a thyroid uptake assessment following other administrations.

6.6 Monte Carlo modelling of a thyroid uptake counter

Monte Carlo techniques have been previously used to model a thyroid uptake counter. Scarboro et al. (2009) detailed the MCNP modelling of a Captus 3000 thyroid uptake counter and the associated validation measurements for a number of radionuclides. The potential application suggested by the authors was to use the thyroid uptake monitor as a screening and internal dosimetry tool in the event of a radiological incident.

Monte Carlo techniques have also been used to address some of the uncertainties identified in the previous sections. Kramer and Crowley (2000) undertook MCNP simulations of various thyroid sizes and shapes for ^{125}I and ^{131}I and found uncertainties in the thyroid uptake measurement to be dependant on detector size, neck to detector position and the radioiodine used. In a seperate paper, Kramer et al. (1997) investigated the optimisation of the thyroid uptake counter for ^{125}I and ^{131}I measurements. Using the EGS4 Monte Carlo code, Ulanovsky et al. (1997) modelled a thyroid uptake counter and simulated ^{131}I variations in thyroid detector distance and angular shift. Uncertainties in the range of -32% to +17% were observed. In a separate paper, Monte Carlo simulations (written in Pascal) were undertaken for a 3" × 3" thyroid uptake detector and a thyroid and neck model (Venturini, 2003). A combined uncertainty of up to 18% was found for the photopeak efficiency when modelling a 12 year old thyroid (taken as the limit for the adult thyroid) and a 20 year old thyroid. Bento et al. (2012) described the PENELOPE modelling of a 2" × 2" NaI ORTEC detector. Uncertainty in thyroid monitoring arising from varying neck to detector distance was found to be 12-38%.

6.7 Aims of the study

The current published literature has identified some of the issues with accurate assessment of radioiodine thyroid uptake. Variations in collimator to neck distance, lateral displacement of the detector and thyroid depth have been acknowledged as factors in limiting the reliability of the thyroid uptake assessment accuracy. Some authors have suggested possible correction strategies for the uptake measurement, for example using the ratio of different parts of the acquired gamma spectrum to determine correction factors (Martin and Rollo, 1977) (Ośko et al., 2007) (Shapiro et al., 2014). However, this previous work has predominantly been undertaken experimentally, with the inherent limitations implied by this approach.

The purpose of the following investigations is to use Monte Carlo simulations to determine the degree of uncertainty for the particular thyroid uptake counter used within the Medical Physics Department of the University Hospital of Wales. Also, for the particular case of thyroid depth, produce a depth based thyroid correction strategy for ^{123}I thyroid uptake assessments that can reasonably be adopted into routine clinical practice

CHAPTER 7: MONTE CARLO THYROID UPTAKE COUNTER MODEL AND VALIDATION

7.1 Introduction

The core components of a thyroid uptake counter include a collimator, a scintillation crystal, a PMT, amplifier electronic circuitry and pulse height determination electronics. The main difference between a thyroid uptake counter and a gamma camera is that the gamma camera will usually consist of 60 or more PMTs and the signal processing electronics are designed to produce an image of the radiopharmaceutical distribution. A thyroid uptake counter usually employs a single PMT for non-imaging applications.

In this chapter an overview of radiation detection using scintillators is presented along with a description of the thyroid uptake counter subject to the Monte Carlo simulations. The Monte Carlo model is detailed and validation is documented against practical measurements to determine the model's suitability for further investigation.

7.2 Radiation detection using scintillation detectors

The principle of radiation detection using a scintillation detector relies on the interaction of gamma and x radiation within the scintillation crystal. Scintillation crystals are generally hygroscopic and hence require the crystal and PMT to be sealed in an outer assembly to prevent any moisture ingress (Prekeges, 2011). The most commonly utilised scintillator crystal in nuclear medicine is NaI(Tl). At nuclear medicine diagnostic photon energy ranges, the predominant interaction between the

incident photon and NaI(Tl) is the photoelectric effect. Above these energies, Compton scattering predominates and the detection efficiency of NaI(Tl) begins to fall (Cherry et al., 2003). Incident photon energies greater than 1.02 MeV are required for pair production interactions, which falls outside the typical diagnostic nuclear medicine energy range.

These interactions will cause excitation of the electrons in the crystal and a subsequent release of optical photons when the electrons fall back to their lower energy levels, via a colour centre. The amount of light produced is proportional to the incident radiation and therefore energy discrimination is possible.

The NaI(Tl) crystal is coupled to a PMT which is designed to detect the light emitted as a result of radiation interactions within the crystal. Light from the crystal hits the photocathode and this results in the emission of photoelectrons via the photoelectric effect. These electrons are accelerated to a nearby dynode, which is held at a positive potential with respect to the photocathode. When the electrons strike the dynode at speed this causes the emission of more electrons. This continues for several dynodes until the final dynode in the chain (anode) where the current produced by the electrons passes out of the PMT. Typical electron gain factors for a PMT with nine to twelve dynodes would be of the order of one million (Prekeges, 2011). The voltage pulse is further subjected to electronic amplification and pulse shaping within the assembly electronics to produce a voltage pulse that is suitable for pulse height analysis.

In theory, a radioactive source that emits single energy photons should produce a single value of voltage pulse when detected by a scintillation detector. However, a spread of values will be observed because of the variations in the processes of photon conversion to an electrical pulse. These include inefficient conversion of the incident photon energy into light photons in the crystal, fluctuations in the high voltage applied to the PMT and electrical noise in the system electronics. When the distribution of pulse height values is plotted it will take the form of a Gaussian curve (Prekeges, 2011).

It is often beneficial to the operator to selectively count the radiation arising from a particular part of the displayed spectrum. This may be due to the fact that there are two or more radionuclides in a given sample or to count over the photopeak of the radionuclide to selectively remove Compton scatter regions (the Compton band is a separate feature of the spectrum due to the escape of the scattered photon and hence partial energy deposition). A voltage window can be selected to count only over a particular energy range of interest in the spectrum. This can be achieved because the electrical signal produced by the detector is proportional to the incident photon energy. The size of the detected signal is represented as a voltage level and a window can be placed around the central photopeak energy. Providing that the detector is calibrated against at least two known gamma energy sources it can also be used to measure photopeak energies.

7.3 Canberra detector system

The thyroid uptake detector system used for the investigations is the 802-2×2 detector manufactured by Canberra (Canberra, 2009). The detector system broadly consists of a scintillation crystal, a PMT, an internal magnetic light shield and a 14-pin connector. The 14-pin connector is connected to a pre-amplifier and is also supplied from an external high voltage power supply. The whole assembly is encased within aluminium housing. The scintillation detector is a hermetically sealed assembly which includes a 51 × 51 mm NaI(Tl) crystal. The detector is housed within a lead outer shield which also incorporates a removable diverging lead collimator (1 cm thick at the entrance). The inner diameter at the entrance of the collimator is 9 cm with an inner diameter of 5.3 cm to the face of the detector. The dimensions of the collimator are consistent with the IAEA recommendations for the calibration and standardisation of thyroid uptake measurements (IAEA, 1962). The shielded detector is attached to a Panax stand that allows manoeuvrability of the detector unit (Figure 7.1).

Figure 7.1: Picture of the Canberra detector system and Panax stand

7.3.1 Multichannel analyser

The high voltage to the PMT is supplied by a Canberra ASA-100 MCA module (Canberra, 2001). The MCA has 1024 channels to allow for energy discrimination. The high voltage, coarse gain and fine gain are set to determine the energy range and location of radionuclide peaks within the acquired spectra. The MCA is controlled using GENIE™ 2000 Gamma Acquisition and Analysis Version 3.1 software (Canberra, 2006). The MCA can be operated in time mode, where data is acquired for a pre-set time, or count mode, where data is acquired until a single channel or group of channels registers a pre-set number of counts.

7.3.2 Optimisation of acquisition parameters

Before using the Canberra system to acquire data, a process of optimisation is required to ensure that the system is correctly calibrated and set up prior to use. For ^{123}I, the upper and lower discriminator levels were set to 1.5% and 100% respectively. As the investigations include the analysis of the spectral x-ray emissions of ^{123}I, raising the lower discriminator level above 1.5% was not desirable. For routine clinical applications, it is customary to set the variables that affect the system gain, such as the applied PMT voltage and electronic amplification, to ensure that the principal gamma peak is in the middle of the spectral display. Replicating the clinical application is desirable in these investigations to determine some of the inherent sources of uncertainty in the uptake assessment. A summary of the parameters employed for the MCA can be seen in Table 7.1.

GENIE™ 2000 Menu Option	Parameter	Setting
ADC	Lower level discriminator	1.5%
	Upper level discriminator	100.0%
Channels	Channels	1024
Amp	Coarse gain	256×
	Fine gain	1.51×
	Input mode	Amplifier
HVPS	HV on	900V

Table 7.1: GENIE™ 2000 MCA parameters

7.3.3 GENIE™ 2000 software analysis tools

The GENIE™ 2000 software (Version 3.1) allows for ROIs to be selected on the displayed spectrum. For thyroid uptake assessments, a consistent selection of ROIs is required for the comparison of a spectrum from the patient to that of a radioactive standard. The GENIE software will allow auto-selection of ROIs based on Gaussian modelling of the gamma peaks. However, this has the potential to cause variable ROI selection depending on the shape of the gamma peak. Therefore for thyroid uptake counting, the ROI is predetermined with the same defined start and end points for both patient and phantom measurements.

An example of a screen capture of the GENIE™ 2000 user interface can be seen in Figure 7.2.

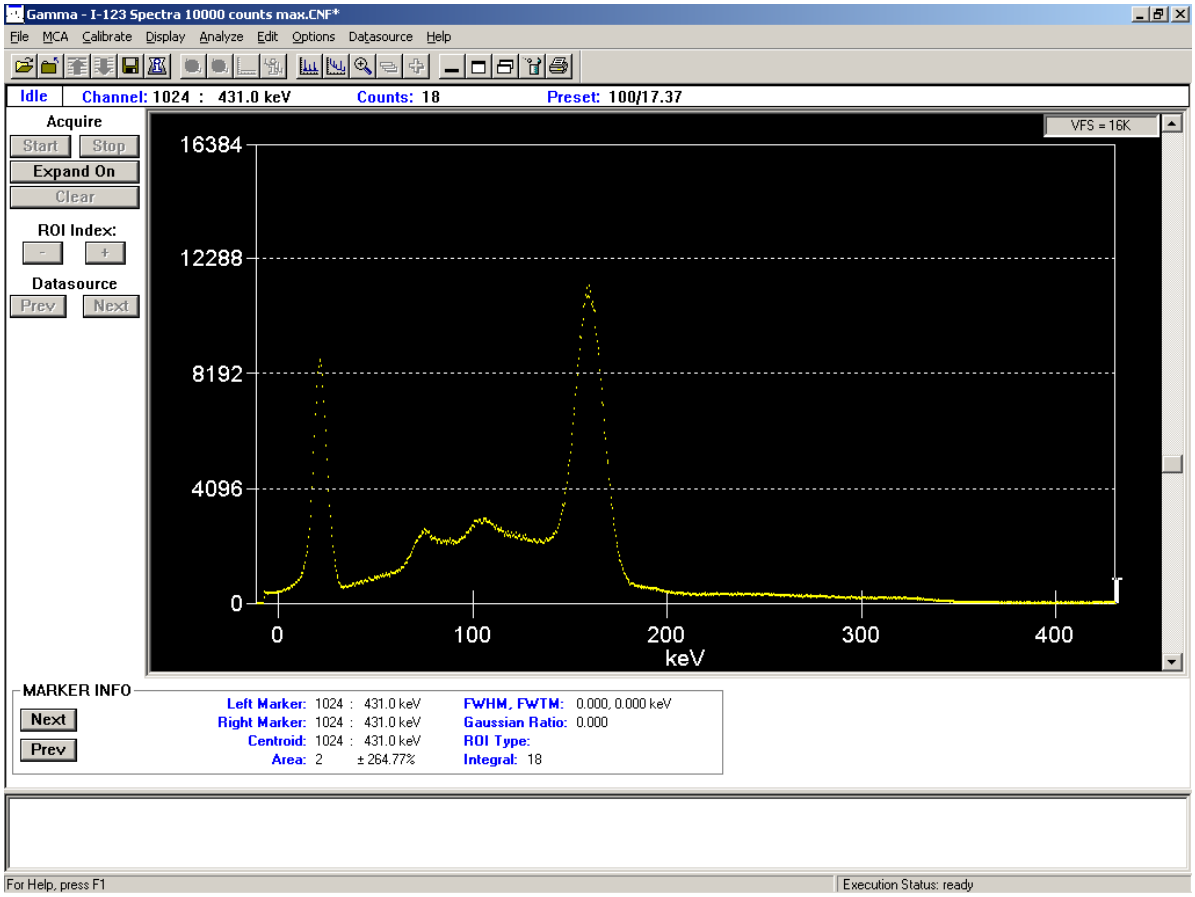

Figure 7.2: GENIE™ 2000 user interface showing a ^{123}I spectra

7.4 Energy Calibration

Energy discrimination is an inherent property of a scintillation detector system and is influenced by the high voltage, electronic gain and also the energy resolution of the system. An energy calibration must be undertaken to relate the energy of the photons detected by the system to a particular channel number. When un-calibrated, the x-axis of the spectrum displays channel numbers between 1 and 1024. As a minimum, at least two distinct incident gamma energies must be used to produce a calibration. However, it is preferable to use more than two energies to improve the accuracy of the calibration. The calibration order of fit can also be varied up to a maximum of a third order fit, dependant on the number of distinct calibration points

used. The GENIE™ 2000 software platform allows for a number of calibrations to be undertaken that can be saved as separate calibration files to be recalled at a later date. To ensure good concordance with the Monte Carlo simulation, it is therefore important that the calibration is accurate in this range.

7.4.1 Calibration of the Canberra system

The choice of radionuclides to use for calibration will depend on local availability and the intended use of the system. Generally, sealed radioactive sources are preferred to reduce any possible radioactive contamination. Radionuclides with longer half-lives are usually sealed to ensure they have a longer working use. For thyroid uptake assessments using ^{123}I, a calibration range of 0 - 320 keV would place the main gamma emission in the centre of the spectral display.

The radionuclides used for energy calibration were: ^{241}Am, ^{99m}Tc, ^{57}Co, and ^{123}I. ^{241}Am and ^{57}Co were sealed sources with activities in the kBq range. ^{99m}Tc and ^{123}I were unsealed and underwent a dilution process to reduce the activities to several kBq. The unsealed sources were secured in a plastic aliquot bottle. The principal emissions of each of these radionuclides have been documented previously in Table 4.7. These radionuclides are chosen specifically to span both the characteristic x-ray and the principal gamma emission. Initially, ^{241}Am and ^{57}Co were placed on the surface of the detector and an acquisition was undertaken for 30 minutes. A further two independent acquisitions were acquired using ^{57}Co and ^{123}I. Similar to the activity linearity issues that may be experienced with a radionuclide calibrator, scintillation detectors may suffer from dead time losses at high incident photon rates.

The Canberra detector does apply a counting time correction for dead time losses. However, the reported dead time was constrained to less than 5% in all calibration acquisitions.

A total of four calibrations were undertaken and as summarised in Table 7.2. The calibration equations for each of the four calibrations are shown in Table 7.3.

Radionuclide	3 Source, 1st Order	3 Source, 2nd Order	4 Source, 1st Order	4 Source, 2nd Order
^{241}Am	✓	✓	✓	✓
^{57}Co	✓	✓	✓	✓
^{99m}Tc	✓	✓	✓	✓
^{123}I	×	×	✓	✓

Table 7.2: Combination of radioactive sources used for each of the four calibrations

Calibration	Calibration Equation
3 Source, 1st Order	Energy = -7.55 + (0.4163×ChNumber)
3 Source 2nd Order	Energy = 4.364 + (0.3077×ChNumber) +(0.0002169×ChNumber^2)
4 Source 1st Order	Energy = -8.791 + (0.4232×ChNumber)
4 Source 2nd Order	Energy = 0.2049 + (0.346×ChNumber) + (0.0001392×ChNumber^2)

Table 7.3: Calibration best fit equations for each of the four calibrations

7.4.2 Calibrated ^{123}I spectra

Once the energy calibration has been undertaken and the calibration files generated, they can be recalled and applied to subsequent spectral acquisitions.

Figure 7.3 shows the ^{123}I spectrum used in the calibration with each of the different calibrations applied. The energy of the channel number corresponding to the peak x-ray and gamma positions are shown in Table 7.4 for each calibration.

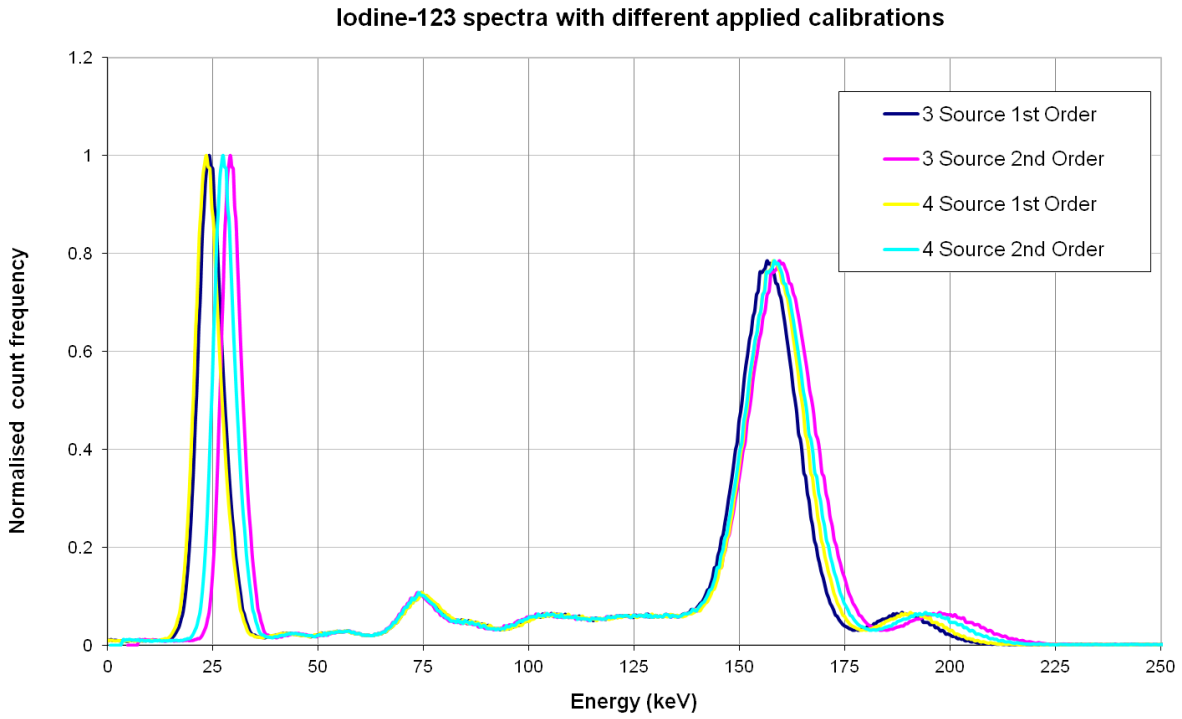

Figure 7.3: Graphical representation of the acquired ^{123}I spectra with the application of four different calibrations

Calibration	X-ray Peak keV	Gamma peak keV
3 Source, 1st Order	24.1	156.5
3 Source 2nd Order	29.0	159.7
4 Source 1st Order	23.4	158.4
4 Source 2nd Order	27.3	158.1

Table 7.4: X-ray and gamma peak energy for each calibration

7.4.3 Calibrated ^{123}I spectra discussion

Figure 7.3 demonstrates that there are differences in the positions of the x-ray and the gamma peaks when applying each of the calibrations to a acquired spectra. NaI(Tl) crystals demonstrate a non-linear energy response which is reflected in the observed spectra. The expectation is that the higher order calibrations will more accurately correlate to the Monte Carlo simulations because of the non-linear energy resolution of the crystal. This is indeed shown in Table 7.4. The average emission weighted energy of the x-rays is 28.1 keV and the principal gamma emission is 159 keV. The two second order calibrations appear to best match both the x-ray and gamma emissions of ^{123}I.

7.5 Energy Resolution

One of the main characteristics of the detector which is evident from Figure 7.3 is the broadening of the spectra peaks, commonly expressed as the energy resolution. An element of broadening would be expected for the x-ray peak due to the number of discrete emissions over a small energy range. However, the gamma peak is also broadened and the reasons for such broadening are discussed in section 7.2.

The energy resolution of the Canberra detector is an important parameter to characterise for subsequent Monte Carlo simulations. The energy resolution is typically expressed as:

$$\text{Energy Resolution} = \frac{\text{FWHM}}{\text{Photopeak Energy}} \quad \text{.....Equation 7.1}$$

Where the FHWM is the full width of the photopeak in keV at half the peak maximum count. The energy resolution is also commonly expressed as a percentage and is non-linear, typically decreasing at higher incident photon energies.

For the x-ray and gamma peaks in the ^{123}I spectrum, the FHWM can be calculated by fitting a Gaussian curve to the peak. The Gaussian curve distribution takes the form of:

$$G(x) = \frac{1}{\sigma\sqrt{2\pi}} e^{-\frac{(x-\mu)^2}{2\sigma^2}} \quad \text{...Equation 7.2}$$

Where σ is the standard deviation and μ is the mean value.

G(x) is a maximum when x = μ:

$$G(\mu) = \frac{1}{\sigma\sqrt{2\pi}}$$ ..Equation 7.3

Let half maximum x = x_H:

$$\frac{G(\mu)}{2} = \frac{1}{2\sigma\sqrt{2\pi}} = \frac{1}{\sigma\sqrt{2\pi}} e^{\frac{-(x_H-\mu)^2}{2\sigma^2}}$$ ...Equation 7.4

$$\frac{1}{2} = e^{-\frac{(x_H-\mu)^2}{2\sigma^2}}$$ ...Equation 7.5

$$In_e(2) = -\frac{(x_H-\mu)^2}{2\sigma^2}$$ ...Equation 7.6

$$x_H - \mu = \pm\sqrt{2\sigma^2 In_e(2)}$$ ...Equation 7.7

$$x_H = \pm\sigma\sqrt{2In_e(2)} + \mu$$ ...Equation 7.8

Therefore

$$FHWHM = 2\sqrt{2\sigma^2 In_e(2)} = 2\sigma\sqrt{2In_e(2)}$$ ...Equation 7.9

7.5.1 Assessment of Canberra energy resolution

To fully characterise the energy resolution of the Canberra system, spectral acquisitions of ^{123}I, ^{57}Co and ^{99m}Tc were undertaken. Each radionuclide spectrum was acquired with the source placed on the detector surface until at least 10,000 counts were acquired within the peak [10,000 counts yield an approximate 1% counting uncertainty within the peak].

The spectra were exported from the GENIE™ 2000 software and imported into Excel™ (Microsoft corp) for analysis. The solver function within Excel™ was utilised to fit a Gaussian curve to the peaks and calculate the standard deviation. Equations 7.9 and 7.1 were used to calculate the FWHM and energy resolution.

The FWHM and energy resolution results for each of the calibrations are shown in Table 7.5.

Radionuclide	FWHM (keV)	Energy resolution (%)
Three source 1st order		
^{123}I X-ray	6.93	24.69
^{57}Co	13.86	11.36
^{99m}Tc	14.81	10.58
^{123}I	16.43	10.34
Three source 2nd order		
^{123}I X-ray	5.73	20.41
^{57}Co	15.15	12.42
^{99m}Tc	16.38	11.70
^{123}I	18.50	11.64
Four source 1st order		
^{123}I X-ray	7.14	25.47
^{57}Co	14.53	11.91
^{99m}Tc	15.30	10.71
^{123}I	16.26	10.23
Four source 2nd order		
^{123}I X-ray	6.19	22.04
^{57}Co	14.81	12.14
^{99m}Tc	15.69	11.21
^{123}I	17.73	11.15

Table 7.5: FWHM values and energy resolutions for each radionuclide

The variation of percentage energy resolution with energy for each of the calibrations is shown in Figure 7.4. A polynomial quadratic equation has been fitted in Excel™ to each of the curves.

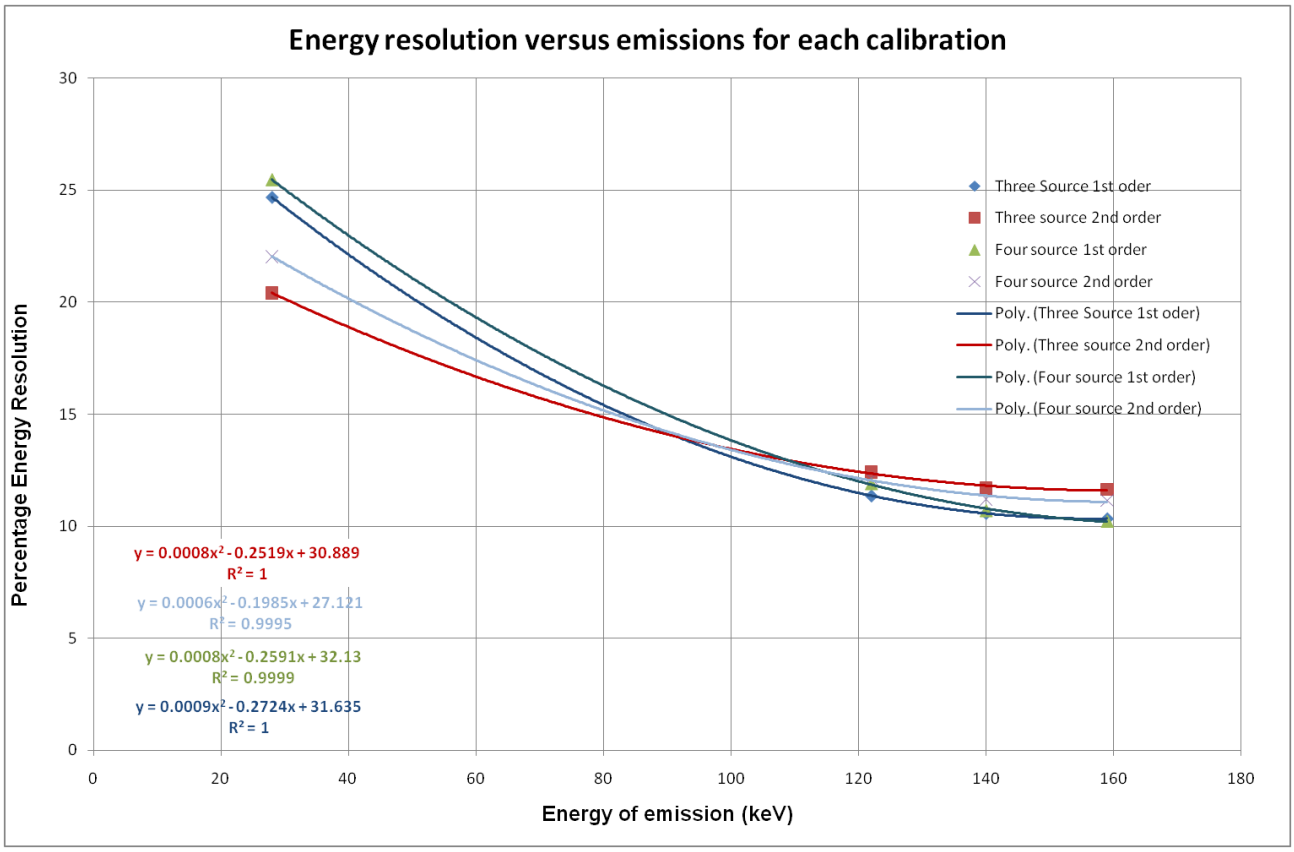

Figure 7.4: Energy resolution values as a function of emitted energy for each calibration

7.6 Monte Carlo model of the Canberra detector

Other authors (Dewji, 2009) (Davies, 2012) have produced MCNP models of the Canberra detector used in the following investigations. However, the MCNP model used for the simulations was produced, validated and investigated independently of previous work (unless otherwise stated). The dimensions and composition of the detector were obtained from published technical data (Canberra, 2011) and where such information was not available, direct measurements and/or estimations of the detector system were undertaken.

7.6.1 Geometrical structure of the Canberra detector

Similar to the modelling of the Fidelis calibrator in Chapter 4, the Canberra detector can be modelled as a series of cylindrical surfaces within the MCNP5 code. The NaI(Tl) crystal is 51 × 51 mm and is surrounded by a 1.6 mm thick aluminium oxide reflector. Behind the crystal is the PMT. All of the components are encased in aluminium and contained within a lead shield. The specifications of the collimator are detailed in chapter 7.2.

7.6.2 Material composition of the Canberra detector

The specifications of the materials can be found in Table 7.6. The PMT is modelled as a vacuum. Material compositions are given as a percentage by weight.

	Crystal	**Reflector**	**Casing**	**Lead casing**	**PMT**
Materials (% Split)	15% Sodium 85% Iodine	47% Oxygen 53% Aluminium	100% Aluminium	100% Lead	Vacuum
Density (g cm^{-3})	3.67	0.55[a]	2.7	11.35	-

Table 7.6 material composition of the Canberra detector

[a] density for the reflector taken from Dewji (2009).

7.6.3 Input file

The cell and surface cards for the Canberra detector model are shown below. A new macro body is introduced into the model, namely a Truncated Right-angle Cone and is described as:

TRC v_x v_y v_z h_x h_y h_z R_{base} R_{top}

where R_{base} is the radius of the base and R_{top} is the radius of the top of the cone. The other surface macro bodies are as previously described.

```
1  3 -2.7 -1 3 14                                  imp:p=1 $Al casing for crystal
2  2 -0.0012 -2 #1 #3 #4 #6 #7 #13 #14 #15         imp:p=1 $Universe of air
3  1 -3.67 -3                                      imp:p=1 $NaI Crystal
4  4 -11.35 -4 5                                   imp:p=1 $Lead collimator
6  4 -11.35 -6 1 3 7 8 13 14 15                    imp:p=1 $Lead casing of detector
7  0 -7                                            imp:p=1 $vacuum PMT Tube
8  0 2                                             imp:p=0 $Outside World
13 5 -1 -12                                        imp:p=1 $Water aliquot
14 7 -0.55 -14 3                                   imp:p=1 $Al oxide reflector
15 3 -2.7 -15 7 3 14 1                             imp:p=1 $Al casing for PMT

c Surface Cards
1  rcc 0 0 2.5 0 0 -5.31 2.76                      $Al casing for NaI
2  so 50                                           $Universe
3  rcc 0 0 2.55 0 0 -5.1 2.55                      $NaI Crystal
4  rcc 0 0 -4.81 0 0 -20.81 5.5                    $Collimator
5  trc 0 0 -4.81 0 0 -20.81 2.65 4.5               $collimator top
6  rcc 0 0 -4.81 0 0 22.07 5.25                    $Casing
7  rcc 0 0 2.55 0 0 14.66 2.835                    $PMT
8  rcc 0 0 -2.6 0 0 -2 2.885                       $gap at bottom of collimator
13 rcc 0 0 2.50 0 0 -7.31 2.885                    $air gap
14 rcc 0 0 2.55 0 0 -5.26 2.71                     $Al Oxide reflector
15 rcc 0 0 2.5 0 0 14.76 2.885                     $Al casing PMT
```

A cross-sectional visualisation of the Canberra detector is shown in Figure 7.5.

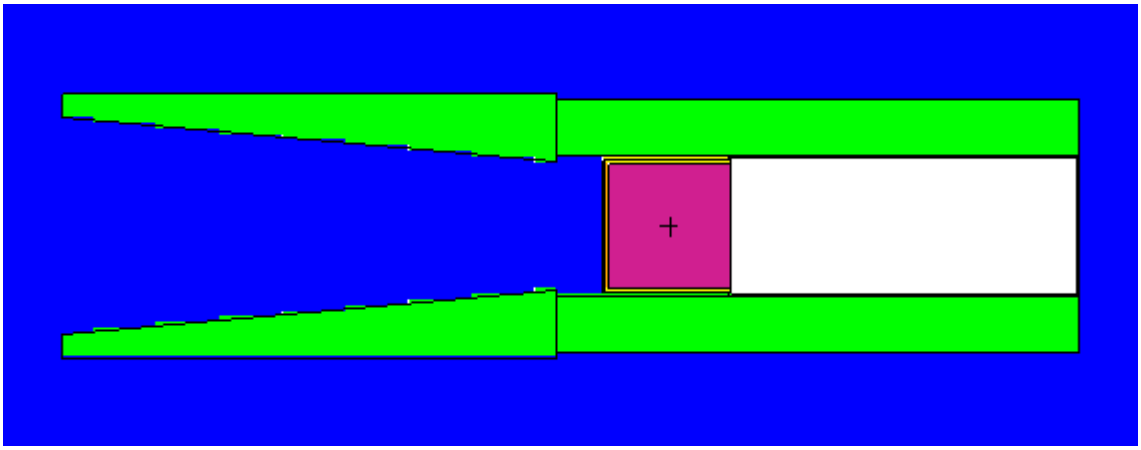

Figure 7.5: Cross-sectional visualisation of the Canberra detector

Figure 7.6 shows a 3D visualisation of the NaI(Tl) crystal and PMT with the aluminium case. Here the white tube is representative of the PMT and the blue region for the crystal.

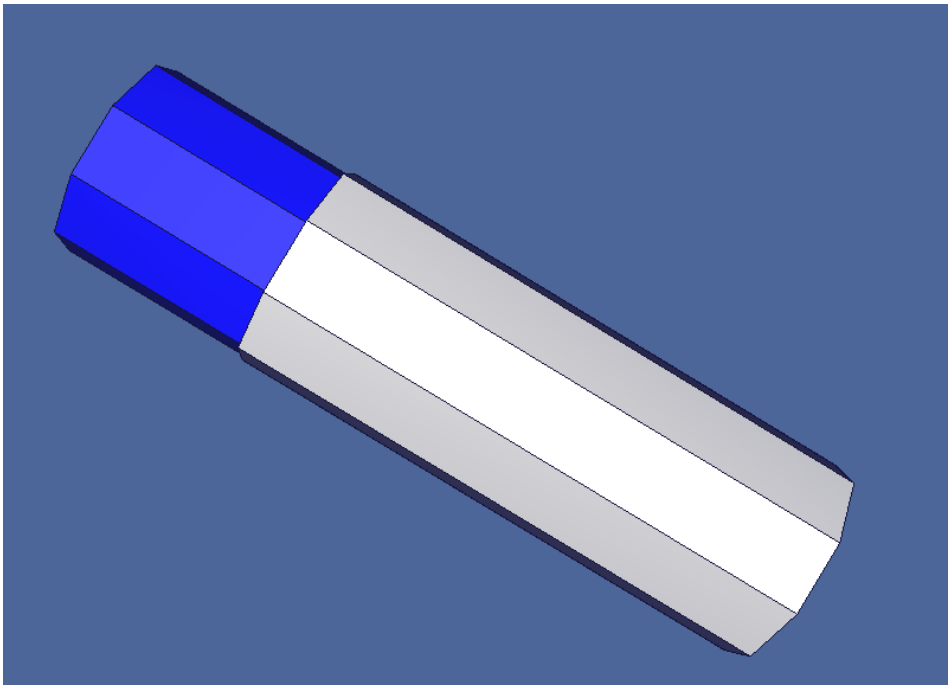

Figure 7.6: Canberra detector in the aluminium casing

Figure 7.7 shows the location of the collimator with respect to the detector. The base of the collimator sits 2 cm in front of the surface of the detector. An aerial view of the collimator towards the detector shows the convergent nature of the collimator (Figure 7.8).

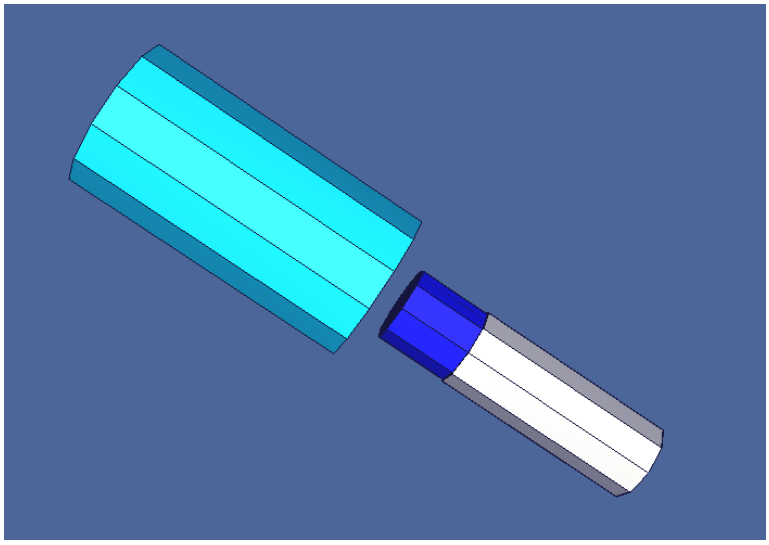

Figure 7.7: Canberra detector in the casing along with the collimator

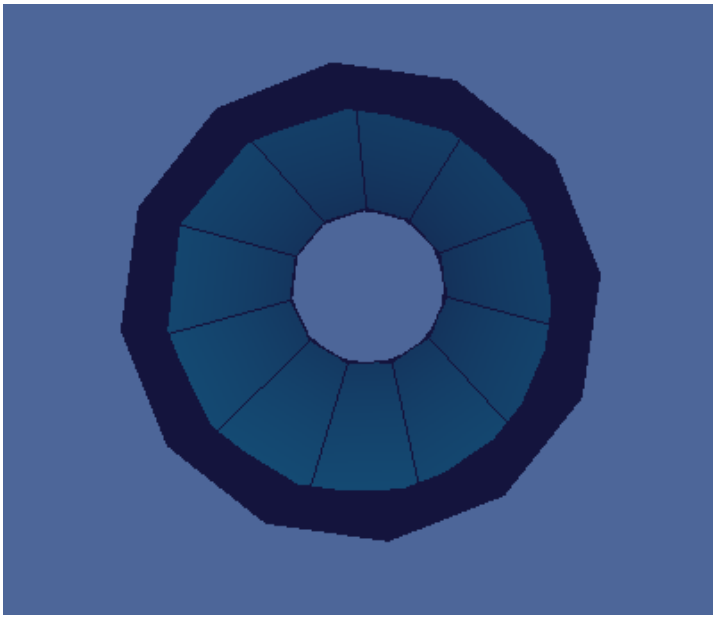

Figure 7.8: Aerial view of the collimator looking towards the detector. This shows the converging nature of the collimator from entrance to crystal face

Figure 7.9 shows the encapsulation of the detector in the lead casing against the collimator.

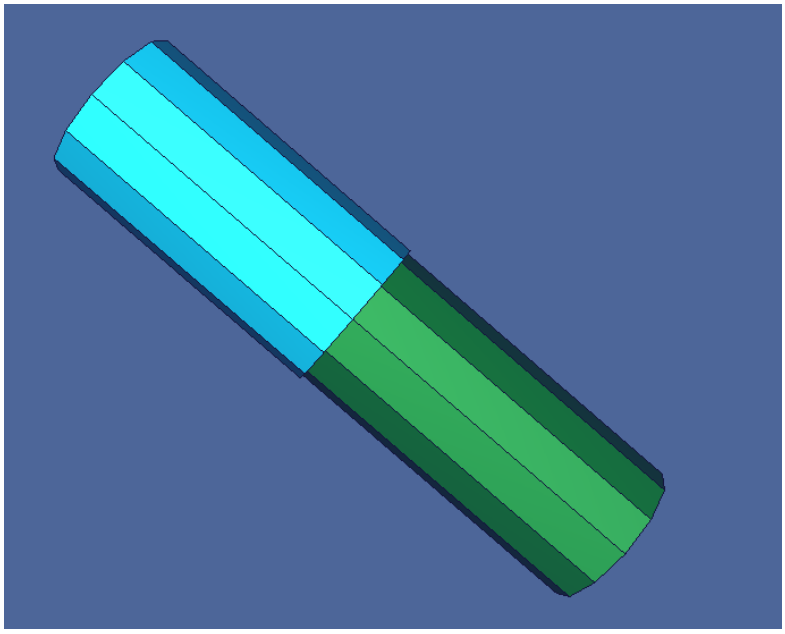

Figure 7.9: Encapsulation of the detector in the lead shield along with the connection with the collimator

7.6.4 Gaussian energy broadening

As previously described, in an imperfect detector there will be broadening of the spectral peaks. Previous work was undertaken in section 7.5 to characterise the relationship between the FWHM and the energy of the incident photons. For accurate Monte Carlo modelling, the relationship between the FWHM and incident energy must be incorporated into the model.

The Gaussian energy broadening function is described in the MCNP5 manual (X-5 Monte Carlo Team, 2003). The tallied energy is broadened by sampling from the Gaussian:

$$f(E) = Ce - \left(\frac{E-E_0}{A}\right)^2 \text{...Equation 7.10}$$

where *E* is the broadened energy, E_0 is the un-broadened energy of the tally, *Ce* is a normalisation constant and *A* is the Gaussian width.

The Gaussian width is related to the full width half maximum (FWHM) by:

$$A = \frac{FHWM}{2\sqrt{\ln(2)}} \text{ ... Equation 7.11}$$

The FWHM is specified by the user by providing the constants a, b and c to fit the following relationship:

$$FHWM = a + b\sqrt{E + cE^2} \text{...Equation 7.12}$$

The estimation of the constants was undertaken on the ^{123}I, ^{57}Co and ^{99m}Tc spectral acquisitions described in section 7.5.1. An initial estimation for each constant was made to match as closely as possible the calculated FWHM from Equation 7.9 to that specified in Table 7.5. The square of the difference between the measured FWHM and that calculated from Equation 7.9 was also calculated. The solver function in Excel™ was used to minimise the square of the differences through an

iterative process of adjusting values of the constants. This continued until the change in the values was negligible.

The constants calculated for each of the calibrations are shown in Table 7.7. A graphical representation of the Gaussian fits is shown in Figure 7.10.

	a	b	c
3 Source, 1st Order	0.00091	0.03543	0.93948
3 Source 2nd Order	-0.00082	0.03693	4.27358
4 Source 1st Order	0.00109	0.03568	0.93946
4 Source 2nd Order	-0.00116	0.04325	0.94004

Table 7.7: Monte Carlo Gaussian energy broadening coefficients

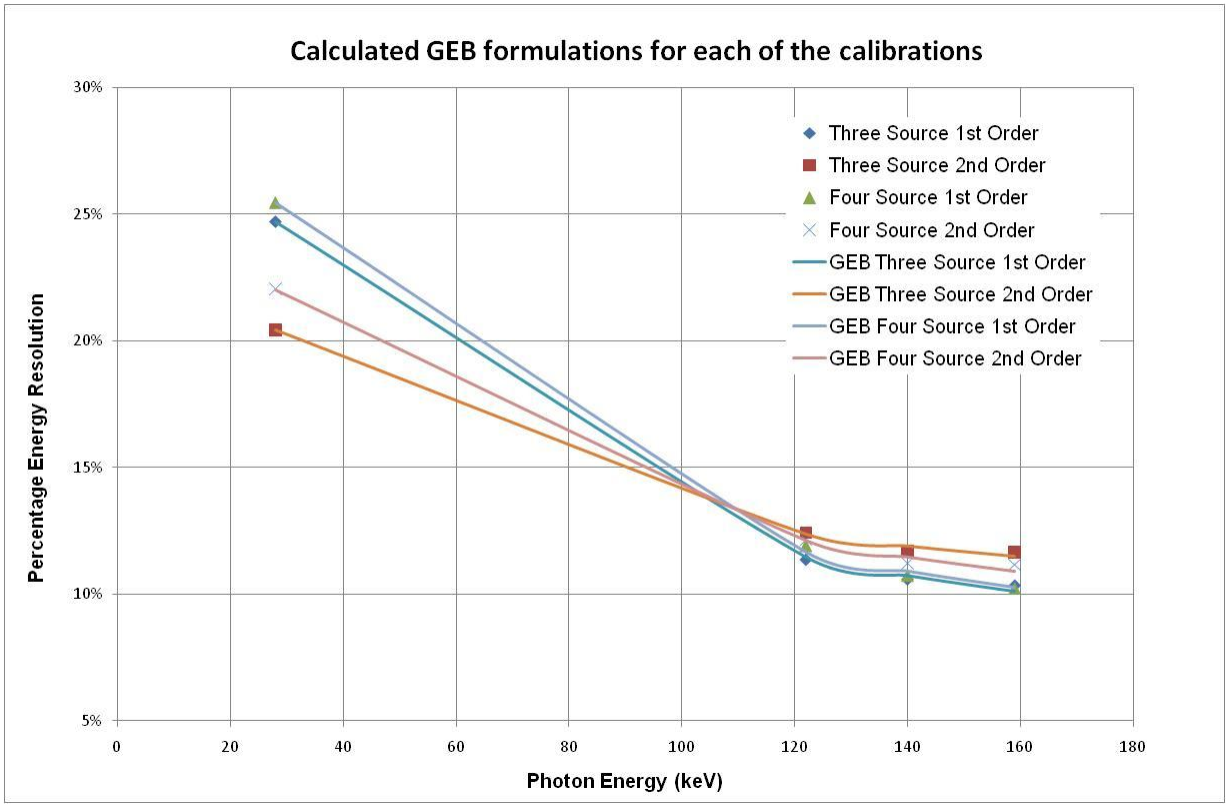

Figure 7.10: Calculated Gaussian energy broadening response for each of the calibrations

7.6.5 Tally card

The tally card used in the simulations is different to that previously used for the Fidelis calibrator simulations.

```
f8:p 3
ft8 GEB -0.00082 0.03693 4.27358
# e8
0
1E-5
0.00467
0.00498
0.00529
0.00560
.......
```

F8 is the pulse height tally specification in MCNP5 and details the normalised number of particles within a particular energy bin per starting particle. As previously described, the tally can be modified by a Gaussian energy broadening function, with the coefficients entered on the next line. In this case, the coefficients corresponding to the three source second order calibration were entered. The next line details the energy binning for the tally to apply. All 1024 energy channels are specified unless the calibration has resulted in negative energies. In this case only the positive energy bins are stated.

7.7 Monte Carlo model validation

A number of investigations were carried out to validate the Monte Carlo model against physical measurements undertaken on the Canberra system. The first assessment undertaken was to determine the most appropriate energy calibration to continue with further investigations.

7.7.1 Monte Carlo calibration modelling

The effect of different calibrations on the apparent central energies of the spectral peaks has been previously documented. The most appropriate energy calibration must be selected for the Monte Carlo simulations to give the best concordance between the Canberra detector and the model.

To determine the most appropriate calibration, an aliquot of ^{123}I was placed on the surface of the Canberra detector. The aliquot was placed directly on the surface of the detector to minimise scatter within the displayed spectrum. A spectrum of the ^{123}I aliquot was acquired until 10,000 counts had been tallied in a single channel.

To remove any uncertainties about source material composition in the Monte Carlo model, initial simulations were undertaken using a radionuclide solution without a container. The aliquot was therefore water based and suspended 0.1 mm above the surface of the detector.

A cross-section of the Monte Carlo model can be seen in Figure 7.11.

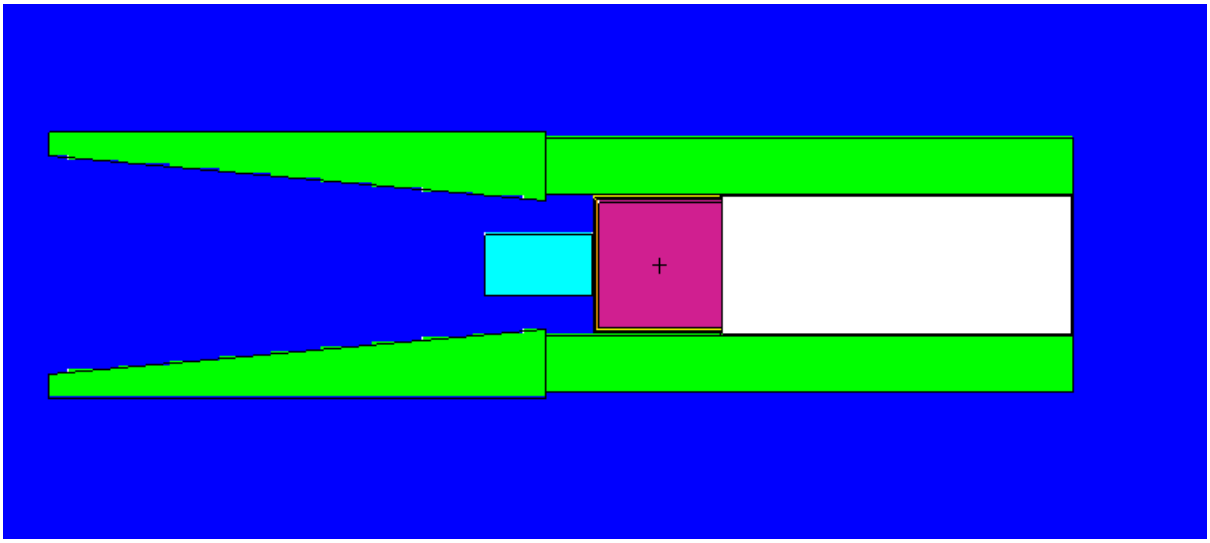

Figure 7.11: Water aliquot of ^{123}I suspended 0.1 mm from the front surface of the detector

A total of 1×10^{8} ^{123}I histories were simulated. A high number of particles were simulated in this instance to improve the statistical significance of each energy tally bin (considering there are 1024 independent channels).

Figure 7.12 shows the Vised visualisation of 10000 particles simulated from the radionuclide solution and the collision points.

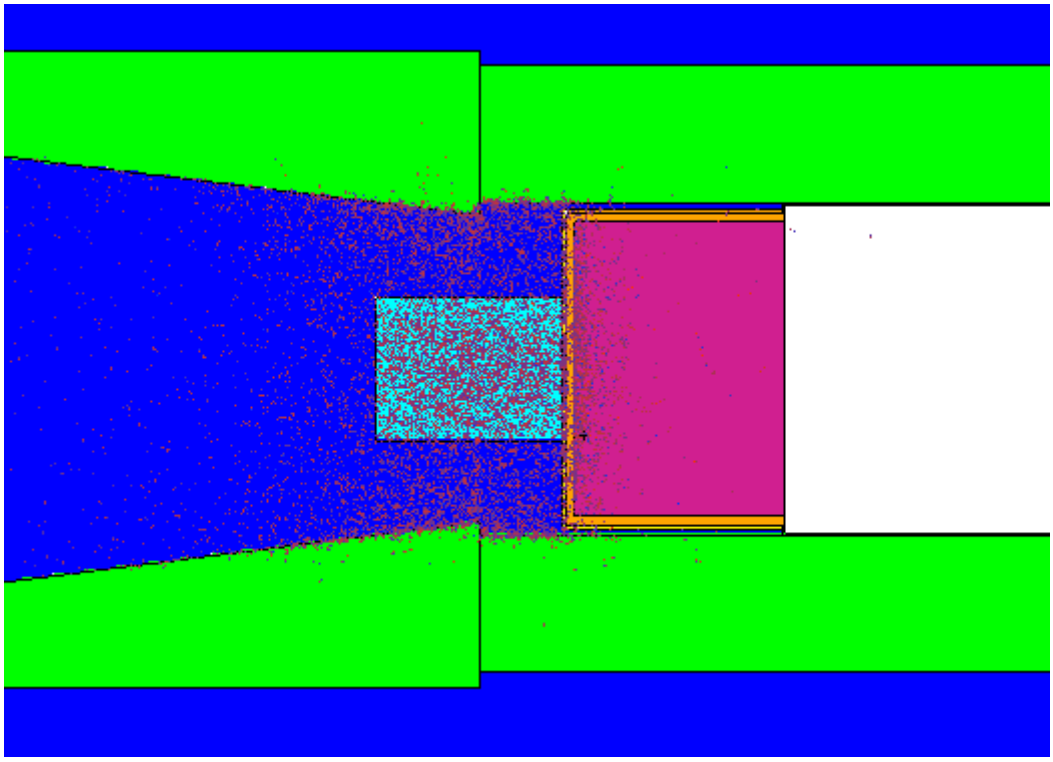

Figure 7.12: Vised visualisation of the collision points for 10000 particles simulated

The spectral display of the Monte Carlo simulations for each calibration as compared to the real ^{123}I acquisitions can be seen in Figures 7.13 - 7.16. Each spectrum has been normalised to the maximum value (counts or pulses) which in this instance occurs within the x-ray peak.

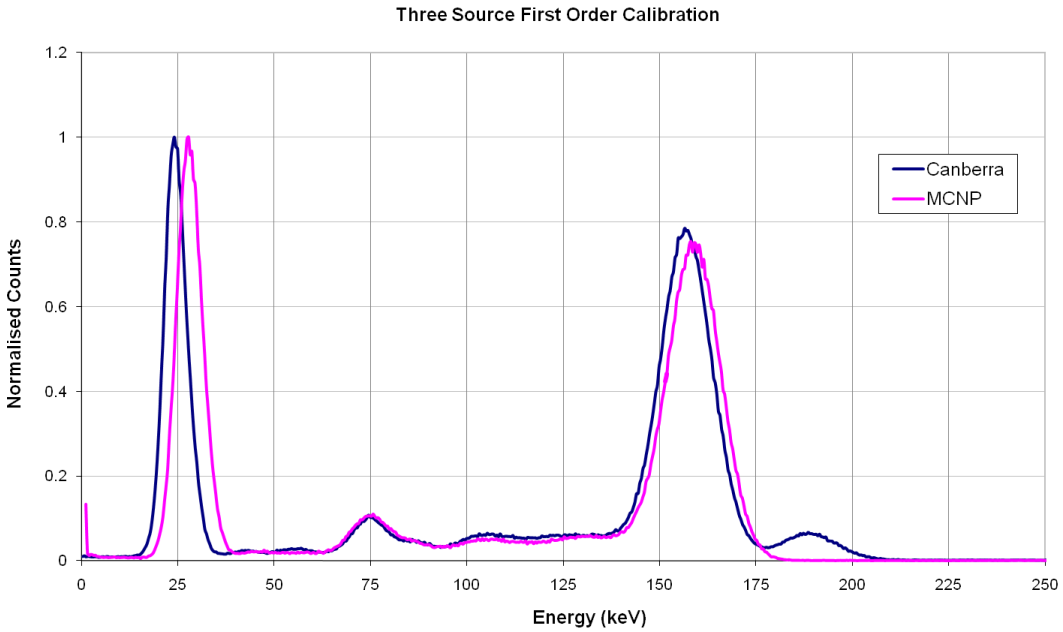

Figure 7.13: Three source first order comparison of the Monte Carlo and Canberra spectra

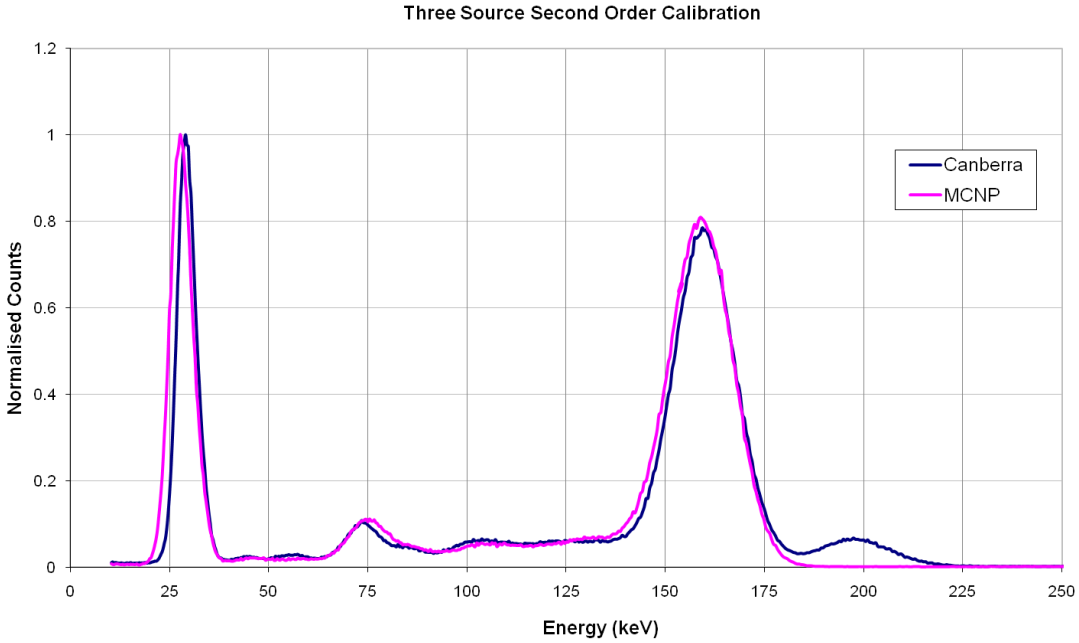

Figure 7.14: Three source second order comparison of the Monte Carlo and Canberra spectra

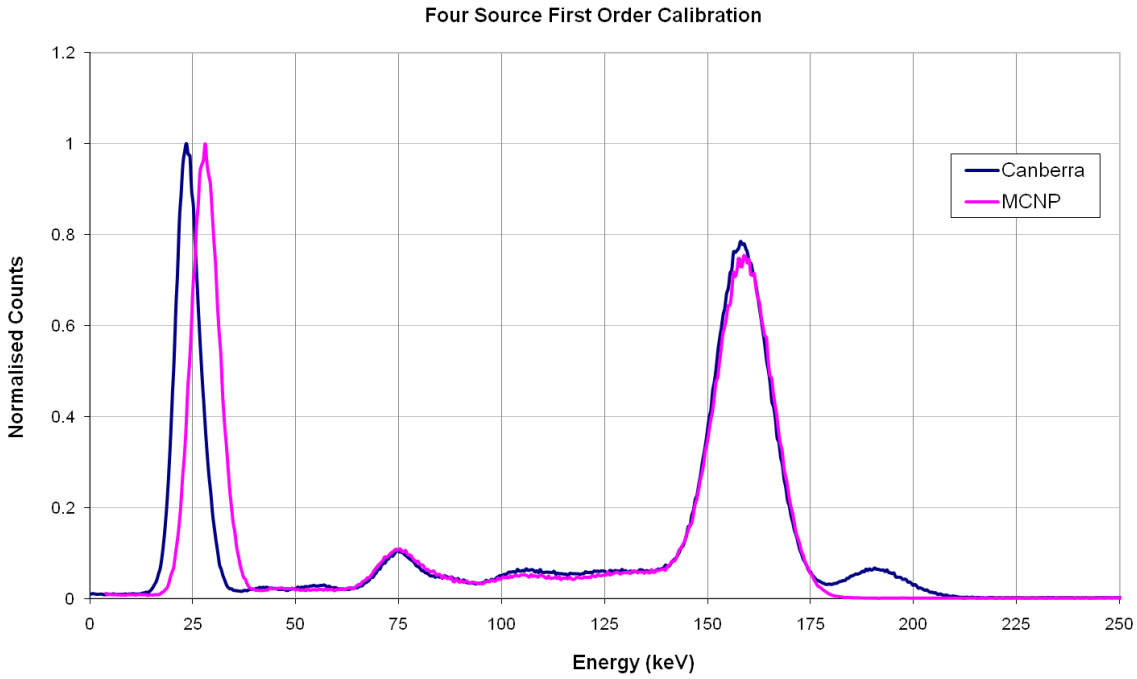

Figure 7.15: Four source first order comparison of the Monte Carlo and Canberra spectra

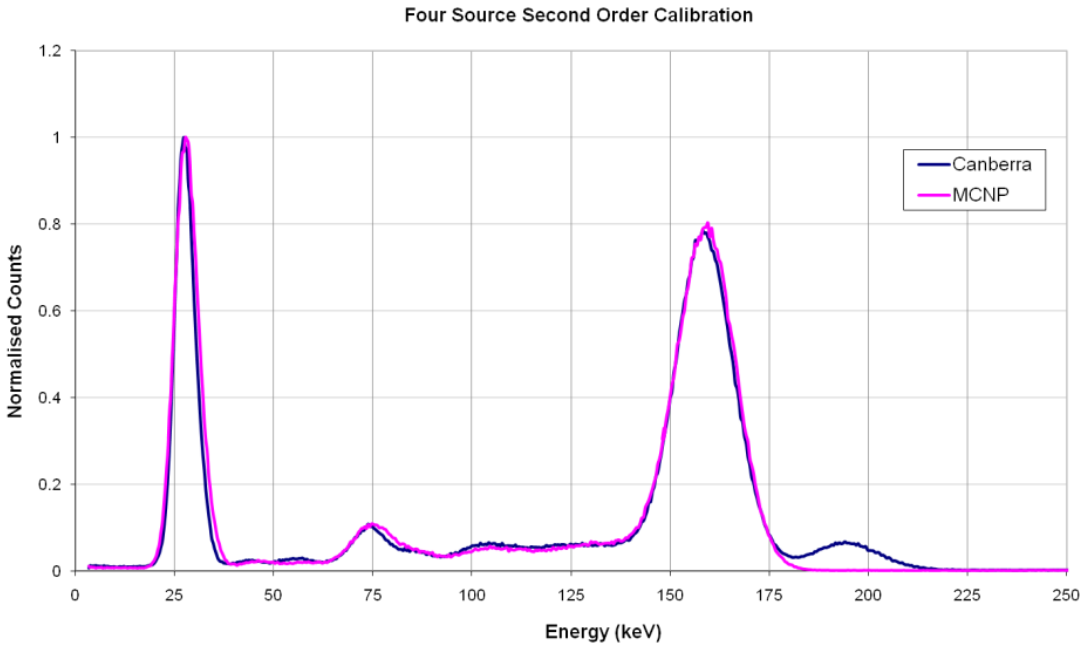

Figure 7.16: Four source second order comparison of the Monte Carlo and Canberra spectra

7.7.2 Discussion

Each of the four simulated curves shows similar spectral characteristics to the Canberra system. Both the x-ray and principal gamma peaks are identifiable on the Monte Carlo simulations. In each case, the degree of modelled spectral broadening appears to be in keeping with the physical system characteristics.

A peak at 75 keV is also apparent in the Monte Carlo and Canberra spectra. This is due to K-alpha (L-shell transition) emissions from lead. A single peak is noted which is the combination of 72 keV and 75 keV emissions.

Each of the Canberra spectra are also characterised by a peak at approximately 185 keV, which is not replicated on the Monte Carlo modelled spectra. This peak is likely due to the summation of the 159 keV gamma peak and the average x-ray emissions. Emissions from the ^{123}I source have resulted in both a characteristic x-ray emission and the principal gamma emission being detected by the Canberra system at the same time. This has therefore resulted in a count being registered for the combined energy of the characteristic x-ray and the principal gamma emission, at approximately 185 keV. As the Monte Carlo code simulates particle histories sequentially, this summation peak will not be observed in the modelled spectra.

It is obvious from the two first order calibrations that there is a discrepancy with the peak location of the x-ray between the modelled and Canberra spectra. Visual inspection of each of the models implies that the four source 2nd order calibration curve and Gaussian energy broadening coefficients are the most appropriate in

terms of accurately representing the physical geometries. To confirm this, the square of the differences between the Monte Carlo model and the Canberra was calculated for two regions corresponding to channels 56 – 109 for the x-ray peak and channels 353 – 448 for the principal gamma peak. The results are summarised in Table 7.8.

Calibration	X-ray peak (56 – 109 ch)	Gamma Peak (353 – 448 ch)
3 Source, 1st Order	7.10	0.71
3 Source 2nd Order	2.05	0.16
4 Source 1st Order	9.11	0.07
4 Source 2nd Order	0.33	0.05

Table 7.8: Sum squares of the difference between the x-ray and gamma peaks for the Monte Carlo models and Canberra system. The lower the value indicates the best concordance between the two spectra

It can be seen from Table 7.8 that the four source 2nd order fit provides the closest resemblance to the physical detector for this particular geometry. The Gaussian energy broadening coefficients and calibration for the four source 2nd order fit was therefore used for the subsequent validation modelling.

7.7.3 Thyroid neck phantom model

The next simulation undertaken was to see if the model could accurately reproduce the physical system when a scattering medium is simulated.

The thyroid uptake neck phantom used for clinical patient measurements was used for this assessment. The neck phantom is 15 cm long and has a radius of 15.4 cm. The centre of the aliquot is at a depth of 2.25 cm in the neck phantom with 0.8 cm of phantom material directly above the aliquot. As per routine protocol, the phantom is placed at 10 cm from the front of the collimator.

The exact material composition of the phantom was not known and therefore two simulations were undertaken, one with the phantom material consisting of PMMA and one with polyethylene. The density of PMMA was 1.19 g cm^{-3} and that of 0.96 polyethylene was g cm^{-3}.

Figure 7.17 shows a picture of the phantom located below the collimator.

Figure 7.17: Thyroid neck phantom located below the Canberra detector

Figure 7.18 shows a Vised visualisation of the cross-section Monte Carlo geometry. A 3D visualisation of the same geometry can be seen in Figure 7.19.

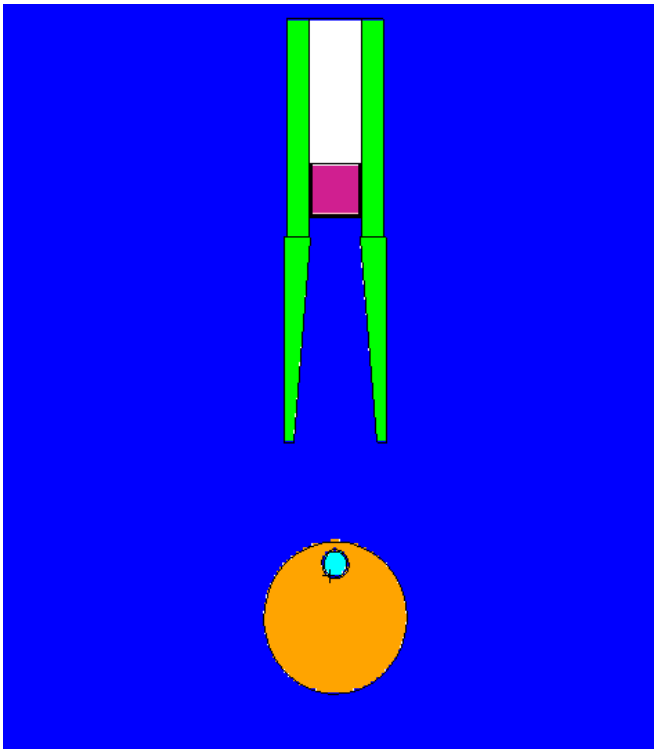

Figure 7.18: Cross-sectional thyroid neck phantom located below the Canberra detector

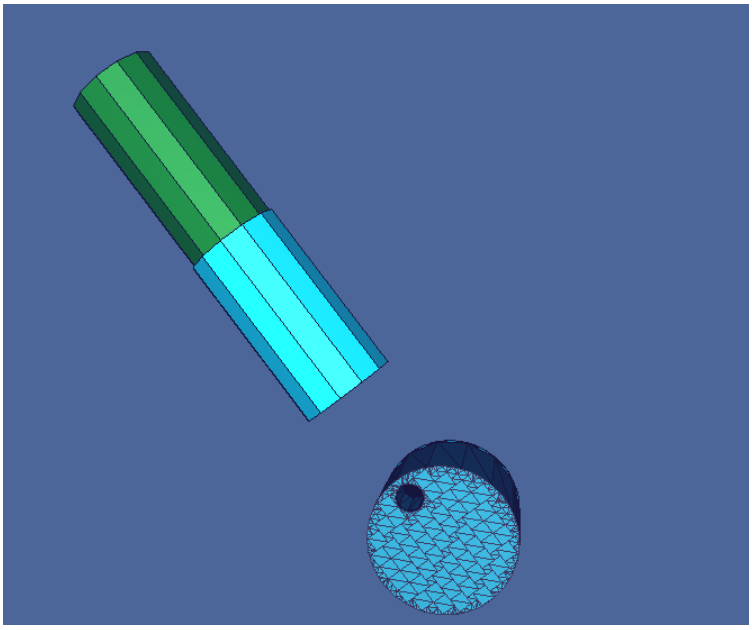

Figure 7.19: 3D visualisation of the thyroid neck phantom located below the Canberra detector

The comparison of the Monte Carlo spectrum and that of the Canberra system for the defined geometry can be seen in Figure 7.20. In this instance normalisation is made to the main gamma peak.

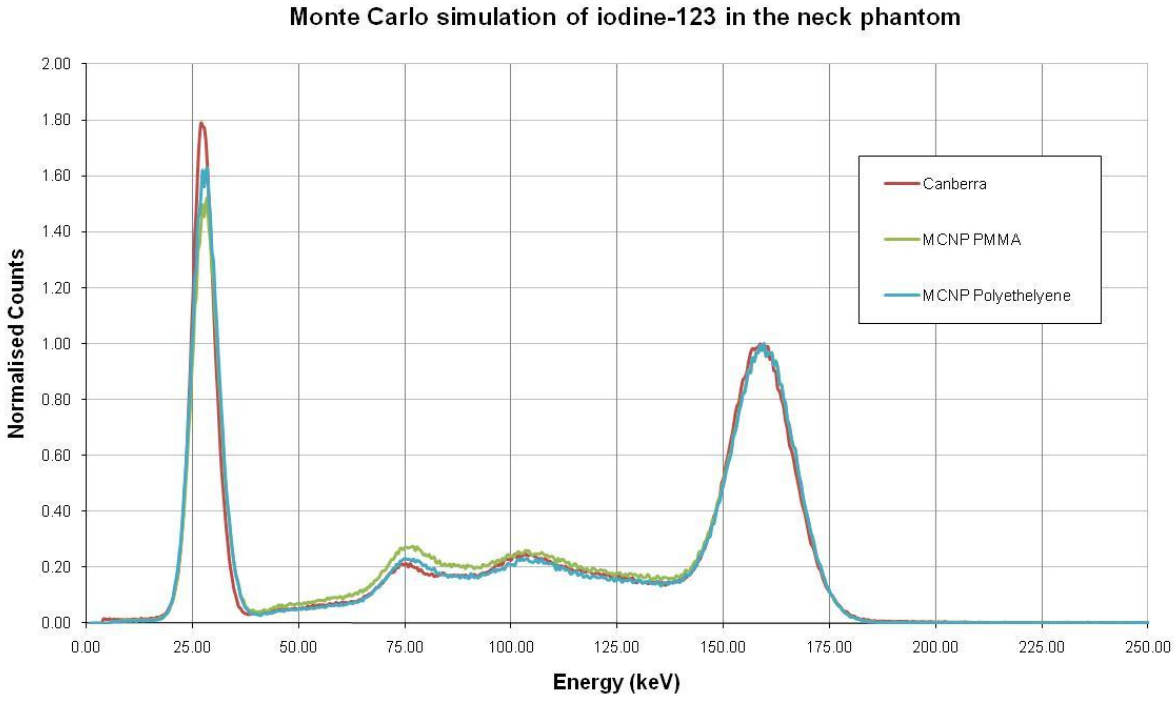

Figure 7.20: Comparison of Monte Carlo simulation and Canberra system for a ^{123}I aliquot within the neck phantom 10cm from the front of the collimator

7.7.4 Discussion

There are a number of spectral differences that can be seen in Figure 7.20 when compared to Figure 7.16. Firstly, a higher degree of Compton scatter can be observed in the region between the two peaks. The relative difference between the height of the x-ray peak and the gamma peak is also more pronounced for the phantom measurements.

Between the PMMA and polyethylene models, there are slight differences as would be expected from different material composition and density. The normalised peak

height of the PMMA model is slightly below that of the polyethylene, a reflection of the increased density of the composition modelled.

There is a discrepancy for the Monte Carlo model x-ray energies reported. There is approximately a 1 keV difference between the peak Monte Carlo x-ray and the Canberra x-ray.

The main difference between the Monte Carlo simulations and the Canberra system is the relative heights of the x-ray and main gamma peaks. In this case, the normalisation is done to the main gamma peak and therefore the discrepancy is seen at the x-ray peaks. The reverse would be true if the normalisation was undertaken to the x-ray peaks.

The relative difference in height between the peaks is likely to be due to the composition of the materials used or the geometry considerations of the thyroid neck phantom. Such a discrepancy was not observed for the simulation of the ^{123}I source near the detector surface. The relative counts (proportional to height) of the peaks is subject to the modelling in chapter 8 and therefore warrants further validation work to ensure a consistent response between the model and Canberra system.

Validation was undertaken for three different situations involving a point source in air, a point source behind PMMA at the collimator surface and a source dispersed in water bottle. As in the previous work, all practical and simulated measurements were undertaken with ^{123}I. The validation was undertaken in a similar fashion to that

described by Scarboro et al. (2009) where count ratios were calculated for the same energy regions in the MCNP5 modelled spectra.

7.7.5 Point source in air

The point source in air model is designed to assess the relative peaks of the ^{123}I spectra without the uncertainty introduced by additional materials.

The ^{123}I radionuclide solution consisted of a syringe with an active cylindrical dimension of 0.3 cm length and 0.23 cm radius. Encapsulation of the source within the syringe was modelled.

Practical measurements were undertaken with the point source centred in the view of the detector at a number of distances between 1 cm and 50 cm in air in front of the collimator.

The geometries were replicated in MCNP5 and a total of 1×10^{8} photons were simulated for each distance.

7.7.6 Point source in air results

A comparison of the Monte Carlo modelled and physical spectra for the case of the point source 5 cm in front of the collimator is shown in Figure 7.21.

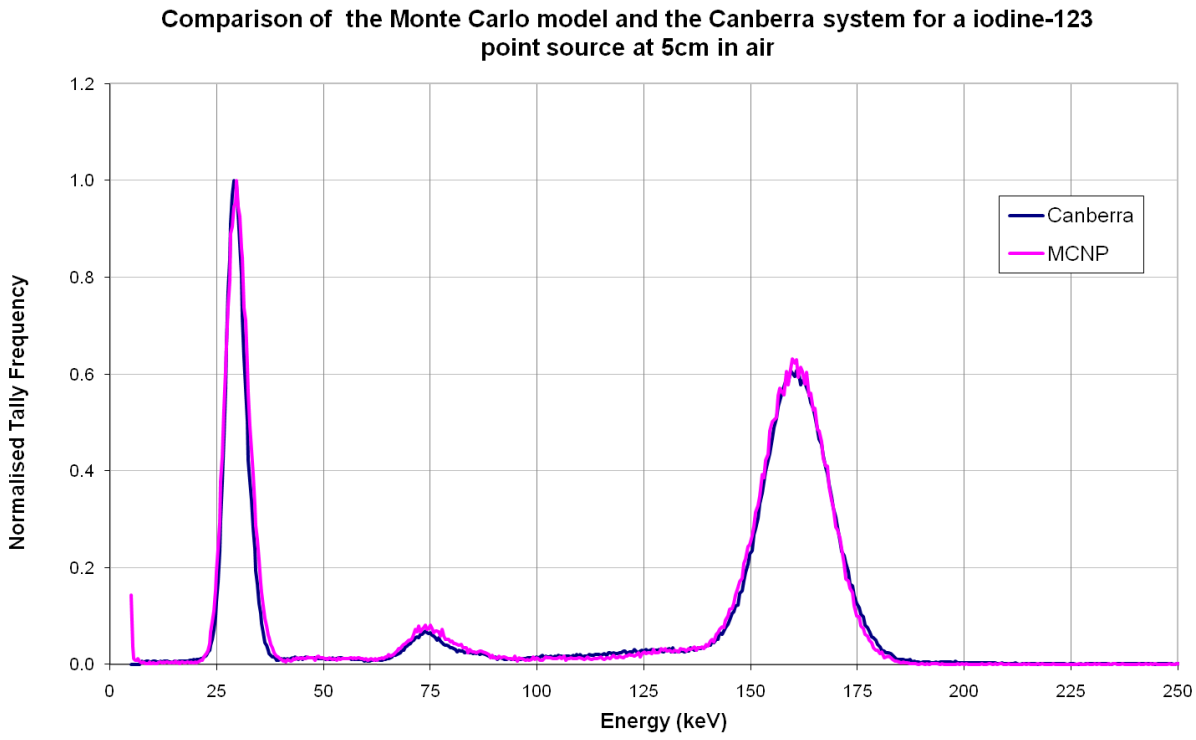

Figure 7.21: Comparison of the Monte Carlo model to the Canberra

Figure 7.21 shows a good concordance in both the energy and x-ray and gamma peak heights for the Monte Carlo and Canberra assessments. This is in keeping with the assessments undertaken with the ^{123}I source on the surface of the detector and shows point sources outside of the collimator can be modelled faithfully.

All of the spectral assessments to date have been normalised to either the x-ray or gamma peak. However, as the Monte Carlo model reports the number of pulses deposited in the energy bin per starting particle, these values can be converted to

counts with the appropriate multiplication of the activity of the source, the total acquisition time and the emissions per disintegration.

Before undertaking each of the measurements, the activity of the ^{123}I source was assayed in a Capintec-CRC15R calibrator using a copper filter with the previously derived copper filter factor of 54. For the case of the ^{123}I point source in 5 cm air, the activity of the source at the start time was 2.98 MBq. The acquisition was undertaken for 50 seconds and the number of emissions per disintegration for ^{123}I is 1.72.

The application of these correction factors to the raw Monte Carlo tallies is shown in Figure 7.22.

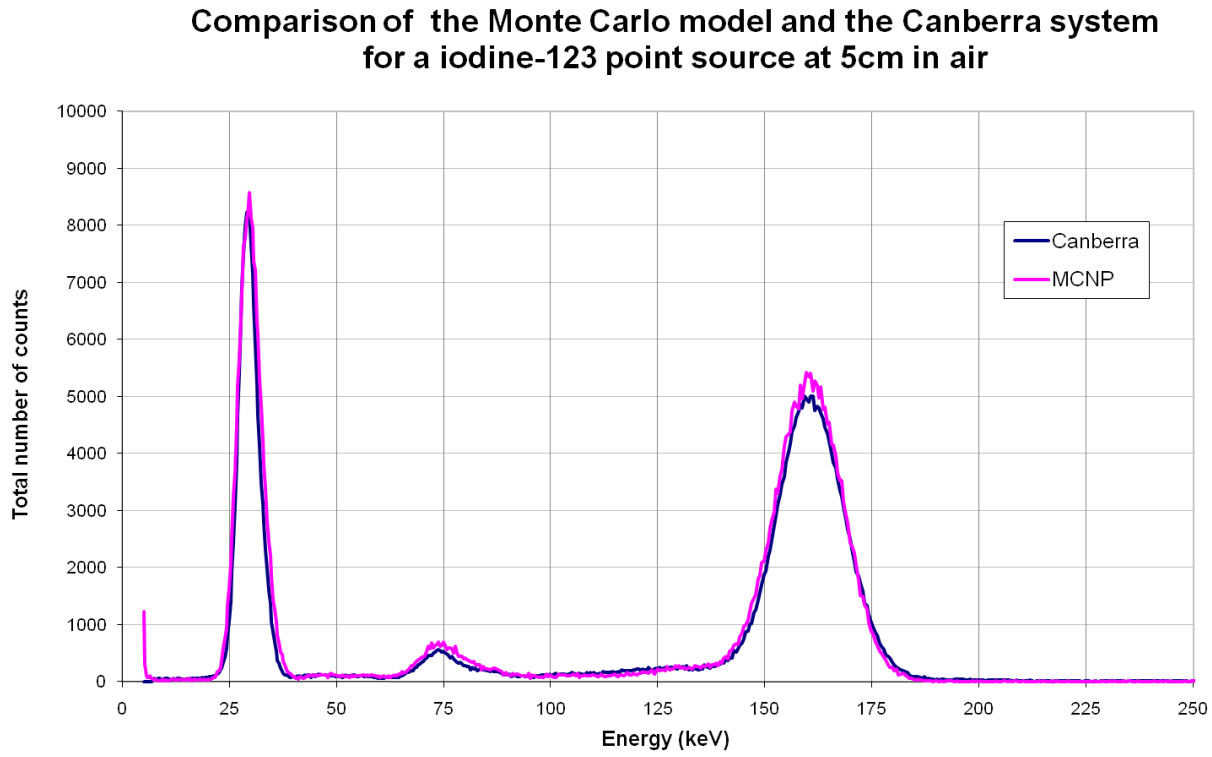

Figure 7.22: Comparison of the Monte Carlo model to the Canberra for total counts

Figure 7.22 shows a good concordance when the total number of counts is plotted for the Monte Carlo model and Canberra system. As the emission probability of ^{123}I and the time of acquisition are well know, the main factor influencing the conversion to counts is the accurate activity determination of the source. Figure 7.22 therefore appears to validate the use of a copper filter with the appropriate calibration factor as an accurate tool for measuring ^{123}I activity.

To determine the relationship between the relative counts in the x-ray peak and the main gamma peak, for each acquisition, the ratio of the Monte Carlo normalised counts to the Canberra normalised counts was plotted at each distance for the x-ray and gamma peak. Normalised counts were used to negate the potential effects of dead time. Fixed ROIs for the entire normalised peaks were used (channels 48 – 109 x-rays; 354 – 427 gamma). Table 7.9 shows the normalised ratios for the point source in air at each distance for the x-ray and gamma peaks.

Distance (cm)	X-ray peak ratio	Gamma peak ratio
1	0.915	0.994
5	0.889	0.969
10	0.877	0.955
15	0.890	0.973
20	0.904	0.983
25	0.900	0.979
30	0.902	0.988
35	0.896	0.973
40	0.901	0.992
45	0.915	0.999
50	0.903	0.991
Mean	0.899	0.982
3 × standard deviation	0.034	0.039

Table 7.9: Ratio of the Monte Carlo and Canberra x-ray and gamma peak for various distances in air

Figures 7.23 and 7.24 show a graphical representation of the data presented in Table 7.9. Error bars indicate three standard deviations of the mean.

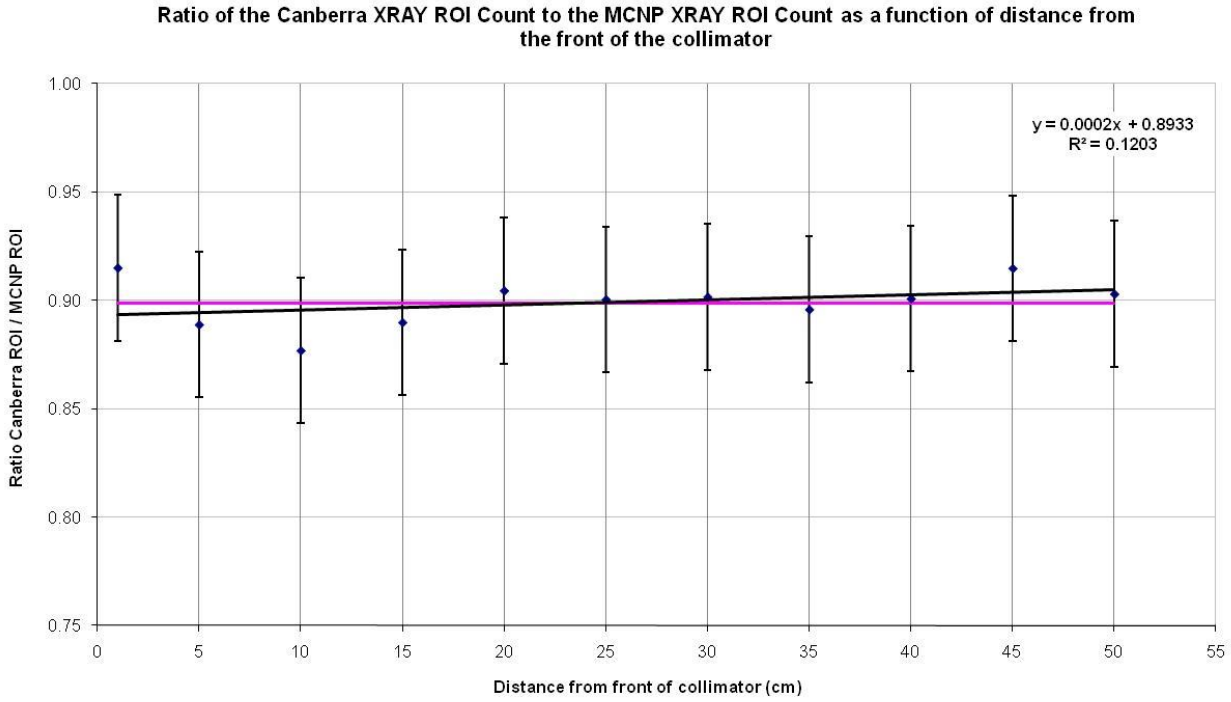

Figure 7.23: Normalised count ratio for the x-ray peak

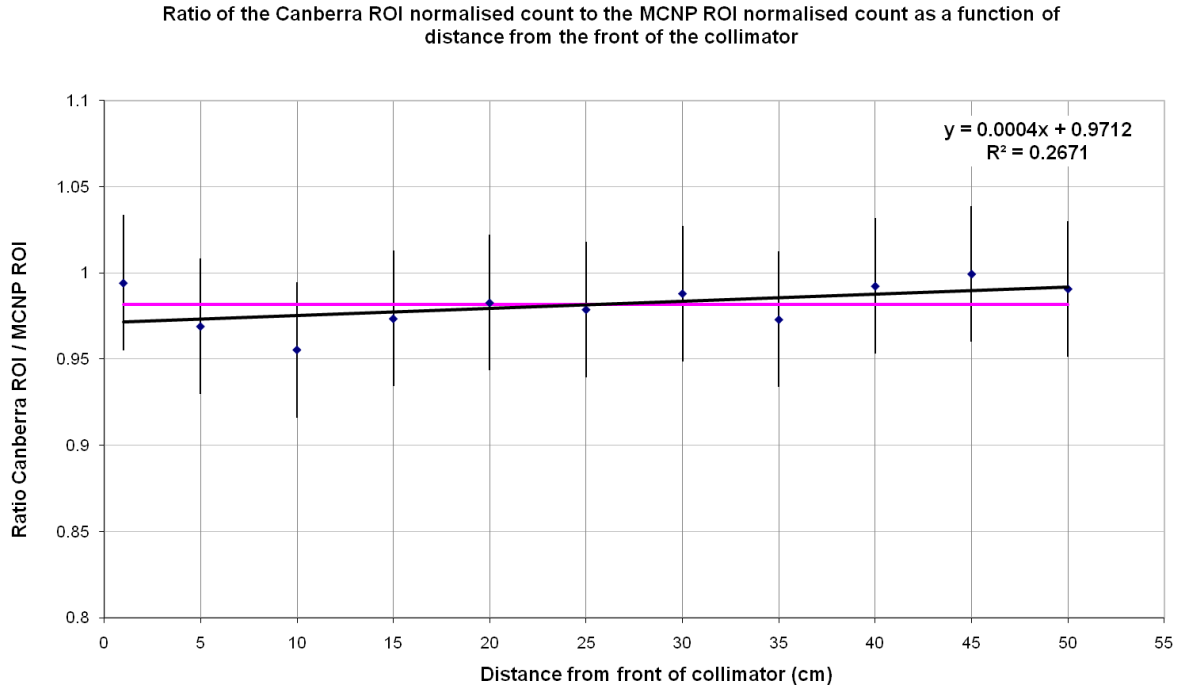

Figure 7.24: Normalised count ratio for the gamma peak

7.7.7 ^{123}I source in a bottle

A point source in air is useful to validate the model without any additional materials. However, it is not representative of the geometry of a thyroid. An assessment was therefore undertaken of an ^{123}I solution dispersed in a plastic cylindrical bottle with a radius of 3.7 cm and a length of 11.5 cm (Astroplast Sterile Eyewash 500 ml). This geometry provides a scattering medium more akin to soft tissue. A similar assessment as previously described for the point source in air was undertaken with the water bottle moved from 5 cm to 50 cm from the front face of the detector.

7.7.8 ^{123}I source in a bottle results

Figure 7.25 shows the comparison between the spectrum for the Canberra and Monte Carlo simulation.

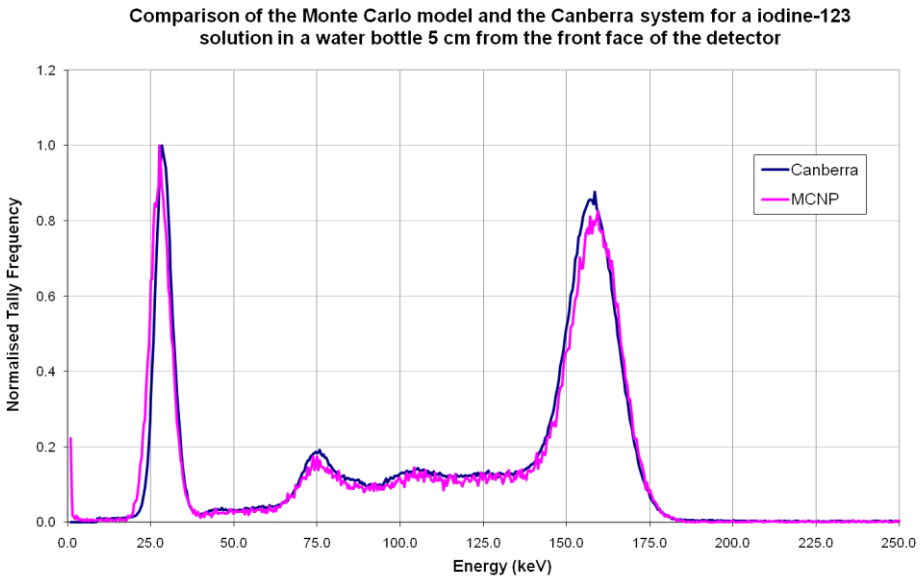

Figure 7.25: Comparison of the Monte Carlo model to the Canberra

Again, we can see from Figure 7.25 that there is good agreement between the Monte Carlo model and the Canberra system.

Table 7.10 shows the normalised ratios for the ^{123}I solution at each distance for the x-ray and gamma peaks.

Distance (cm)	X-ray peak ratio	Gamma peak ratio
5	0.912	1.045
10	0.884	0.999
15	0.886	0.996
20	0.897	1.001
25	0.904	1.000
30	0.880	0.989
35	0.961	1.016
40	0.917	1.019
45	0.907	1.005
50	0.892	1.000
Mean	0.906	1.007
3 × standard deviation	0.070	0.048

Table 7.10: Ratio of the Monte Carlo and Canberra x-ray and gamma peak for various distances in air

Figures 7.26 and 7.27 show a graphical representation of the data presented in Table 7.10. Error bars indicate three standard deviations of the mean.

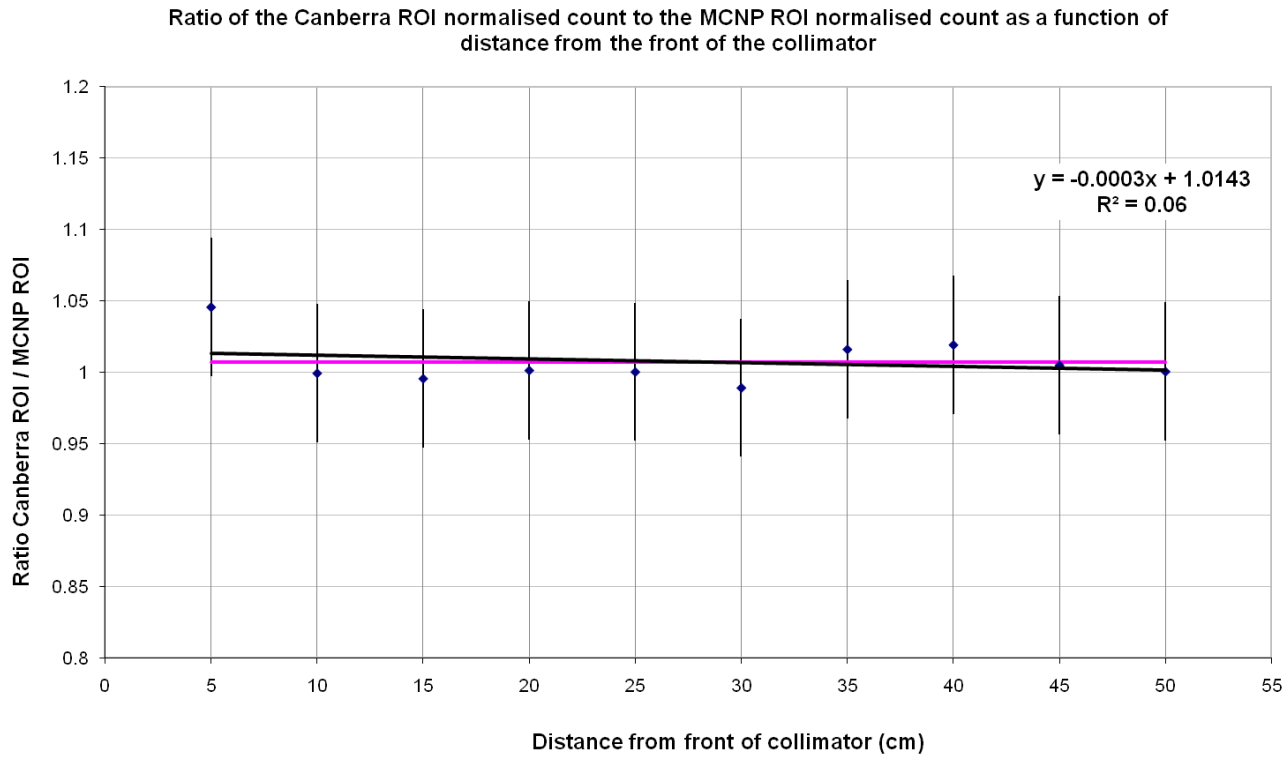

Figure 7.26: Normalised count ratio for the gamma peak

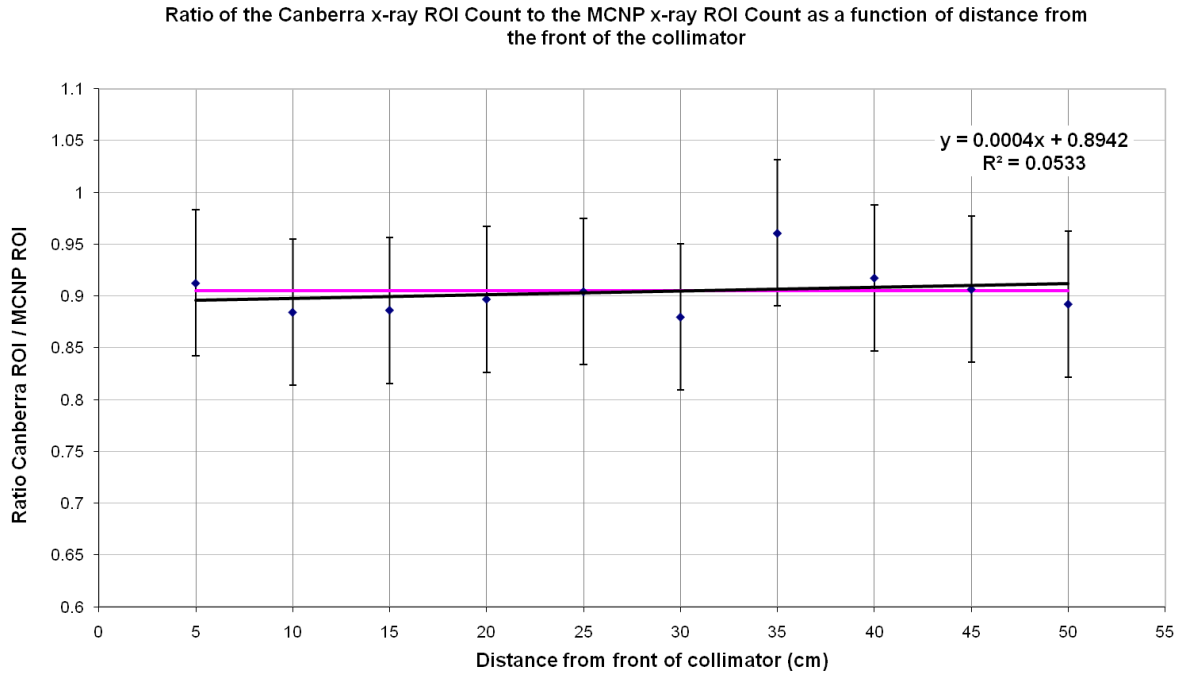

Figure 7.27: Normalised count ratio for the x-ray peak

7.7.9 Point source with PMMA

Finally, to simulate the effect of depth, PMMA was placed on the surface of the collimator. Thicknesses of 1 cm to 8 cm were simulated with the point source behind the PMMA in the central field of the detector. The PMMA is useful as it simulates some scatter that will be encountered in the human measurements, but the added uncertainty is the material specification of the PMMA.

7.7.10 Point Source with PMMA results

Figure 7.28 shows the comparison between the spectra for the Canberra and Monte Carlo simulation for 4 cm thickness of PMMA in front of the collimator.

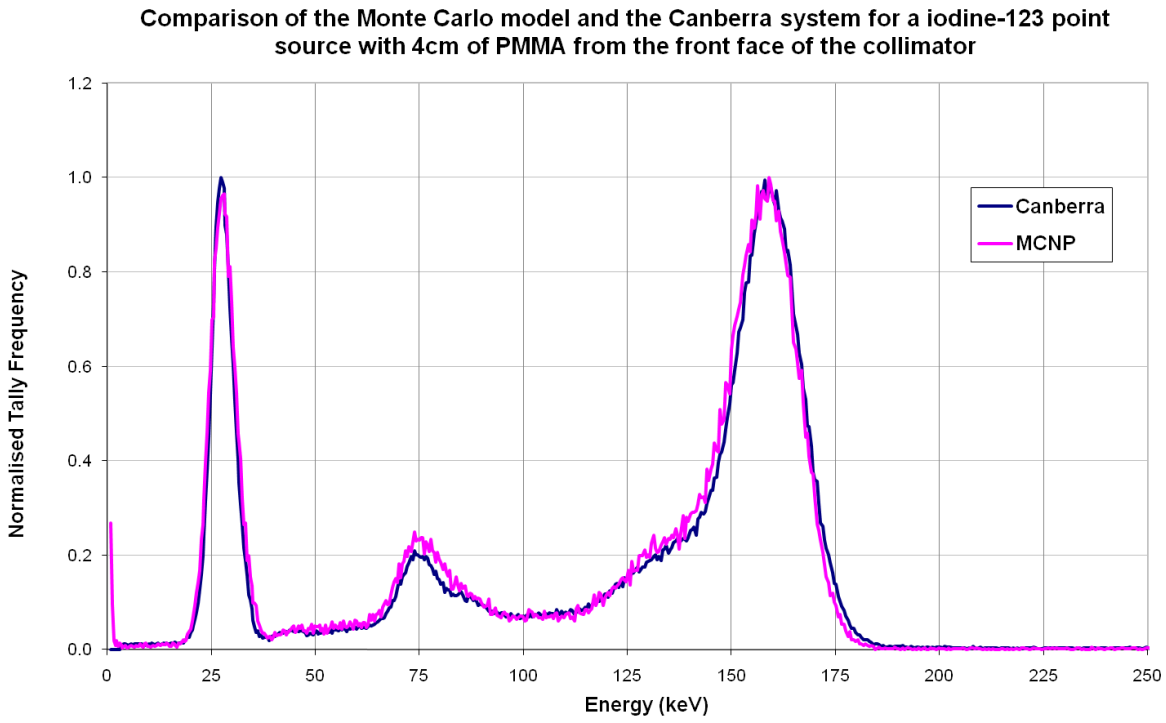

Figure 7.28: Comparison of the Monte Carlo model to the Canberra

Table 7.11 shows the normalised ratios for the ^{123}I point source with increasing thicknesses of PMMA.

PMMA Thickness (cm)	X-ray peak ratio	Gamma peak ratio
1	0.882	0.998
2	0.867	0.972
3	0.887	0.980
4	0.912	0.993
5	0.953	1.025
6	0.965	1.021
7	0.999	1.036
8	0.973	0.999
Mean	0.930	1.003
3 × standard deviation	0.147	0.068

Table 7.11: Ratio of the Monte Carlo and Canberra x-ray and gamma peak for increasing thicknesses of PMMA

Figures 7.29 and 7.30 show a graphical representation of the data presented in Table 7.11. Error bars indicate three standard deviations of the mean.

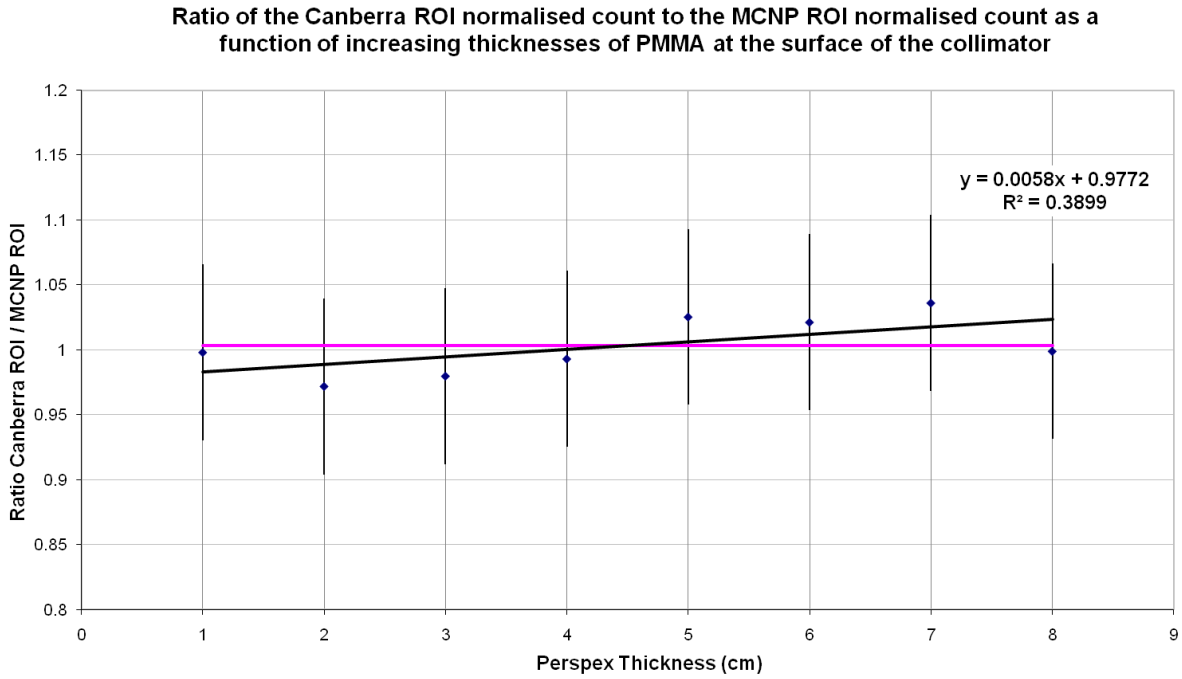

Figure 7.29: Normalised count ratio for the gamma peak

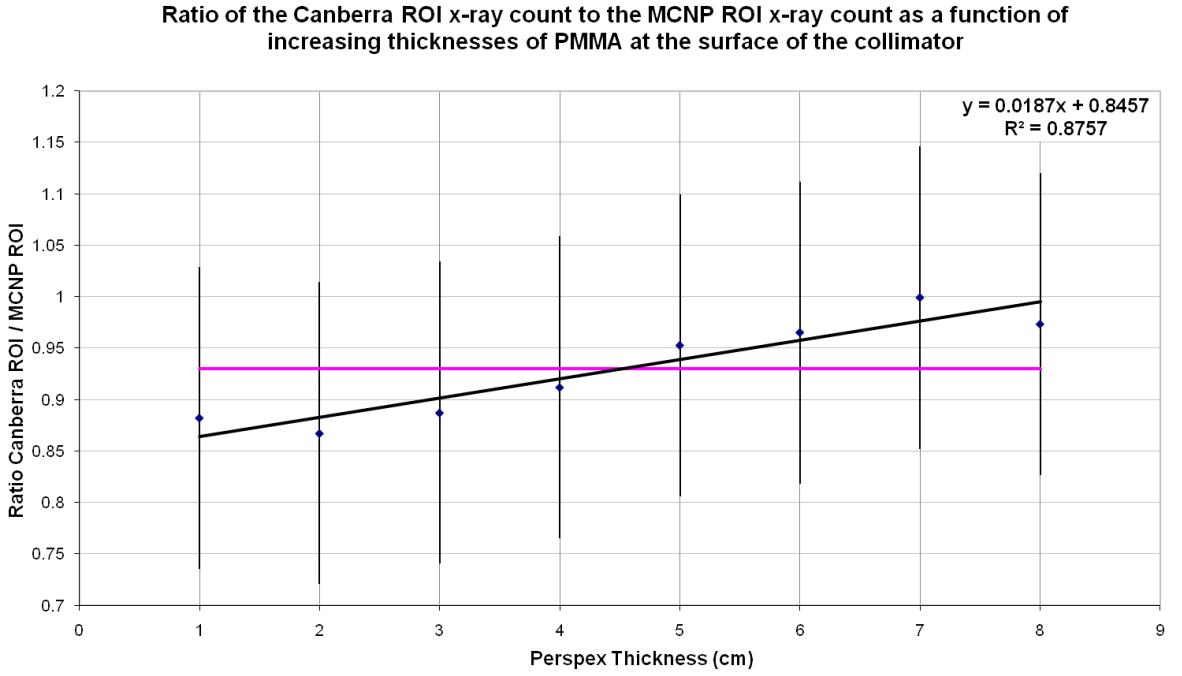

Figure 7.30: Normalised count ratio for the x-ray peak

7.7.11 Discussion of validation results

The validation results indicate that the Monte Carlo model is an accurate representation for the Canberra detector for the measurement of ^{123}I.

Firstly, the results for the point source in air and the ^{123}I source dispersed in the water bottle show consistent relationship when varying the source-detector distance. Unity is not achieved in terms of the ratios, and this is due to slight variations in compositions and geometries between the Monte Carlo model and the Canberra system. However, the ratio is effectively constant in both circumstances, which indicate good agreement between them. The significance of the slope for each case was tested and the P value was > 0.05 in all cases (implying no significant difference from zero).

There is evidently more variation in the model with the varying thicknesses of PMMA. This variation is not reflected in the previous two circumstances and therefore it is likely to be an issue with the material composition. The fact that the x-ray ratio is affected more than the main gamma peak ratio gives more credence to this theory. However, it is noted that all measurements are within three standard deviations of the mean. Significance testing for the main gamma peak returned a P value > 0.05. However, a significant difference ($P<0.05$) was found for the x-ray ratios.

7.8 Summary

In this chapter a Monte Carlo model of the Canberra thyroid uptake counter was produced and validated for a number of different circumstances. This has shown to produce acceptable agreement between what has been measured and what was simulated.

The next stage of the investigations is to determine, using the Monte Carlo model, the degree of uncertainties for the Canberra thyroid uptake counter used within the Medical Physics Department of the University Hospital of Wales. Also, for the particular case of thyroid depth, determine a correction strategy for ^{123}I thyroid uptake assessments that can reasonably be adopted into routine clinical practice.

CHAPTER 8: MONTE CARLO SIMULATION OF FACTORS INFLUENCING THE THYROID UPTAKE ASSESSMENT

8.1 Introduction

In the previous chapter a Monte Carlo model of the Canberra thyroid uptake counter was created and validation of the model was undertaken against the physical system.

In this chapter, a model of the human thyroid gland is used to quantify some of the uncertainties identified in chapter 7. The three areas identified for assessment are: variations in neck to collimator distance, the effect of displacement of the detector and variations in neck tissue thickness.

Finally, a correction strategy is devised for increasing thickness of tissues overlaying the thyroid.

8.2 Modelling of a human thyroid

The first stage of the investigations requires the Monte Carlo modelling of a human thyroid and neck anatomy. The anatomy and physiology of the thyroid gland was detailed in chapter 6.

The main components of the thyroid to be modelled are the left and right thyroid lobes and the connecting isthmus tissue. The neck must also be modelled to allow for the physical attenuation (absorption and scattering) conditions to be replicated.

The neck also contains the trachea and windpipe. Other tissues within the neck are predominately soft tissues and are therefore collectively modelled as soft tissue within the neck.

In the following simulations, no radioactivity is simulated emanating from outside of the thyroid. The influence of background radioactivity is therefore not considered. The major contribution to background radiation would be from tissues above and below the thyroid. Emissions emanating from tissues outside of the field of view would in most cases be attenuated by the lead collimator, unless scattered into the field of view. However, to permit realistic body geometry, a head, torso, arms and legs are also included in the model.

8.2.1 Geometric structure

The geometric structures of the simulated human are shown in Table 8.1 and are identical to the MCNP5 model produced by Davies (2012). Baseline data for the geometric structure of the head, lungs, trachea, thyroid and isthmus is based on data provided in ICRP Publication 23 (ICRP, 1975). Where such information is not available estimations were made.

For simulation, the initial thickness of tissue overlying the thyroid is an important factor. ICRP (1975) gives the amount of overlying tissue in various age groups. The quoted values for a 15 year old female, 36 year old male and 38 year old female were 1 cm, 2 cm and 0.4 cm repesctively. Initially, simulations were conducted with a thyroid depth of 2 cm, in keeping with the baseline modeling data for reference man.

Body part	Modelled geometry	Dimensions
Head	Sphere	Radius: 9.07 cm
Thyroid	Ellipsoid (two lobes)	Length: 6.5 cm Width: 3 cm Depth: 1.75 cm
Isthmus	Cylinder	Length: 2 cm Radius: 1 cm
Trachea	Cylinder	Radius: 0.85 cm Length: 20 cm Thickness: 0.1 cm
Air way	Cylinder	Radius: 0.75 cm Length: 20 cm
Neck	Cylinder	Length: 12 cm Radius: 6 cm
Torso	Rectangle	Length: 52.35 cm Width: 30 cm Depth: 20 cm
Arms	Cylinder	Length: 75 cm Radius: 3 cm
Legs	Cylinder	Length: 90 cm Radius: 7 cm
Lungs	Rectangle	Length: 28 cm Width 13/12 cm Depth 18 cm

Table 8.1: Dimensions of the human model (adapted from ICRP (1975) for the head, lungs, trachea, thyroid and isthmus).

8.2.2 Material composition

The material composition of each of the tissues in the model is shown in Table 8.2. The soft tissues are predominately water and so for ease of modelling, the majority of the tissues are regarded as water with a density of 1 g cm^{-3}. For the thyroid gland, the quoted density is slightly greater at 1.051 g cm^{-3} (ICRP, 1975).

Body part	Composition	Density (g cm^{-3})
Head	Water	1
thyroid	Water	1.051
isthmus	Water	1.051
trachea	Water	1
Air way	Air	0.0012
Neck	Water	1
Torso	Water	1
lungs	Air	0.0012

Table 8.2: Material composition of the modelled reference man (density of the thyroid taken from ICRP (1975))

8.2.3 Monte Carlo model

The cell and surface cards for the Monte Carlo simulations are shown below. The thyroid counter model was transposed accordingly.

```
c Cell card
   10     5      -1 -11 #14 #15 #16          $Neck
   11     5      -1 -12 #10 #14 #15          $Head
   12     5      -1 -13 14 15 #14 #15        $Torso
   13     2 -0.0012 -14 -15 #14 #15          $Lungs
   14     5      -1 -16 #15                  $Trachea
   15     2 -0.0012 -17                      $Airway
   16     5  -1.051 (-18 :-19 :-20 )#14 #15 $Thyroid
   17     5      -1 (-21 :-22 )              $Legs
   18     5      -1 (-23 :-24 )              $Arms

c Surface Cards
   11       rcc 39.39 -6 0 0 12 0 6
   12         s 39.39 12 0 9.07
   13       box 29.5 -58.35 -15.06 0 52.35 0 20 0 0 0 0 30
   14       box 30 -38.5 -14 0 28 0 18 0 0 0 0 13
   15       box 30 -38.5 1 0 28 0 18 0 0 0 0 12
   16       rcc 36.24 -10.5 0 0 20 0 0.85
   17       rcc 36.24 -10.5 0 0 20 0 0.75
   18        sq 1.3061224489796 0.094674556213018 0.44444444444444 0 0 0
                -1 35.39 0 2
   19        sq 1.3061224489796 0.094674556213018 0.44444444444444 0 0 0
                -1 35.39 0 -2
   20       rcc 35.84 -1 0 0 2 0 1
   21       rcc 39.5 -149.85 8 0 90 0 7
   22       rcc 39.5 -149.85 -8 0 90 0 7
   23       rcc 40 -81 -19 0 75 0 3
   24       rcc 40 -81 19 0 75 0 3
```

A cross-sectional image of the Monte Carlo model through the neck along with a vised visualisation of the thyroid gland is shown in Figure 8.1. The thyroid depth of 2 cm is taken from the midpoint of the thyroid lobes to the detector along the central axis.

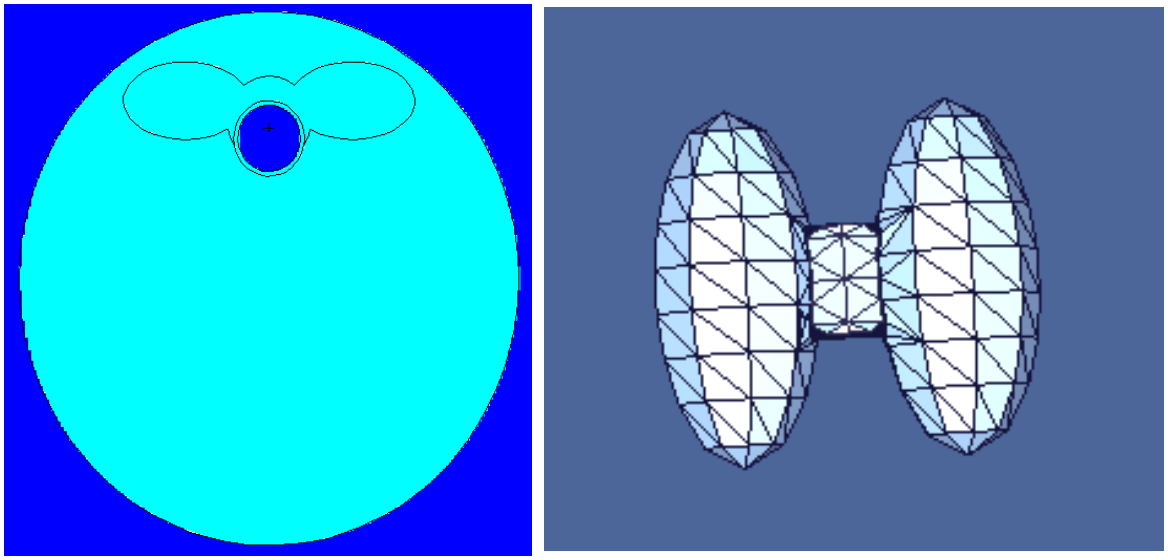

Figure 8.1: Left: Cross-sectional visualisation of the human neck showing the two thyroid lobes, connecting isthmus tissues, trachea and wind pipe. Right: Vised 3D visualisation of the thyroid gland

Figure 8.2 shows a cross-sectional visualisation of the detector and neck with the detector collimator entrance at 10 cm in front of the neck.

Figure 8.3 shows a vised 3D visualisation of the detector centred at 10 cm from the top of the neck. The neck is not shown in the figure to allow for the thyroid gland location to be observed.

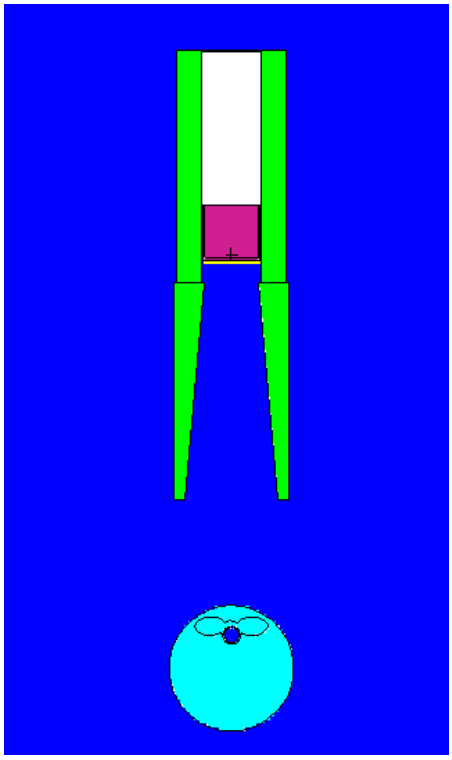

Figure 8.2: Cross-sectional visualisation of the human neck and detector. The entrance to the collimator is 10 cm above the surface of the neck

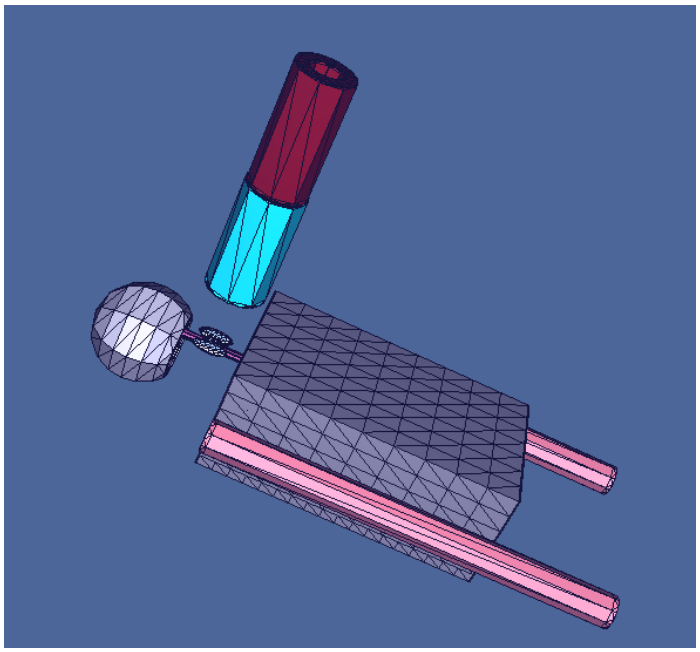

Figure 8.3: Vised visualisation of the Canberra thyroid uptake counter centred over the thyroid at a collimator entrance to thyroid distance of 10 cm

8.2.4 Spectral display of ^{123}I in the thyroid

The initial modelled conditions previously described were used to obtain a spectrum of ^{123}I emanating from the thyroid gland. The source definition for the Monte Carlo simulation is shown below.

```
sdef pos=35.39 0 0 erg=d3 rad=d1 cell=16 par=2 $I-123 within thyroid
si1 0 6
sp1 -21 2
si3 l 0.02720 0.02747 0.03094 &
0.03100 0.03171 0.1590 0.2480 &
0.2810 0.3463 0.4400 0.5053 &
0.52900 0.53850 0.62460 0.68790 &
0.73580 0.78360
sp3 0.24600 0.45800 0.04460 &
0.08660 0.02660 0.82800 &
0.00071 0.00079 0.00125 &
0.00425 0.00314 0.01380 &
0.00379 0.00083 0.00027 &
0.00061 0.00059
```

The source is defined as emanating from the thyroid tissues encompassing cell number 16. A visual depiction of the starting source particle positions for 1000 particles is shown in Figure 8.4.

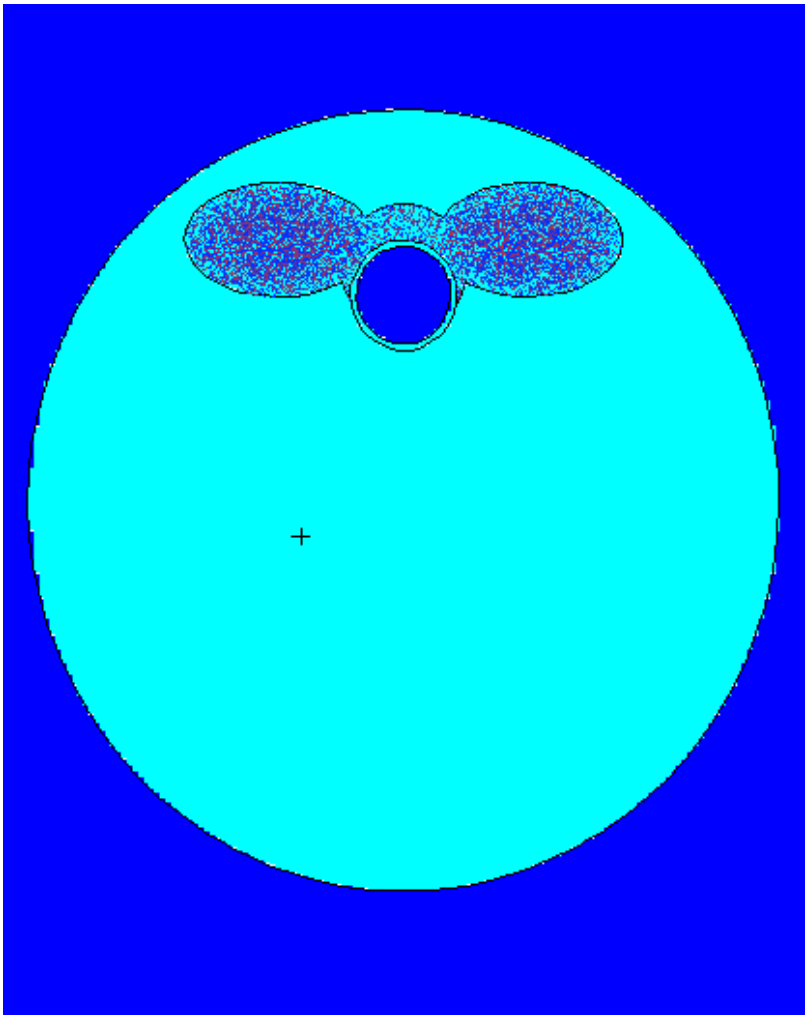

Figure 8.4: Cross-sectional visualisation of the thyroid in the neck with the positions of 1000 starting particles. All the emissions are seen emanating from the thyroid tissues

To create a spectrum of the ^{123}I emissions from the thyroid, 3×10^{7} particles were simulated. The normalised number of particles deposited in the simulated energy bins is plotted in Figure 8.5.

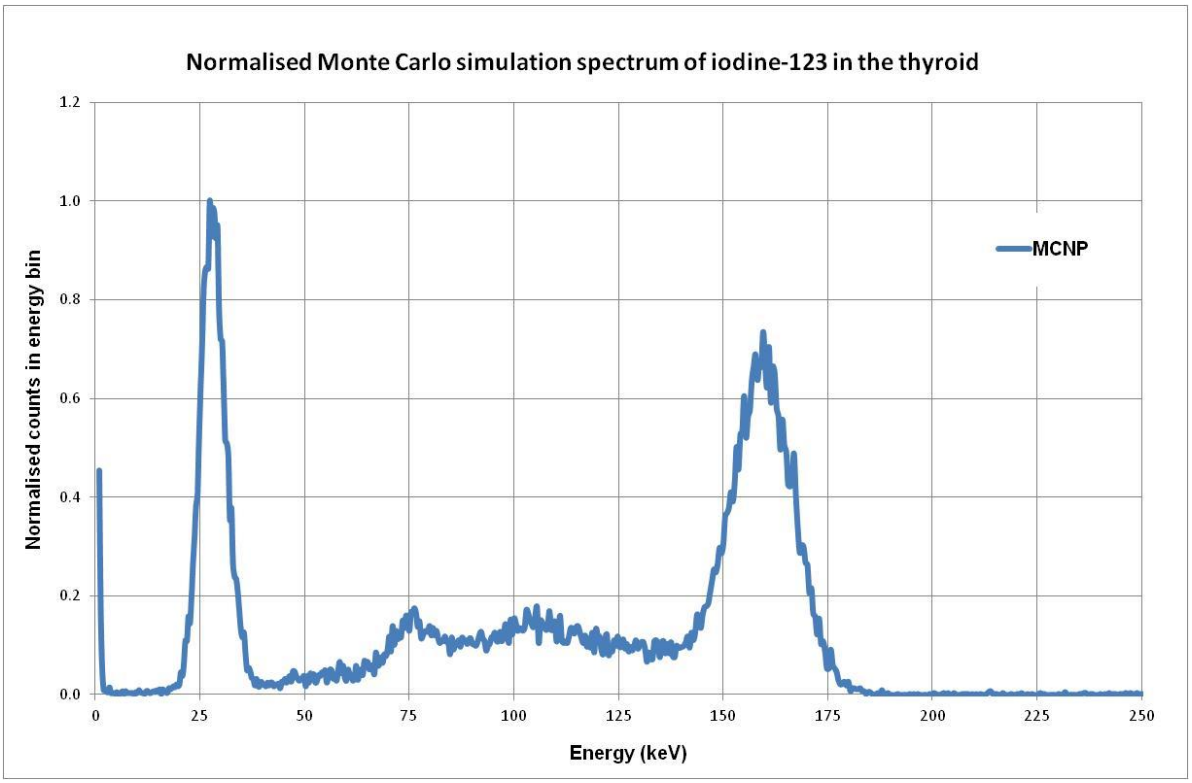

Figure 8.5: Normalised Monte Carlo simulation of ^{123}I in the thyroid

The spectrum clearly displays the x-ray and gamma peaks as previously seen during the validation work. A degree of noisiness of the data is also seen. This is a result of a reduction in the amount of particles being tallied in the crystal due to the distance of the thyroid uptake counter from the source and the scattering conditions. Such nosiness of the data is also evident in a clinical setting.

8.2.5 Determination of x-ray and gamma peak windows

The determination of the x-ray and gamma peak windows for comparative assessments was undertaken qualitatively based on the spectrum displayed in Figure 8.5.

The counting windows for subsequent assessments are shown in Table 8.3.

Peak	Energy Window (keV)
X-ray	15.34 – 38.07
Gamma	138.36 – 178.46

Table 8.3: Energy window ranges

For all the Monte Carlo assessments undertaken in 8.3 the relative error of the mean tally was below 0.05.

8.3 Investigation of the effect of changing parameters associated with thyroid uptake measurement

8.3.1 Vertical displacement of the detector

The first simulations are concerned with varying the vertical position (x axis in the simulation) of the detector above the thyroid. In a clinical setting, a spacer may be employed to ensure a consistent approach to determining the vertical position of the collimator above the surface of the neck. However, as described in chapter 6, even a marginal change in distance, of the order of 1 cm, may produce a variation of up 6.6 % in flux at the face of the detector.

To determine the relationship between vertical displacement and normalised counts, the collimator to neck distance was varied between 7 cm and 13 cm in increments of 0.5 cm by moving the detector (this increases or decreases the distance travelled by radiation in air). Displacements outside of those stated are not deemed to be clinically likely.

The results of varying the detector to thyroid distance can be seen in Table 8.4 and Figure 8.6. All results are normalised to 10 cm neck to collimator distance.

Distance (cm)	Normalised counts in x-ray peak compared to 10 cm	Normalised counts in gamma peak compared to 10 cm
13	0.867	0.860
12.5	0.880	0.878
12	0.900	0.898
11.5	0.923	0.922
11	0.951	0.945
10.5	0.974	0.971
10	1.000	1.000
9.5	1.025	1.031
9	1.052	1.057
8.5	1.087	1.088
8	1.119	1.124
7.5	1.150	1.153
7	1.192	1.185

Table 8.4: Normalised counts in the x-ray and gamma peaks

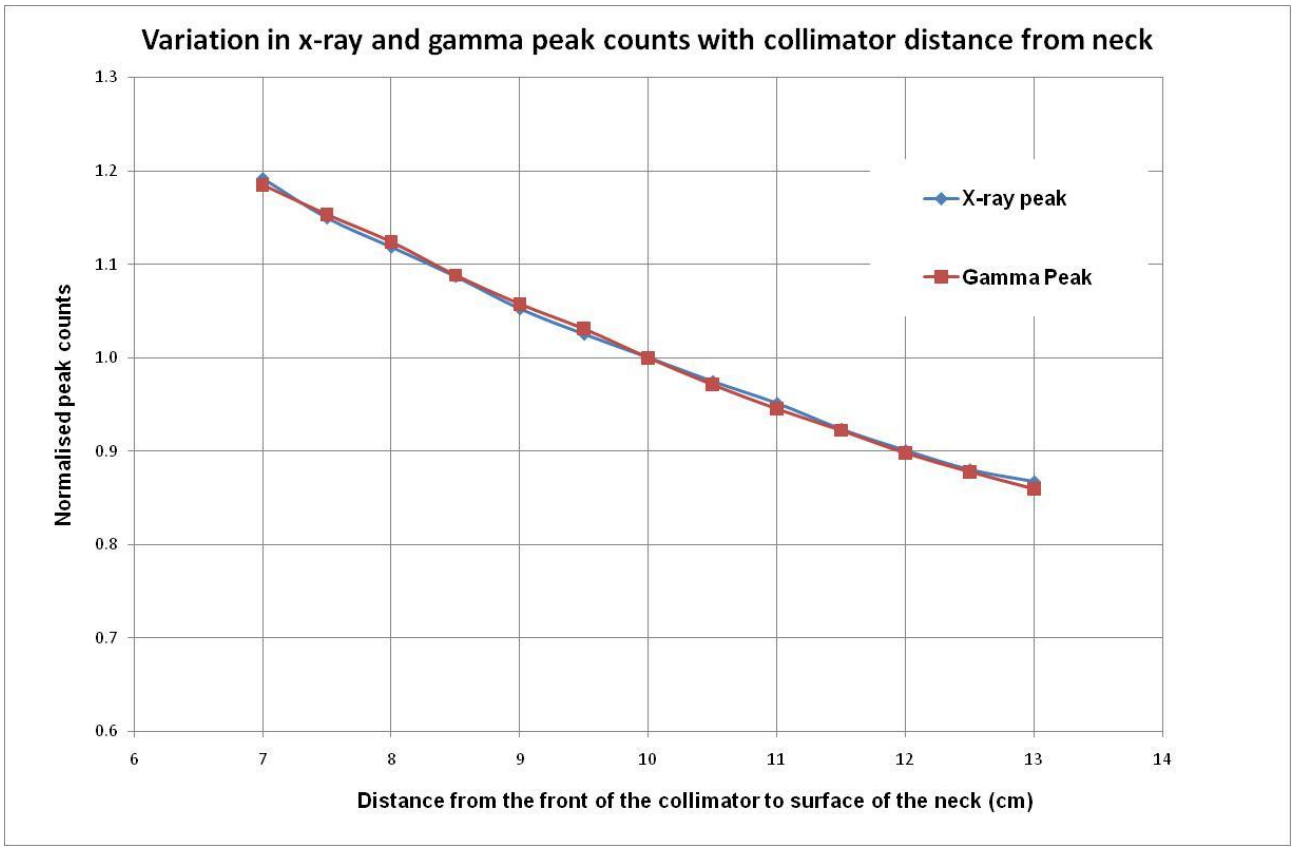

Figure 8.6: Variation in x-ray peak and gamma peaks counts with distance from the collimator to the neck

8.3.2 Vertical displacement of the detector discussion

As expected, the relationship between the normalised counts and the distance between the surface of the collimator and neck appears to be in keeping with the inverse square law. Based on the inverse square law, a change in vertical displacement between 32.89 cm and 33.89 cm from the surface of the neck to the detector surface would result in 5.8% variation in photon flux. The value measured was 5.5% based on the gamma peak measurements (corresponding to a displacement from 10 cm to 11 cm collimator to neck distance) but also accounts for a potential increase in scatter into each of the measurement windows. Even a

moderate change of 0.5 cm either side of 10 cm can produce an uncertainty of 3% in the number of photons deposited in the energy windows.

8.3.3 Horizontal displacement of the detector

A potential source of error which is more likely than vertical displacement error is the horizontal displacement of the detector. In this model, horizontal movements in the Z (medio-lateral) and Y (cranio-caudal) directions were modelled. Increments of 1 cm were made in the positive and negative directions to indicate misalignment of the detector. Figures 8.7 and 8.8 and shows a visualisation for misalignment of 5 cm in the Y and Z directions.

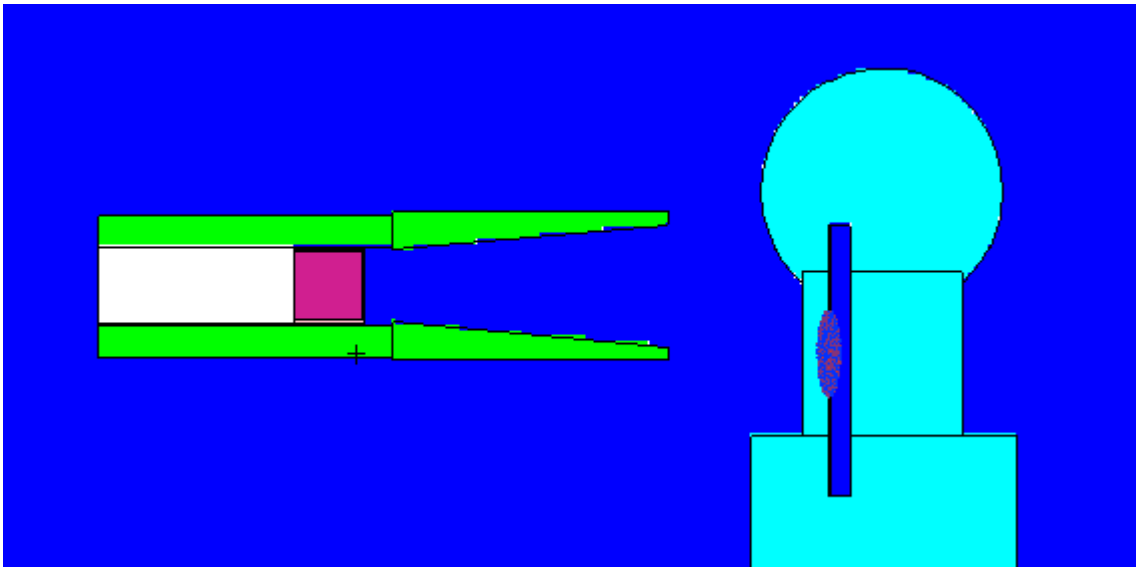

Figure 8.7: Visualisation of the misalignment of the detector distally along the Y axis of the body

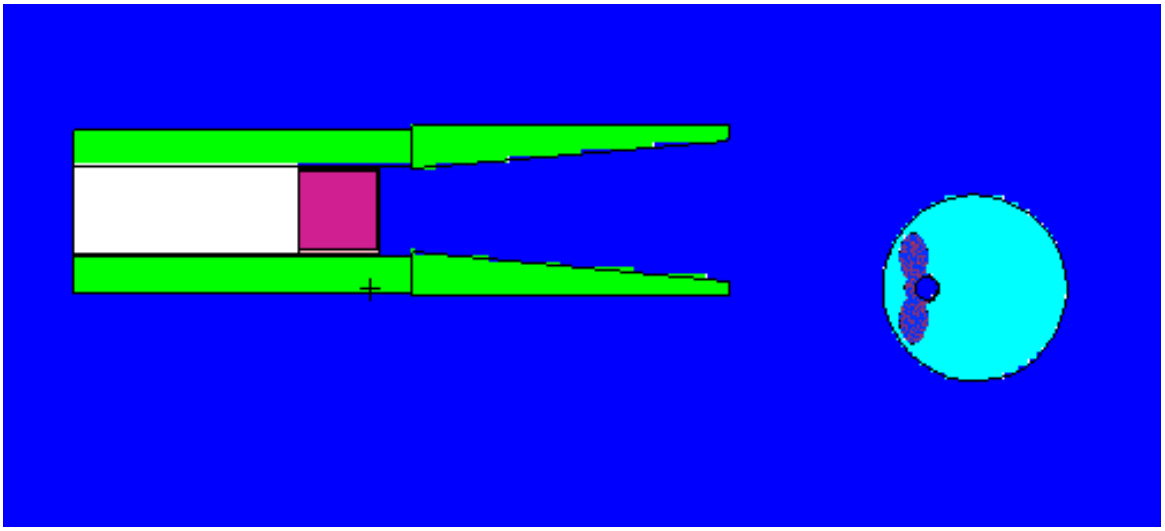

Figure 8.8: Visualisation of the misalignment of the detector laterally along the Z axis of the body

The results are shown in Table 8.5 and Figures 8.9 and 8.10.

Z Location	Normalised counts in x-ray peak compared to Z0	Normalised counts in gamma peak compared to Z0	Y Location	Normalised counts in x-ray peak compared to Y0	Normalised counts in gamma peak compared to Y0
Z5	0.636	0.662	Y5	0.727	0.766
Z4	0.809	0.818	Y4	0.850	0.903
Z3	0.929	0.948	Y3	0.935	0.985
Z2	0.960	0.962	Y2	0.958	1.011
Z1	0.987	0.983	Y1	0.970	1.004
Z0	1.000	1.000	Y0	1.000	1.000
Z-1	1.010	1.003	Y-1	1.008	0.991
Z-2	1.000	0.984	Y-2	0.983	0.975
Z-3	0.955	0.964	Y-3	0.947	0.965
Z-4	0.859	0.823	Y-4	0.894	0.902
Z-5	0.701	0.625	Y-5	0.757	0.767

Table 8.5: Horizontal displacement ratios for the Z and Y directions

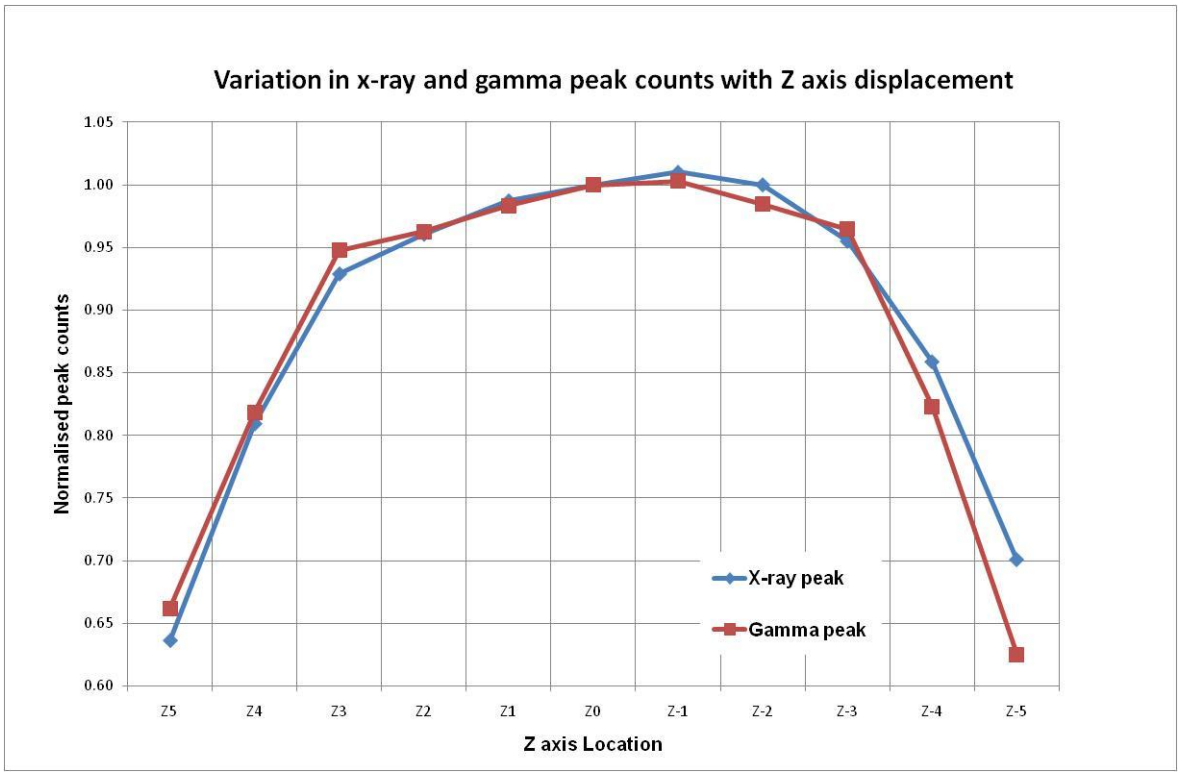

Figure 8.9: Variation of x-ray peak and gamma peaks counts with Z axis displacement

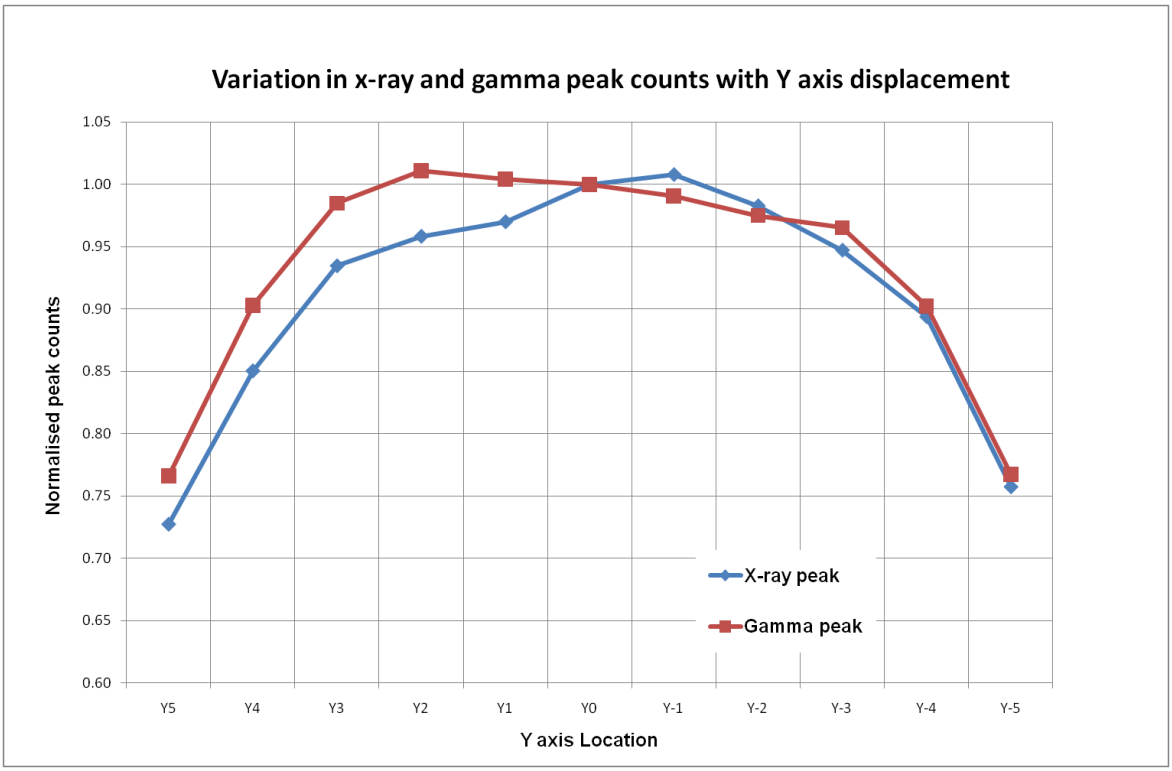

Figure 8.10: Variation of x-ray peak and gamma peaks counts with Y axis displacement

8.3.4 Horizontal displacement of the detector discussion

Figures 8.9 and 8.10 show the effect of detector displacement in the Z and Y axis directions. Considering the symmetrical nature of the geometries in the neck, it would be expected that a displacement in the Z direction would produce a symmetrical effect. In general, both the x-ray peak and the gamma peak variation are symmetrical. The negative Z direction tends to return higher values for both the x-ray and gamma peaks. This is likely to be due to slight geometrical uncertainties in either the MCNP5 input file or the reading of the file by the programme. A 3 cm deviation results in less than a 5.2% error in the uptake assessment, but rises sharply to 35% at 5 cm.

A displacement in the positive Y direction is towards the head and the negative Y direction towards the feet. Considering the differences in potential scattering conditions in these directions, a completely symmetrical distribution is not likely to occur. The effect of movement towards the head seems to have a greater effect on the x-ray peak compared with movement towards the feet. Displacement up to 2 cm either side can be tolerated without significant effect on the gamma counts. A 4 cm displacement, however, could produce up to 10% error in the measured counts in the gamma peak.

Displacement of the neck in the medio-lateral (Z) direction appears to be the more critical than that in the cranio-caudal (Y) direction considering the potential consequences of misalignment.

8.3.5 Thyroid depth in tissue

The effect of thyroid depth is simulated by increasing the thickness of thyroid tissue between the thyroid and the collimator. This is achieved by increasing the radius of the neck. Because of the ellipsoidal shape of the thyroid gland, the distance from the thyroid to the edge of the neck varies depending on what point the measurement is undertaken. Therefore, the depth of the thyroid is taken as the midpoint depth of the thyroid lobes, which can be measured along the central axis to the detector. The reference thyroid depth is taken as 2 cm. Due to the cylindrical nature of the modelled neck, smaller depths were not possible with this configuration.

Two simulations were modelled. In the first instance, the neck to detector distance was kept constant at 10 cm, as would be the case in clinical practice. In the second instance, the detector remained at the same position with increasing thickness of tissue.

The results are shown in Tables 8.6 and 8.7 and graphically displayed in Figures 8.11 and 8.12.

Tissue thickness (cm)	Normalised counts in x-ray peak compared to 2 cm	Normalised counts in gamma peak compared to 2 cm
2	1.000	1.000
2.5	0.845	0.919
3	0.691	0.855
3.5	0.581	0.800
4	0.489	0.731
4.5	0.408	0.686
5	0.343	0.628
5.5	0.295	0.581
6	0.238	0.541

Table 8.6: Increasing neck thickness: count ratios normalised to 2 cm depth (fixed collimator to neck distance of 10 cm)

Tissue thickness (cm)	Normalised counts in x-ray peak compared to 2 cm	Normalised counts in gamma peak compared to 2 cm
2	1.000	1.000
2.5	0.866	0.944
3	0.728	0.903
3.5	0.630	0.865
4	0.536	0.814
4.5	0.461	0.777
5	0.392	0.727
5.5	0.339	0.685
6	0.283	0.656

Table 8.7: Increasing neck thickness: count ratios normalised to 2 cm depth (collimator to neck distance not adjusted)

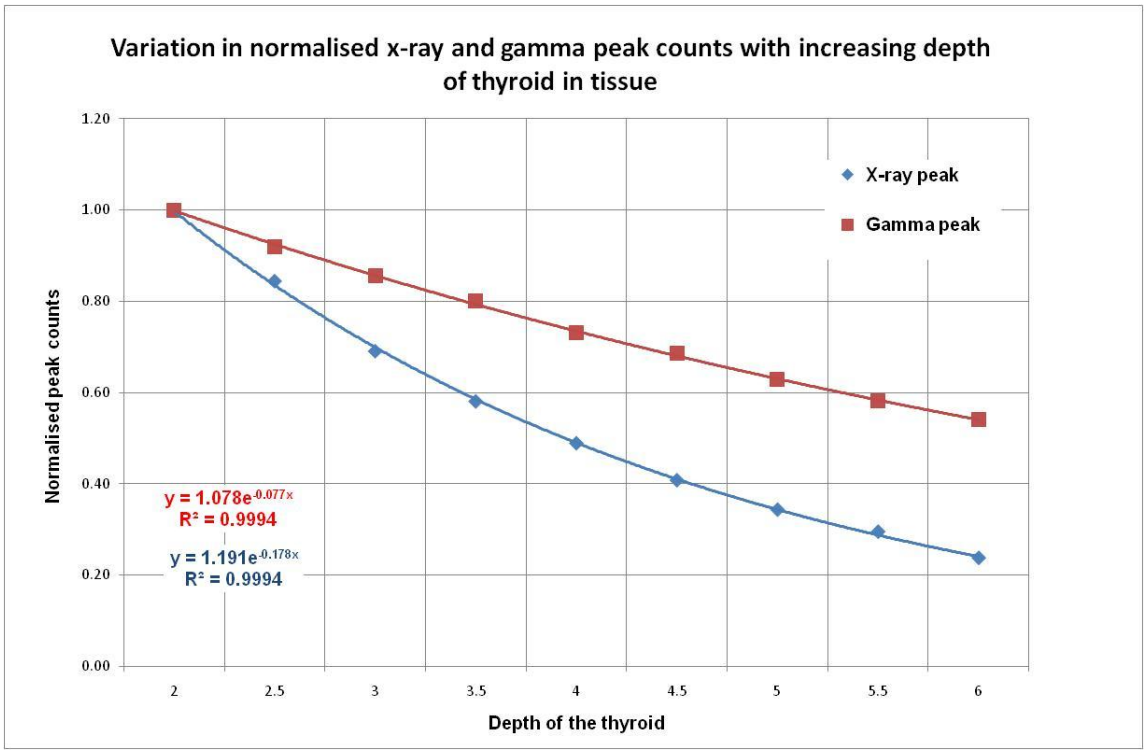

Figure 8.11: Variation in x-ray peak and gamma peaks with increasing depth of thyroid in tissue (fixed collimator to neck distance 10 cm)

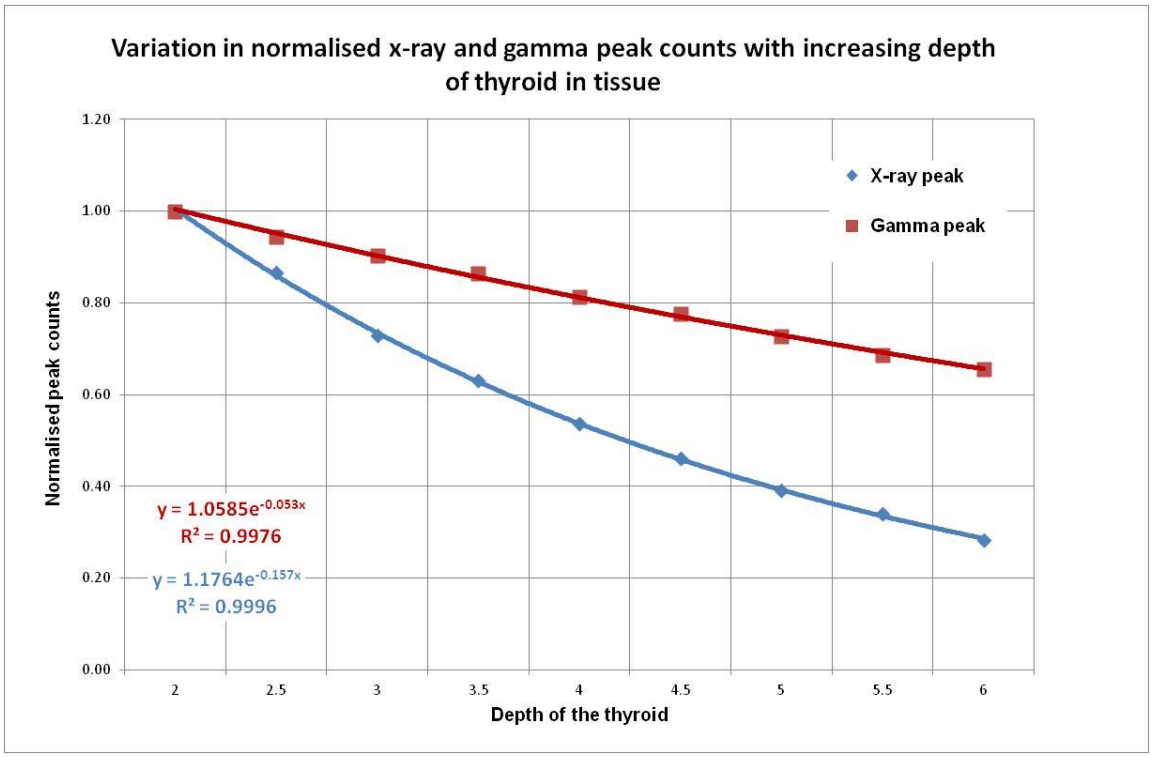

Figure 8.12: Variation in x-ray peak and gamma peaks with increasing depth of thyroid in tissue (collimator to neck distance not adjusted)

8.3.6 Thyroid depth in tissue discussion

The relationship between normalised counts and thyroid depth appears to be exponential between 2 cm and 6 cm depth for the fixed collimator to neck distance and when the detector is not moved.

For a fixed collimator to neck distance of 10 cm, a 1 cm increase in neck tissue thickness results in a 14% reduction in counts in the gamma peak. This increases to over 45% with a thyroid depth of 6 cm. With a fixed collimator to neck distance, there will also be an inverse square law component due to the increasing distance of the detector to the thyroid. When the collimator to neck distance is not adjusted, a reduced discrepancy of 10% is seen between 2 cm and 3 cm thyroid depth.

8.3.7 X-ray to gamma peak ratio

Table 8.8 shows the ratio of the x-ray and gamma peak counts with varying thickness of tissue when the collimator to neck distance is kept at 10 cm and when the collimator to neck distance is not adjusted.

Figure 8.13 is a graphical representation of the data. The variation of this ratio with tissue depth when the detector to neck distance is not adjusted is very similar and not shown.

	Fixed collimator to neck distance 10 cm		Collimator to neck distance not adjusted	
Tissue thickness (cm)	**Ratio x-ray to gamma peak**	**Normalised ratio x-ray to gamma peak to 2 cm**	**Ratio x-ray to gamma peak**	**Normalised ratio x-ray to gamma peak to 2 cm**
2	0.703	1.000	0.703	1.000
2.5	0.646	0.920	0.644	0.917
3	0.568	0.808	0.567	0.807
3.5	0.510	0.726	0.512	0.728
4	0.470	0.669	0.463	0.659
4.5	0.418	0.595	0.416	0.593
5	0.384	0.547	0.379	0.540
5.5	0.356	0.507	0.348	0.495
6	0.309	0.439	0.303	0.431

Table 8.8: Ratio of the x-ray and gamma peak counts with varying thickness of tissue

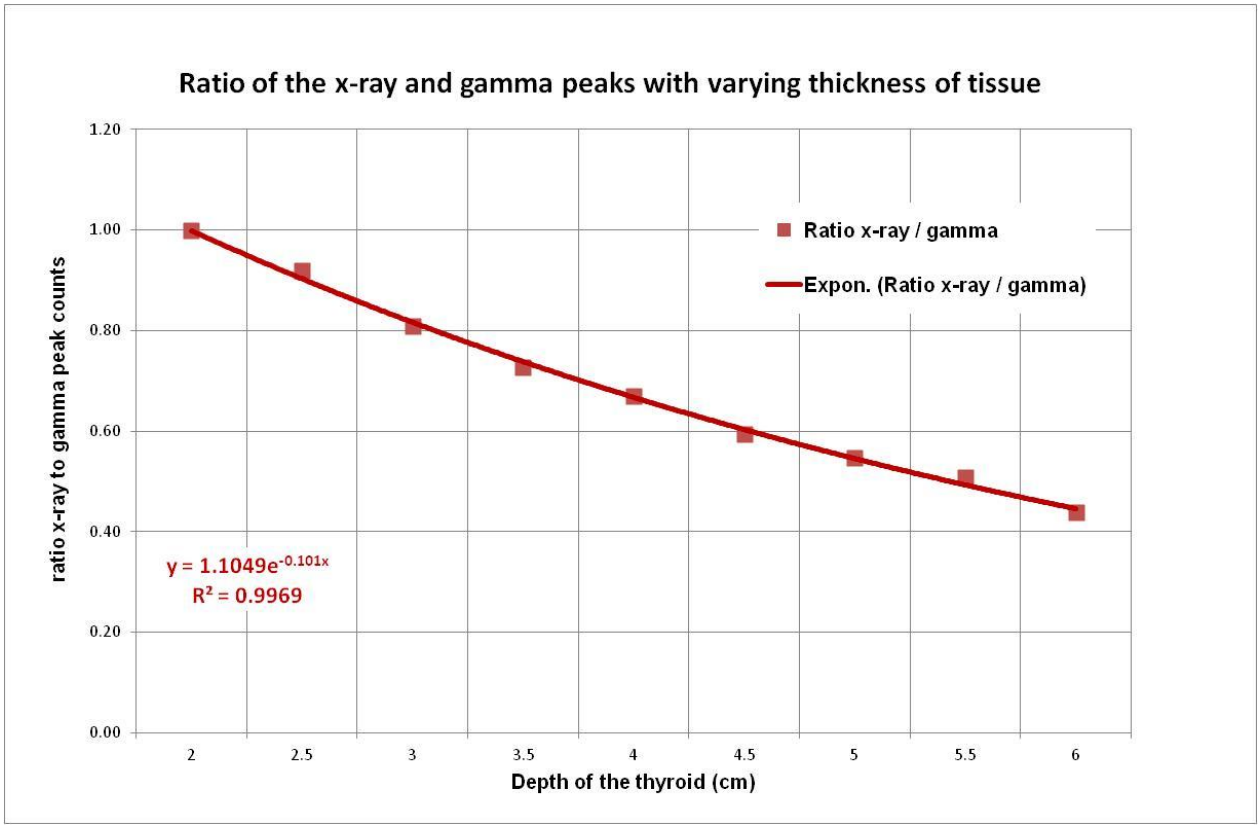

Figure 8.13: Ratio of the x-ray peak to the gamma peak (fixed collimator to neck distance 10 cm)

8.3.8 X-ray to gamma peak correction discussion

Figure 8.13 shows a strong exponential correlation between the ratios of the counts measured in the x-ray peak to those in the gamma peak. In a clinical setting, it would be feasible to measure the counts within the x-ray peak to those in the gamma peak using the appropriate energy windows. The ratio of the counts in the x-ray and gamma peaks may then be cross referenced to Figure 8.13 to estimate the depth of the thyroid in the neck. Once the depth of the thyroid is known, Figure 8.11 may then be used to determine the magnitude of the correction factor that needs to be applied to the gamma peak counts to correct for the error.

8.4 Summary

In this chapter the previously validated Canberra thyroid uptake counter Monte Carlo model was used to simulate a number of the recognised uncertainties in the thyroid uptake assessment. The vertical displacement of the collimator was shown to produce errors of up to 12% with a vertical displacement of 2 cm. The lateral movement of the detector in the medio-lateral and cranio-caudal directions was also found to be a source of error. Although less of a variation is seen over 2 cm in either direction compared to a vertical displacement, accurately centring the collimator over the thyroid gland is inherently more variable as the location of the thyroid in the neck is inferred. Therefore the more extreme misalignment situations may be encountered in clinical practice.

The variation in x-ray and gamma counts with increasing thyroid depth was also investigated. Again, the depth of the thyroid in the neck was shown to be a potential cause of error. A 2 cm increase in tissue thickness can result in a reduction of counts in the gamma peak approaching 27%.

Finally, a correction strategy for the depth of the thyroid in the neck was presented. The ratio of the counts in the x-ray peak compared to the gamma peak can be used as the basis for correcting the depth of the thyroid tissue and therefore improve the accuracy of the thyroid uptake assessment.

CHAPTER 9: CONCLUSIONS AND FURTHER WORK

9.1 Conclusions

The use of MCNP5 Monte Carlo radiation transport simulation code has been shown to be suitable for modelling two common nuclear medicine pieces of equipment, namely a radionuclide calibrator and a thyroid uptake counter. ^{123}I, with its low energy x-ray emissions, may have posed particular modelling issues for the MCNP5 code since these emissions are near the low end of the specified validated energy (1 keV). However, particularly when undertaking the thyroid uptake counter simulations, a high degree of concordance was seen between the physical and modelled spectra. Other validation work provided further reassurance that MCNP5 is a good tool for the medical physics simulations undertaken.

This thesis covers two broad themes regarding issues surrounding ^{123}I: its assay using a radionuclide calibrator and its use for the measurement of radioiodine uptake in the thyroid gland.

Issues regarding ^{123}I assay are well documented as described in section 3.6. However, the novel approach adopted in this thesis is the use of Monte Carlo techniques for the investigation of measurement uncertainties with the UK Fidelis secondary standard instrument. It was shown that uncertainty in the region of 21% was expected when comparing ^{123}I assay in syringe and in a vial. This value was somewhat lower than has been reported in the literature. Comparative simulations were also undertaken with the same chamber filled with argon. These confirmed the uncertainty, in the region of 60-80%, noted in the literature.

The observation of reduced uncertainty for ^{123}I assay when using nitrogen as a chamber gas compared to argon, leads to the conclusion that nitrogen is preferable to argon if no correction strategies are employed. Even so, uncertainties in the region of 21% as found with the modelled syringe are still unacceptable, bearing in mind the principle of ALARP. Therefore, even for a nitrogen filled chamber, the application of suitable correction strategies is warranted. The particular correction strategy investigated in chapter 5 was the use of a copper filter. For an nitrogen filled Fidelis chamber, a copper thickness of 0.3 mm would be sufficient to negate the influence of low energy x-rays on the ionisation current. Increasing the thickness of copper in this circumstance may not be desirable, as the Monte Carlo generated sensitivity curve for the nitrogen filled Fidelis chamber indicates reduced sensitivity when compared to argon. A 0.3 mm thick copper filter is therefore proposed for a nitrogen filled Fidelis chamber.

As well as highlighting uncertainties in the assay of ^{123}I, Monte Carlo modelling also had wider advantages by generating a sensitivity curve for the nitrogen-filled Fidelis chamber. Generating such a curve using experimental measurements with radionuclides can pose issues because of uncertain radionuclide emission data. There is certainly a role for modelling to negate such issues. The generation of new calibration factors (as described in chapter 5) can be undertaken by simulating the radionuclide and container combination, or by using the previously derived sensitivity curve.

The uncertainty associated with assaying ^{123}I is of direct relevance to the thyroid uptake assessment with this radionuclide. Thyroid uptake assessment involves a comparative of the ^{123}I activity in the thyroid gland to that of a radioactive standard embedded within suitable tissue equivalent material (neck phantom). Any difference in ^{123}I measurement sensitivity between the receptacle used for the administration to the patient and that used in the thyroid phantom will inevitably result in an error in the uptake assessment.

The second theme to the thesis was concerned with uncertainties associated with thyroid uptake assessment using the Canberra thyroid uptake counter. Variations in certain parameters and how they propagate to a clinical measurement have been documented in the literature previously. In this study, these issues were quantified for the particular case of a Canberra thyroid uptake counter. While the assessments undertaken looked at the effect of vertical and horizontal displacement of the thyroid uptake counter and thyroid depth with soft tissue as sources of error, other factors as outlined in chapter 6 will also contribute to the uncertainty in the uptake measurement.

For the Canberra detector modelled, a 2 cm vertical displacement of the detector was shown to produce errors of up to 12%. The horizontal movement of the detector in the medio-lateral and cranio-caudal directions was also found to be a source of error, although to a lesser degree for a similar misalignment. The variation in gamma peak counts with increasing thyroid depth showed a 27% reduction in counts for an additional 2 cm of tissue anterior to the thyroid.

In terms of negating the uncertainties identified, two of the three sources of error can be reduced by careful operator preparation. Vertical errors are negated by using a spacer although horizontal displacement can be more difficult to correct while not knowing the exact location of the thyroid in the neck. Using a gamma camera can help reduce horizontal displacement errors either by using the camera itself for the uptake assessment or using it to aid localisation. However, the inherent poor sensitivity of a gamma camera compared to a thyroid uptake counter must be borne in mind.

Finally, for the Canberra thyroid uptake counter a correction strategy for thyroid depth in tissue is proposed based on the differential counts in the x-ray and gamma peaks. This would be achieved by using a dual counting window over both the x-ray and gamma peaks for patient measurements. The relationship of the differential ratio fits an exponential curve to a high degree of correlation. The thyroid depth as estimated using Figure 8.13 can be applied to Figure 8.11 to correct for the depth of the thyroid.

In chapter 1 the following hypothesis was proposed:

"Monte Carlo techniques can be used to accurately simulate a radionuclide calibrator and thyroid uptake counter and quantify uncertainties with respect to ^{123}I measurement"

The work undertaken herein supports this hypothesis.

9.2 Further work

Firstly, while useful work has been undertaken in modelling the Fidelis calibrator, there is scope for significant further work to explore different combinations of vials and syringes as containers of radioactivity. As previously stated, syringe factors do not currently feature in the NPL list of approved Fidelis calibration factors. Therefore, Monte Carlo simulations of a wide number of different syringes, validated against practical measurements, would be of benefit to Fidelis calibrator users. The Monte Carlo simulations undertaken in this thesis gave no consideration to a potential jig as a syringe holder for measurements in the Fidelis. A jig or set of jigs would need to be constructed for proper validation of the syringe factors for implementation into routine practice.

In terms of a field radionuclide calibrator, a copper filter is routinely used to correct ^{123}I assays. Further modelling investigations could be undertaken regarding different filtering materials and the appropriate thickness of the materials to use. Monte Carlo modelling could also be used to investigate the effect of incorporating a suitable filtering material into the design of the calibrator.

In terms of the thyroid uptake assessment, the depth of the thyroid is a significant source of error and suitable correction strategies are worth pursuing. While this thesis proposes a potential methodology based on Monte Carlo simulations, a significant amount of further work is required before incorporation into routine practice. The human model used for the investigations would require significant modification to fully replicate a human neck geometry and composition. Such data could be provided from ultrasound or CT scans and imported into MCNP5; this has

the potential to encompass the full range of anatomies seen in the human population. The effect of abnormal thyroid geometries on the differential x-ray and gamma peak ratios would also need careful consideration.

REFERENCES

Agostinelli, S. et al., 2003. GEANT4 - a simulation toolkit. *Nuclear Instrumentation and Methods in Physics Research A*, 506(3), pp.250-303.

Amino, N. and Tachi, J., 1994. Hypothyroidism: Etiology and Management. In Wheeler, M. and Lazarus, J. *Diseases of the thyroid*. London: Chaptman and Hall. pp.243-67.

Andreo, P., 1991. Monte Carlo techniques in medical radiation physics. *Physics in Medicine and Biology*, 36(7), pp.861-920.

Andreo, P. and Ljungberg, M., 1998. General Monte Carlo Codes for use in Medical Radiation Physics. In M. Ljungberg, S. Strand and M. King, eds. *Monte Carlo Calculations in Nuclear Medicine*. 1st ed. London: Institute of Physics Publishing. pp.37-52.

Anger, H., 1957. A new instrument for mapping gamma-ray emitters. *Biology and Medicine Quarterly Report (University of California Radiation Laboratory, Berkeley-3653)*, p.38.

ARSAC, 2016. *Notes for Guidance on the Clinical Administration of Radiopharmaceuticals and the Use of Sealed Radioactive Sources*. [Online] Available at: https://www.gov.uk/government/uploads/system/uploads/attachment_data/file/492127/ARSAC_NfG_2016.pdf [Accessed 20 April 2016].

Baker, M., 2005. Calibration of the NPL secondary standard radionuclide calibrator for the new 10R Schott, Type 1+ vials. *Applied Radiation and Isotopes*, 63(1), pp.71-77.

Balon, H. et al., 2006. *Society of Nuclear Medicine Procedure Guideline for Thyroid Uptake Measurement. Version 3.0*. [Online] (3.0) Available at: http://snmmi.files.cms-plus.com/docs/Thyroid%20Uptake%20Measure%20v3%200.pdf [Accessed 22 January 2014].

Bennett, B., Repacholi, M. and Carr, Z., 2006. *Health Effects of the Chernobyl Accident and Special Health Care Programmes*. Geneva: World Health Organization.

Bento, J. et al., 2012. Performance assessment and uncertainty evaluation of a portable NaI-based detection system used for thyroid monitoring. *Radiation Protection Dosimetry*, 151(2), pp.252-61.

BNMS, 2003. *Radionuclide Thyroid Scans*. [Online] Available at: http://www.bnms.org.uk/procedures-guidelines/bnms-clinical-guidelines/radionuclide-thyroid-scans.html [Accessed 22 January 2014].

Bolch, W., 2010. The Monte Carlo Method in Nuclear Medicine: Current Uses and Future Potential. *Journal of Nuclear Medicine*, 51(3), pp.337-39.

Brown, B. et al., 2001. *Medical Physics and Biomedical Engineering*. 1st ed. London: Institute of Physics Publishing.

Canberra, 2001. *Model ASA-100, NaI Multichannel Analyzer Board*. Meriden: Canberra Industries, Inc.

Canberra, 2006. *Genie™ 2000 Basic Spectroscopy Software*. [Online] Available at: http://www.canberra.com/products/radiochemistry_lab/pdf/G2K-BasicSpect-SS-C40220.pdf [Accessed 11 February 2014].

Canberra, 2009. *Canberra Model 802 Scintillation Detectors*. Meriden: Canberra Industries, Inc.

Canberra, 2011. *Product Data Sheet*. [Online] Available at: http://www.canberra.com/products/detectors/scintillation-detectors.asp?Accordion1=0 [Accessed 3 April 2011].

Chauvie, S. et al., 2002. The GEANT4 simulation toolkit and its low energy electromagnetic physics package. *Medical Physics*, 29(6), p.1231.

Cherry, R., 2016. *International Labour Office. Encyclopaedia of Occupational Health and Safety: Chapter 48 - Radiation: Ionizing*. [Online] Available at: http://www.ilocis.org/documents/chpt48e.htm [Accessed 23rd June 2016].

Cherry, S., Sorenson, J. and Phelps, M., 2003. *Physics in Nuclear Medicine*. 3rd ed. Philadelphia: SAUNDERS.

Chervu, S., Chervu, L., Goodwin, P. and Blaufox, M., 1982. Thyroid uptake measurement with I-123: problems and pitfalls: concise communication. *Journal of Nuclear Medicine*, 23(8), pp.667-70.

Chiste, V. et al., 2004. *Monographie BIPM-5: Table of Radionuclides*. Frane: Bureau International des Poids et Measures (BIPM).

Davies, C., 2012. *Monte Carlo Modelling of a Thyroid Uptake Counter*. Project Report. Cardiff: Cardiff University.

Dewji, S., 2009. *Assessing internal contamination after a radiological dispersion device event using a 2×2-Inch sodium iodide detector*. Thesis. Georgia: Georgia Institute of Technology.

EC, 1997. Council Directive 97/43/Euratom. *Official Journal of the European Communities*, L(180), pp.22-27.

EC, 2013. Council Directive 2013/59/Euratom. *Official Journal of the European Union*, L(13), pp.1-73.

Floyd, J. et al., 1985. Thyroid Uptake and Imaging with Iodine-123 at 4-5 Hours: Replacement of the 24-Hour iodine-131 Standard. *Journal of Nuclear Medicine*, 26(8), pp.884-87.

Fog, L. and Collins, P., 2008. Monte Carlo simulation of the dose to nuclear medicine staff wearing protective garments. *Australasian Physical and Engineering Sciences in Medicine*, 31(4), pp.307-16.

Gadd, R. et al., 2006. *Protocol for Establishing and Maintaining the Calibration of Medical Radionuclide Calibrators and their Quality Control*. Teddington: NPL.

Geant4, 2013. *Applications*. [Online] Available at: http://geant4.web.cern.ch/geant4/applications/index.shtml [Accessed 23 June 2016].

Geant4, 2016. *Geant4 Download*. [Online] Available at: http://geant4.web.cern.ch/geant4/support/download.shtml [Accessed 23 June 2016].

Gostely, J. and Laedermann, J., 2000. Simulation of the response of the IG11 4pi-gamma ionization chamber using GEANT Monte Carlo code. *Applied Radiation and Isotopes*, 52(3), pp.447-53.

Guhlke, S., Verbruggen, A. and Vallabhajosula, S., 2007. Radiochemistry and Radiopharmacy. In H. Biersack and L. Freeman, eds. *Clinical Nuclear Medicine*. Berlin: Springer. pp.34-76.

Harris, C. et al., 1984. Effects of characteristic X-rays on assay of I-123 by dose calibrator. *Journal of Nuclear Medicine*, 25(12), pp.1367-70.

Hart, D. and Wall, B., 2005. UK nuclear medicine survey 2003-2004. *Nuclear Medicine Communications*, 26(11), pp.937-46.

Hirayama, H. et al., 2016. *The EGS5 Code System. SLAC Report Number SLAC-R-730*. Stanford: Stanford University Stanford Linear Accelerator Center.

IAEA, 1962. The Calibration and Standardization of Thyroid Radioiodine Uptake Measurements. *Physics in Medicine and Biology*, 6(4), p.533.

IAEA, 2009. *Cyclotron Produced Radionuclides: Physical Characterstics and Production Methods*. Vienna: IAEA.

IAEA, 2015. *Principles of an isotope calibrator*. [Online] Available at: https://nucleus.iaea.org/HHW/Radiopharmacy/VirRad/Quality_Control_Procedures/Quality_Control_Module/Radioactivity_concentration/Measurement_tools/Isotope_Calibrator/Principles_of_an_isotope_calibrator/index.html [Accessed 15 June 2015].

ICRP, 1975. Report on the Task Group on Reference Man. ICRP Publication 23. *Annals of the ICRP*, 23.

ICRP, 1983. Radionuclide Trasnformations. Energy and Intensity of Emissions. ICRP Publication 38. *Annals of the ICRP*, 11-13(38), pp.442-43.

Jan, S. et al., 2011. GATE V6: a major enhancement of the GATE simulation platform enabling modelling of CT and radiotherapy. *Physics in Medicine and Biology*, 56(4), pp.881-901.

Jan, S. et al., 2004. GATE: a simulation toolkit for PET and SPECT. *Physics in Medicine and Biology*, 49(19), pp.4543-61.

Kato, K. et al., 2011. Calculation of personal dose equivalent for positron-emitting radionuclides using Monte Carlo code EGS5. *Radiation Protection and Dosimetry*, 146(1-3), pp.202-05.

KEK, 2016. *EGS5 Web Page*. [Online] Available at: http://rcwww.kek.jp/research/egs/egs5.html [Accessed 25 June 2016].

Kowalsky, R. and Johnston, R., 1998. Dose calibrator assay of iodine-123 and Indium-111 with a copper filter. *Journal of Nuclear Medicine Technology*, 26(2), pp.94-98.

Kramer, G., Chamberlain, M. and Yiu, S., 1997. A study of thyroid radioiodine monitoring by Monte Carlo simulations: implications for equipment design. *Physics and Medicine in Biology*, 42(11), pp.2175 - 2182.

Kramer, G. and Crowley, P., 2000. The assessment of the effect of the thyroid size and shape on the activity estimate using monte carlo simulation. *Health Physics*, 78(6), pp.727-38.

Ladenson, P., 2003. Problems in the Management of Hypothyroidism. In L. Braveman, ed. *Diseases of the Thyroid*. 2nd ed. Totowa: Humana Press Inc. pp.161-76.

Laedermann, J., Valley, J., Bulling, S. and Bochud, F., 2004. Monte Carlo calculation of the sensitivity of a commercial dose calibrator to gamma and beta radiation. *Medical Physics*, 31(6), pp.1614-22.

Lamare, F. et al., 2006. Validation of a Monte Carlo simulation of the Phillips Allegro/GEMINI PET systems using GATE. *Physics in Medicine and Biology*, 51(4), pp.943-62.

Lazarus, J., 1994. Clinical features. In M. Wheeler and J. Lazarus, eds. *Diseases of the Thyroid*. London: Chapman and Hall. pp.165-69.

Lee, K., Siegel, M. and Fernandez, O., 1995. Discrepancies in thyroid uptake values use of commercial thyroid probe systems versus scintillation cameras. *Clinical Nuclear Medicine*, 20(3), pp.199-202.

Ljungberg, M., 1998. Introduction to the Monte Carlo Method. In M. Ljungberg, S. Strand and M. King, eds. *Monte Carlo Calculations in Nuclear Medicine*. 1st ed. London: Institute of Physics Publishing. p.9.

Maguire, W., 1988. Deadtime Error with Iodine-123 Thyroid Uptake Measurement. *Journal of Nuclear Medicine Technology*, 16(3), pp.105-08.

Martin, P. and Rollo, F., 1977. Estimation of Thyroid Depth and Correction for I-123 Uptake Measurements. *Journal of Nuclear Medicine*, 18(9), pp.919-24.

MedicalTerms.info, 2012. *Thyroid Gland*. [Online] Available at: http://medicalterms.info/anatomy/Thyroid-Gland/ [Accessed 22 January 2014].

Metropolis, N., 1987. The Beginning of the Monte Carlo Method. *Los Alamos Science*, Special Issue, pp.125-30.

Metropolis, N. and Ulam, S., 1949. The Monte Carlo Method. *Journal of the American Statistical Association*, 44(247), pp.335-41.

National Research Council, 2015. *EGSnrc: software tool to model radiation transport*. [Online] Available at: http://www.nrc-cnrc.gc.ca/eng/solutions/advisory/egsnrc_index.html [Accessed 25 June 2016].

National Research Council, 2016. *EGSnrc*. [Online] Available at: http://nrc-cnrc.github.io/EGSnrc/ [Accessed 25 June 2016].

NPL, 2015a. *Primary Standards of Radioactivity*. [Online] Available at: http://www.npl.co.uk/upload/pdf/ps.pdf [Accessed 14 August 2015].

NPL, 2015b. *Fidelis Secondary Standard Radionuclide Calibrator*. [Online] Available at: http://www.npl.co.uk/science-technology/radioactivity/products-and-services/fidelis-secondary-standard-radionuclide-calibrator [Accessed 15 June 2015].

NPL, 2015c. *CALIBRATION FACTORS FOR THE NPL 'FIDELIS' SECONDARY STANDARD RADIONUCLIDE CALIBRATOR*. [Online] Available at: http://www.npl.co.uk/upload/pdf/fidelis_ssrc_factors.pdf [Accessed 15 June 2015].

O'Connor, M. and Malone, J., 1978. Thyroid uptake measurements: the influence of gland depth, gland mass and lobe separation. *The British Journal of Radiology*, 51(606), pp.454-59.

Olsovcová, V., 2010. Monte Carlo simulation o factivity measurement of 123I, 111In and 153Sm with a radionuclide calibrator. *Applied Radiation and Isotopes*, 68(7-8), pp.1383-87.

ORAU, 2015. *ENSDF Decay Data in the MIRD (Medical Internal Radiation Dose) Format for 123I*. [Online] (Feb-1994) Available at: http://www.orau.org/PTP/PTP%20Library/library/DOE/bnl/nuclidedata/MIRI123.htm [Accessed 25 April 2016].

Ośko, J., Golnik, N. and Pliszczynski, T., 2007. Uncertainties in determination of 131I activity in the thyroid gland. *Radiation Protection Dosimetry*, 125(1-4), pp.516-19.

Paganetti, H., 2014. Monte Carlo simulations will change the way we treat patients with proton beams today. *The British Journal of Radiology*, 87(1040).

Patton, K. and Thibodeau, G., 2013. *Anatomy and Physiology*. 8th ed. St. Louis: Mosby Elsevier.

Powser, R. and Powser, E., 2006. *Essential Nuclear Medicine Physics*. 2nd ed. Oxford: Blackwell Publishing Ltd.

Prekeges, J., 2011. *Nuclear Medicine Instrumentation*. 1st ed. Sudbury, Massachusetts: Jones and Bartlett.

Price, R., 2008. Basic Monte Carlo Concepts. *MCNP Training Course Notes*, 15th - 19th September 2008, Lymm, UK.

Reed, A., 2007. *Medical Physics calculations with MCNP: A Primer*. Summer American Nuclear Society Meeting Conference Procedings. Los Alamos: Los Alamos National Laboratory.

Reynaert, N. et al., 2007. Monte Carlo treatment planning for photon and electron beams. *Radiation Physics and Chemistry*, 76(4), pp.643-86.

Rogers, D. and Bielajew, A., 1990. Monte Carlo Techniques of Electron and Photon Transport for Radiation Dosimetry. In K. Kase, B. Bjarngard and F. Attix, eds. *The Dosimetry of Ionizing Radiation (Chapter 5, Vol. III)*. 1st ed. Academic Press. pp.433-36.

Ross, D., 2003. Management of the Various Causes of Thyrotoxicosis. In Braverman, L. *Diseases of the Thyroid*. 2nd ed. Totowa: Humana Press Inc. pp.177-98.

Sarrut, D. et al., 2014. A review of the use and potential of the GATE Monte Carlo simulation code for radiation therapy and dosimetry applications. *Medical Physics*, 41(6).

Scarboro, S. et al., 2009. Validation of a Monte Carlo Simulation of a Thyroid Uptake System using Various Sources and a Slab Phantom. *Nuclear Technology*, 168(1), pp.169-72.

Shapiro, B., Zanin, D. and Schipper, R., 2014. Reference-free thyroid uptake measurement. *Nuclear Medicine Communications*, 35(4), pp.382-90.

Southern Scientific Ltd., 2009. *SSI / NPL Fidelis*. [Online] Available at: http://www.southernscientific.co.uk/catalog/products/southern-scientific-npl-fidelis?category-id=113 [Accessed 5 November 2015].

Staelens, S. et al., 2003. Monte Carlo simulation of a scintillation camera using Gate: Validation and application Modelling. *Physics in Medicine and Biology*, 48(18), pp.3021-42.

Stsjazhko, V. et al., 1995. Childhood thyroid cancer since accident at Chernobyl. *The British Medical Journal*, 310(6982), p.801.

Suzuki, A., Suzuki, M. and Weis, A., 1976. Analysis of a Radioisotope Calibrator. *Journal of Nuclear Medicine Technology*, 4(4), pp.193-98.

Temple, B., 2007. *MCNP Generated Detector Response and Blur Functions for CsI Detectors*. MCNP references. Los Alamos: Los Alamos National Laboratory.

Thompson, W. et al., 1997. Ionisation Chamber Measurements of I123 Using a Copper Filter. In H. Bergmann, A. Kroiss and H. Sinzinger, eds. *Radioactive Isotopes in Clinical Medicine and Research XXII*. Basal: Birkhauser. pp.231-36.

Tyler, D. and Woods, M., 2002. *Syringe Calibration Factors and Volume Correction Factors for the NPL Secondary Standard Calibrator*. [Online] Available at: http://publications.npl.co.uk/npl_web/pdf/cirm56.pdf [Accessed 20 April 2016].

Tyler, D. and Woods, M., 2003. Syringe calibration factors for the NPL Secondary Standard Radionuclide Calibrator for selected medical radionuclides. *Applied Radiation and Isotopes*, 59(5-6), pp.367-72.

UK Government, 1978. *The Medicines (Administration of Radioactive Substances) Regulations 1978. Statutory Instrument No. 1006.* [Online] Available at: http://www.legislation.gov.uk/uksi/1978/1006/made [Accessed 25 April 2016].

UK Government, 1995. *The Medicines (Administration of Radioactive Substances) Ammendment Regulations 1995. Statutory Instrument No. 2147*. [Online] Available at: http://www.legislation.gov.uk/uksi/1995/2147/contents/made [Accessed 25 April 2016].

UK Government, 2000. *The Ionising Radiation (Medical Exposure) Regulations 2000. Statutory Instrument No. 1059.* [Online] Available at: http://www.legislation.gov.uk/uksi/2000/1059/contents/made [Accessed 25 April 2016].

UK Government, 2006a. *The Ionising Radiation (Medical Exposure) Ammendment Regulations 2006. Statutory Instrument No. 2523*. [Online] Available at:

www.legislation.gov.uk/uksi/2006/2523/pdfs/uksi_20062523_en.pdf [Accessed 25 April 2016].

UK Government, 2006b. *The Medicines (Administration of Radioactive Substances) Ammendment Regulations 2006. Statutory Instrument No. 2806.* [Online] Available at: http://www.legislation.gov.uk/uksi/2006/2806/contents/made [Accessed 25 April 2016].

UK Government, 2011. *The Ionising Radiation (Medical Exposure) Ammendment Regulations 2011. Statutory Instrument No. 1567*. [Online] Available at: http://www.legislation.gov.uk/uksi/2011/1567/made [Accessed 25 April 2016].

Ulanovsky, A., Minenko, V. and Korneev, S., 1997. Influence of measurement geometry on the estimate of 123I activity in the thyroid: Monte Carlo simulation of a detector and a phantom. *Health physics*, 72(1), pp.34-41.

Vahjen, G., Lange, R. and Merola, T., 1992. Thyroid Uptake Neck Phantoms are Not Created Equal. *Journal of Nuclear Medicine*, 33(2), pp.304-05.

Vanderpump, M., 2011. The epidemiology of thyroid disease. *British Medical Bulletin*, (99), pp.39-51.

Venturini, L., 2003. Evaluation of systematic errors in thyroid monitoring. *Radiation Protection Dosimetry*, 103(1), pp.63-68.

Verhaegen, F. and Seuntjens, J., 2003. Monte Carlo modelling of external radiotherapy photon beams. *Physics in Medicine and Biology*, 48(21), pp.107-64.

Wheetman, A., 1994. Graves' Disease. In A. Wheetman and J. Lazarus, eds. *Diseases of the thyroid*. London: Chapman and Hall. pp.171-99.

Wiarda, K., 1984. Use of a Copper Filter for Dose-Calibrator Measurements of Nuclides Emitting K X-Rays. *Journal of Nuclear Medicine*, 25(5), pp.633-34.

Woods, M., Callow, W. and Christmas, P., 1983. The NPL Radionuclide Calibrator - Type 271. *International Journal of Nuclear Medicine and Biology*, 10(2-3), pp.127-32.

X-5 Monte Carlo Team, 2003. "MCNP - Version 5, Vol. I: Overview and Theory". *LA-UR-03-1987*.

X-5 Monte Carlo Team, 2015. *MCNP Reference Collection*. [Online] Available at: https://laws.lanl.gov/vhosts/mcnp.lanl.gov/references.shtml#mc_verif [Accessed 11 September 2015].